

I.FAST

Innovation Fostering in Accelerator Science and Technology

Horizon 2020 Research Infrastructures GA n° 101004730

MILESTONE REPORT

IIF Projects final progress

MILESTONE: MS12

Document identifier:	IFAST-MS12
Due date of deliverable:	End of Month 46 (February 2025)
Report release date:	23/07/2025
Work package:	WP4: Management of the Internal Innovation Fund (IIF)
Lead beneficiary:	CERN
Document status:	Final

ABSTRACT

This milestone reports the IIF projects final progress and results. The progress, innovations, and technical achievements have been constantly monitored, and a comprehensive overview will be presented during the 4th Annual Meeting held in April 2025. The financial aspects are periodically supervised and discussed with the CERN IIF financial officer.

I.FAST Consortium, 2025

For more information on IFAST, its partners and contributors please see <https://ifast-project.eu/>

This project has received funding from the European Union's Horizon 2020 Research and Innovation programme under Grant Agreement No 101004730. IFAST began in May 2021 and will run for 4 years.

Delivery Slip

	Name	Partner	Date
Authored by	L. Garolfi	CERN	17/07/2025
Reviewed by	M. Vretenar, L. Celona [on behalf of Steering Committee]	CERN	23/07/2025
Approved by	Steering Committee		23/07/2025

TABLE OF CONTENTS

1	INTRODUCTION.....	4
2	DESCRIPTION OF PROJECTS PROGRESS	5
2.1	HIGH-TEMPERATURE HIGH-GRADIENT SUPERCONDUCTORS (HIGHEST).....	5
2.2	PERMANENT MAGNET FOR HIGH EFFICIENCY KLYSTRONS (PM4HEK)	8
2.3	A FIELD EMISSION CATHODE FOR A TRAVELLING-WAVE RF GUN FOR HIGH BRIGHTNESS BEAMS IN INDUSTRIAL AND SMALL RESEARCH FACILITY SETTINGS (FE CATHODE)	10
2.4	KAIO ACCELERATOR	19
2.5	DEVELOPMENT OF HIGHLY EFFICIENT MW CLASS CROSS FIELD VACUUM TUBE AMPLIFIER FOR PARTICLE ACCELERATORS DRIVEN BY A SOLID-STATE POWER AMPLIFIER AT 750 MHZ.....	28
2.6	MILLISECOND FLASH LAMP TREATMENT FOR SRF ACCELERATING CAVITIES.....	30
2.7	AM APPLICATIONS OF REFRACTORY METALS FOR ION SOURCES	35
	36
2.8	DEMONSTRATION OF ADDITIVE MANUFACTURING FOR LARGE AND COMPLEX SHAPED VACUUM CHAMBERS BY PLASMA METAL DEPOSITION (PMD®).....	48
3	SCIENTIFIC PUBLICATIONS, DISSEMINATION, AND COMMUNICATION OF WORK.....	69
4	FUTURE PLANS / CONCLUSION / RELATION TO OTHER IFAST WORK	72
5	REFERENCES.....	84

Executive summary

This milestone summarises each IIF project final progress, detailing technical and experimental activities, numerical simulations, prototype manufacturing, tests, and validation. The main achievements, data, and results are reported. Chapter 3 lists the scientific publications, dissemination, and communications performed during the period P4 (April 2024 to February 2025). Chapter 4 briefly describes the conclusions, perspectives and future activities that some projects can undertake. The last Chapter is dedicated to the list of references used in this report.

1 Introduction

The scope of the WP4 activities included the implementation of an internal fund to support innovative technology developments in the I.FAST's second phase (3rd and 4th year), namely the Internal Innovation Fund, IIF. The Fund structure relies on nine thematic areas that intersect with the European Community's (EC) priority agenda. That allows tackling similar priorities while connecting the accelerator community and society. Also, it stimulates the accelerator technology innovation potential by encouraging the I.FAST beneficiaries to identify innovative solutions with viable industrial or commercial potential. The novel projects supported by the IIF should significantly advance the I.FAST state-of-the-art thematic areas while contributing to more sustainable particle accelerator facilities. This context implies reducing accelerators' power demand, footprint, and best performances compared to the same environmental impact or new green accelerator-based technologies.

The IIF budget attributed to CERN within the WP4 is one MEuro (EC contribution, total cost). Three different payment instalments are foreseen for the selected projects. The fund finances innovative projects at early development and prototype stages, with technical maturity up to a Technology Readiness Level (TRL) equal to 4 (validated in the laboratory). The project selection gave priority to those able to raise additional external funding. The Governing Board (GB) endorsed eight projects in November 2022. The selected projects have been executed by ten I.FAST beneficiaries with four new partners. The IIF projects started their activities in February 2023. Each selected project beneficiary received 50% pre-financing of the requested budget in March 2023. A second instalment of up to 80% of the total single project budget has been transferred upon submission of a technical report due in M36 (April 2024). A report of the interim progress and results has been provided by each IIF project and proved clearly and tangibly achievements of the ongoing activities. The final 20% of the budget will be transferred in M47 (March 2025) upon proving that final achievements meet the initial objectives.

2 Description of projects progress

2.1 HIGH-TEMPERATURE HIGH-GRADIENT SUPERCONDUCTORS (HIGHEST)

The focus of the HIGHEST project is to develop large width (up to 50 mm) HTS coated conductors (or “tapes”) by KCT for the sake of testing their RF properties at low field by CSIC-ICMAB. The final goal of our work, beyond the scope of IIF but enabled by it, is to test the materials produced within IIF in high-gradient RF field at SLAC, both on flat discs and on 3D segmented cavities. Large tapes would enable working with surfaces of larger dimensions, and thus RF structures of lower frequency, compared to standard 12-mm tapes, avoiding junctions between tapes.

As preliminary and background work, standard commercial 12-mm tapes will be soldered on discs and on 3D segmented cavities for low-gradient and high-gradient tests, to assess and develop the technology at the standard X-band SLAC frequency of 11.424 GHz.

Hereafter is the detailed description of internal Milestones and Deliverables proper for this project:

WP1 (CERN):

D1 - RF low power characterization of segmented cavities (small tapes) (due 6/2024)

All initial difficulties on cavity alignment and tape soldering were solved thanks to a thorough analysis, also with the help of the relevant CERN services (engineering, SEM analyses, surface treatments). Several segmented cavities relevant for the study have been prepared:

- Several cavities for axion searches and detection (two segments) have been coated. Of these, two cavities have been selected for their very promising performance (x3-x5 sensitivity improvement compared to standard copper reference cavities) and tested in a two-weeks physics data acquisition run at the SM18 facility at CERN, using a 11.5 Nb3Sn LHC prototype dipole for the background field (see Figure 1).



Figure 1. Left: two-segments cavities for axion detection. Right: assembly in the SM18 dipole.

- One segmented cavity for RF pulse compression (eight segments) has been prepared by SLAC, coated by ICMAB with 12-mm tapes and is being tested at present at SLAC (see Figure 2) (low-temperature, low-gradient results should be available by the end of HIGHEST). This cavity, if successful, will open-up the road for real accelerator devices demonstrating TRL6.

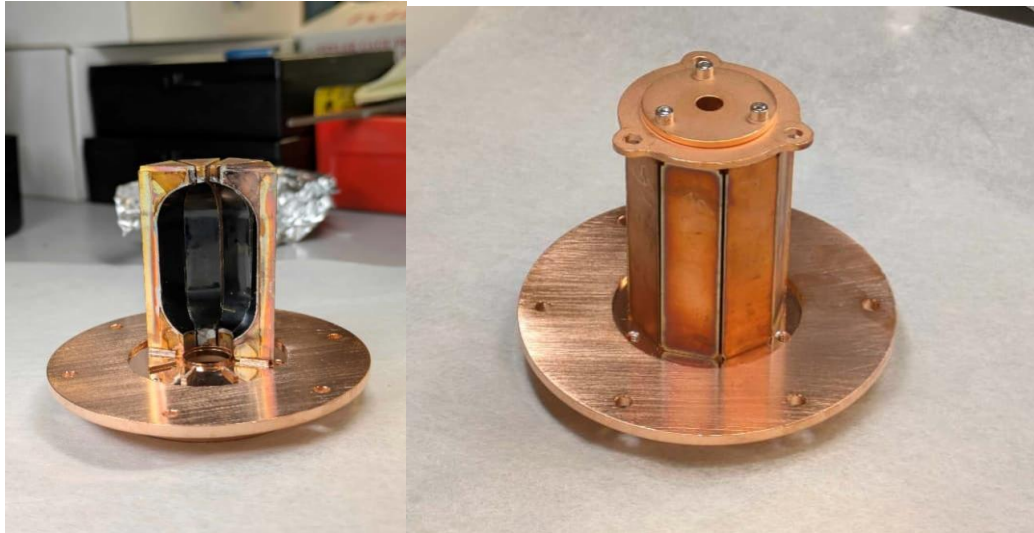


Figure 2. Left: eight-segments cavity for pulse compressor, opened with HTS coating visible. Right: eight-segments cavity for pulse compressor, assembled.

D2 – Final report (due 3/2025)

- The present report.

WP2 (KCT):

D1 - HTS coating of large samples (due 3/2025)

- The first tape delivered already mid-2024 was not very successful in term of RF performance tested at ICMAB. Thus, it was decided to improve and optimize the fabrication process following several routes for the buffer layers, coating YBCO on tapes of different widths (see Figure 3). These coatings are performed without artificial pinning centres, which improve the performance at high externally applied magnetic field. First RF measurements at ICMAB on these optimized tapes demonstrate performance comparable with the best commercial 12-mm wide tapes, as discussed later.

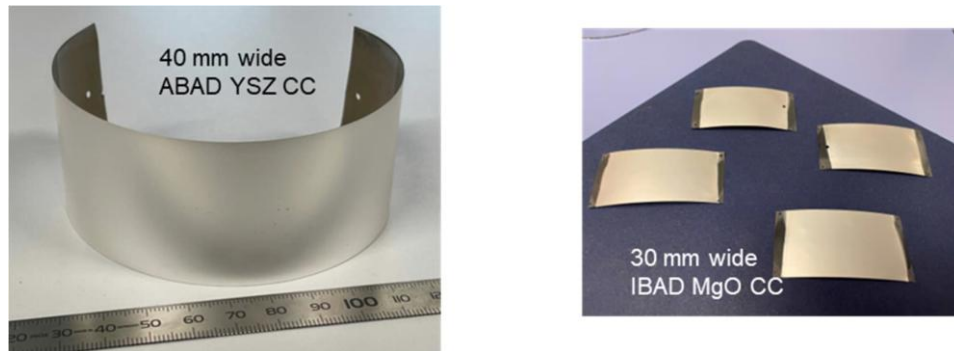


Figure 3. Tapes of 30 mm and 40 mm width were coated with YBCO on different buffer layers.

WP3 CSIC-ICMAB:

D1 - Coating on discs and segmented cavities for benchmarking (small tapes) (due 3/2024)

- Coating on the eight-segments cavity is successful, as described earlier. The cavity is waiting for cryogenic tests at SLAC. A preliminary room-temperature RF verification confirmed expectations for quality.

D2 - Measurement of superconducting properties of large size tapes (due 3/2025)

- First 40 mm wide tape was already characterized mid-2024 as discussed earlier. The new generation of coatings that were produced was characterized recently with the 8 GHz dielectric resonator of ICMAB. Sample tapes as prepared for the RF measurement are illustrated in Figure 4. First results at 50K (relevant for FCC-hh impedance reduction, or for RF application operated with a cryocooler system) and at 20K (relevant for RF applications operated with liquid-helium cryogenics) as a function of applied external magnetic field will be published. For RF high-gradient applications the external field would be zero. Copper at 50K would have a surface resistance of 8 mOhm; state-of-the-art commercial HTS tapes would have a surface resistance at zero external magnetic field of 0.2÷0.5 mOhm. The obtained results, similar to the performance of state-of-the-art tapes at zero externally applied magnetic field, are extremely positive and coronate the success of HIGHEST.



Figure 4. samples of large-size HTS tapes, prepared at ICMAB for RF characterization with the 8 GHz dielectric resonator

2.2 PERMANENT MAGNET FOR HIGH EFFICIENCY KLYSTRONS (PM4HEK)

The PM4HEK (“Permanent Magnets for High-Efficiency Klystrons”) project aims to design and fabricate a magnetic electron beam confinement system composed of permanent magnets, to be installed in the 8-MW, 12 GHz high-efficiency klystron. Since permanent magnets consume no energy, the installation would increase the overall efficiency of the full power source from 23.7% to 35.5%.

In the first design phase, a solenoid-type permanent magnet structure has been designed surrounding the klystron tube and producing a solenoidal magnetic field profile that successfully confines the klystron beam in the simulations performed in DGUN and CST Particle-in-Cell. It is composed of radially and axially magnetized NdFeB magnets arranged in segmented cylinders of adjusted sizes to fit the klystron tube and provide a good field quality. The design process has been steered through weekly meetings between CERN and ELYTT where results on simulations and parameters were exchanged and discussed.

As anticipated, small errors in the permanent magnets near the emission cathode can compromise the beam dynamics at the entrance of the tube. For this reason, a low-power ($< 3\text{W}$) correction coil has been added to the design at this location. This will allow the magnetic field to be compensated. This is indeed common practise also for electromagnetic solenoids which include a smaller current bucking coil for field compensation.

The PM magnets should be sorted to minimize the transverse field components on the beam that confinement of electron beam.

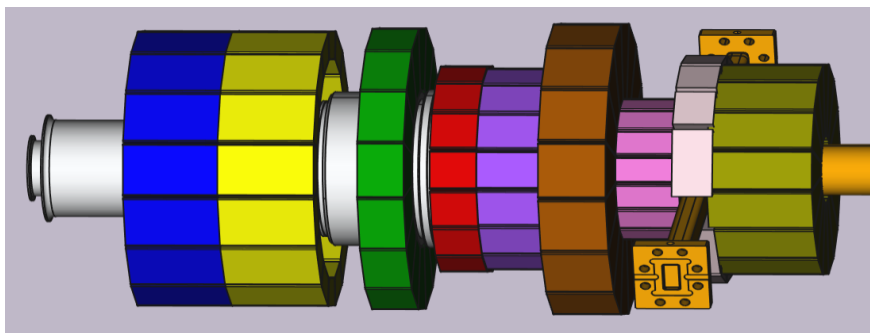


Figure 5: 3D model of permanent magnet configuration for solenoidal confinement of the electron beam. Permanent magnet cylinders are shown in colours.

The final design of the solenoid is shown in Figure 5. The final field has been used in beam simulations and preserves the high efficiency of the original klystron. However, this solution cannot be adapted to the current geometry of the klystron commercialised by Canon. There are two main reasons to this:

- To preserve the symmetry of the field and avoid transverse components, the input and output window need to be taken to the opposite sides of the same sector. An elongation of the input window inside the PM solenoid has been designed.
- The current location of the collector is not compatible with the geometry of the PM solenoid. Indeed, using permanent magnets leads to an unwanted beam refocusing after the drift tube due to magnetic field reversal. In order to minimize the return of electrons that will generate an instability on the klystron, and the power deposition in the collector, additional magnets beyond the RF output are required. This means the collector must be located further away from the output waveguide.

Currently, a physical demonstrator of Figure 5 is being manufactured. It is not intended to be installed in the current klystron, but it would allow to verify the magnetic field simulation results and field compensation techniques discussed above, including magnet measurements. Full manufacturing drawings were done as final stage of the design phase including the magnets, the mechanical support and the assembly and magnetic measurement tooling.

Procurement has been divided in three different supplies all of which have been already launched.

- The magnetic elements themselves are being manufactured and are expected by the end of June. However, delivery from China may be delayed by new export regulations on rare earth materials and NdFeB magnets.
- The aluminium mechanical structure holding the magnets in place has been manufactured and can be seen in Figure 6.
- Assembly and magnetic measurements tooling is being prepared. Magnetic measurements hardware is ready as shown on Figure 7a. and 7b shows the assembly tooling that will be done by additive manufacturing.

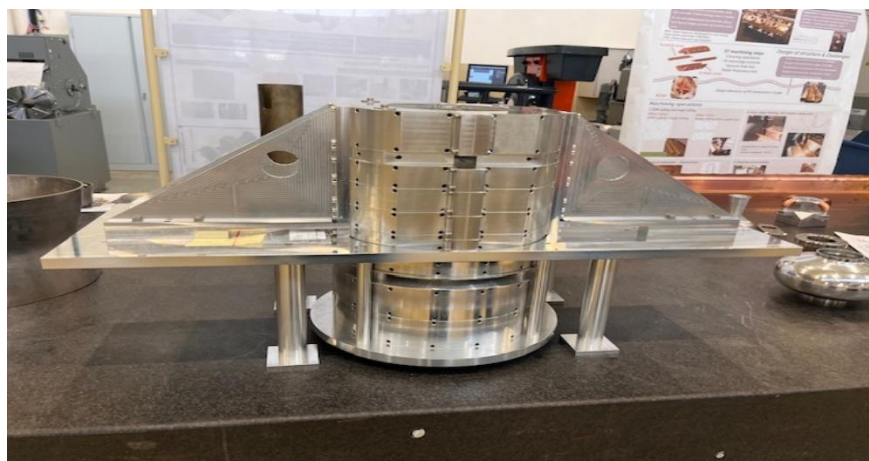


Figure 6: Mechanical structure holding the permanent magnets that allows installation around the klystron. The middle plate separates the part submerged under oil inside the modulator.

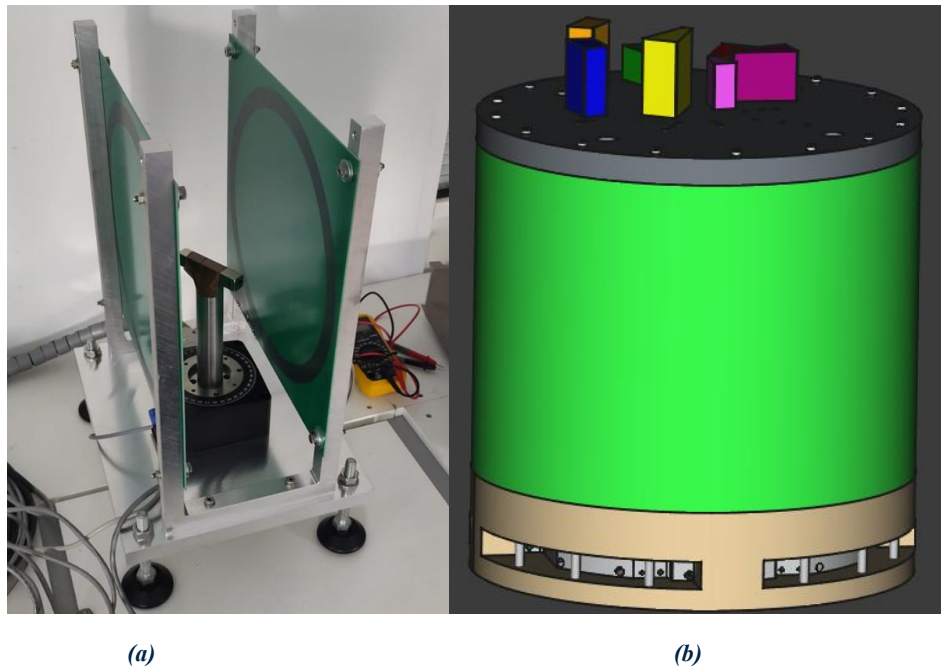


Figure 7: Tooling for magnetic measurements and installation. (a) Helmholtz coils for magnetization measurements of the permanent magnets. (b) 3D model of tooling for installation of the magnets in their holders.

2.3 A FIELD EMISSION CATHODE FOR A TRAVELLING-WAVE RF GUN FOR HIGH BRIGHTNESS BEAMS IN INDUSTRIAL AND SMALL RESEARCH FACILITY SETTINGS (FE CATHODE)

This report details the development of a novel field-emission traveling-wave (TW) RF gun, aimed at generating low emittance and high average current electron beams for advanced accelerator applications such as radiotherapy and MeV UED. The project began with extensive beam dynamics simulations to optimise the cathode shape and determine the ideal phase velocity shift required for low energy spread. The field emission cathode was then realised in OFHC copper and shipped to PSI. Low-power testing of the TW rf gun, conducted in an involved S-parameter measurements and bead-pull testing, confirming excellent low power electromagnetic performance of the TW RF gun.

Following these successful low-power measurements, the gun was installed in a high-power test stand at PSI, where initial conditioning is now underway and has made significant progress towards the ultimate goal of 17 MW input power. However, the development process was not without challenges. Delays occurred due to concurrent infrastructure upgrades at PSI and funding allocation issues, impacting resource availability. Despite these setbacks, the project has maintained steady progress towards completion. Below is a summary of our output for the project.

PICS Simulations of Field Emission TW Gun

To demonstrate the potential of this concept, beam dynamics simulations of the TW RF field emission gun were conducted using CST. Firstly, such simulations were key to understanding the optimal shape of the field emission cathodes. Figure 8 illustrates the field emitter geometry with electric field magnitude. Here we see that the field emission cathode has been developed to enhance the field on the centre of the cathode to approximately 3 times greater than the peak axial field. This ensures that the field emission originates from the field emission tip rather than the cells' irises. The aim was also to keep the field emission tip below 200 MV/m while the accelerating gradient was at least 32 MV/m. This condition occurs with an input power of 17 MW. With the shape of the cathode determined, the beam dynamics modelling could continue. This was divided into two steps: first, solving the electromagnetic field-maps in the frequency domain solver, while shifting the drive frequency to generate a phase ramp; then, importing these field-maps into the PIC solver, where the field emission electron source was defined and simulated. Simulations were performed at various drive frequencies to determine the optimal phase velocity shift. This lay at 4 MHz above the regular frequency of 5.712 GHz. Figure 9 illustrates the propagation of field-emitted electrons through the gun given a frequency offset of 4 MHz. The beam is observed to be well bunched by the end of the gun. However, with this pictorial representation, it is hard to elucidate the impact on the phase velocity on the energy spread within the bunch. Figure 10 compares the impact of a frequency offset to a nominal drive frequency, or equivalently a phase velocity less than c to that which is equal to c . The results show that lower-energy particles are accelerated toward the main peak, an effect that only works with a bunched beam. This is illustrated in the right-hand plot of Figure 10, where the field emission distribution is contrasted with that of a thermionic cathode, which emits beam continuously while using this same phase ramp technique. Unlike the field emission source, the thermionic cathode, retains a large intrinsic energy spread.

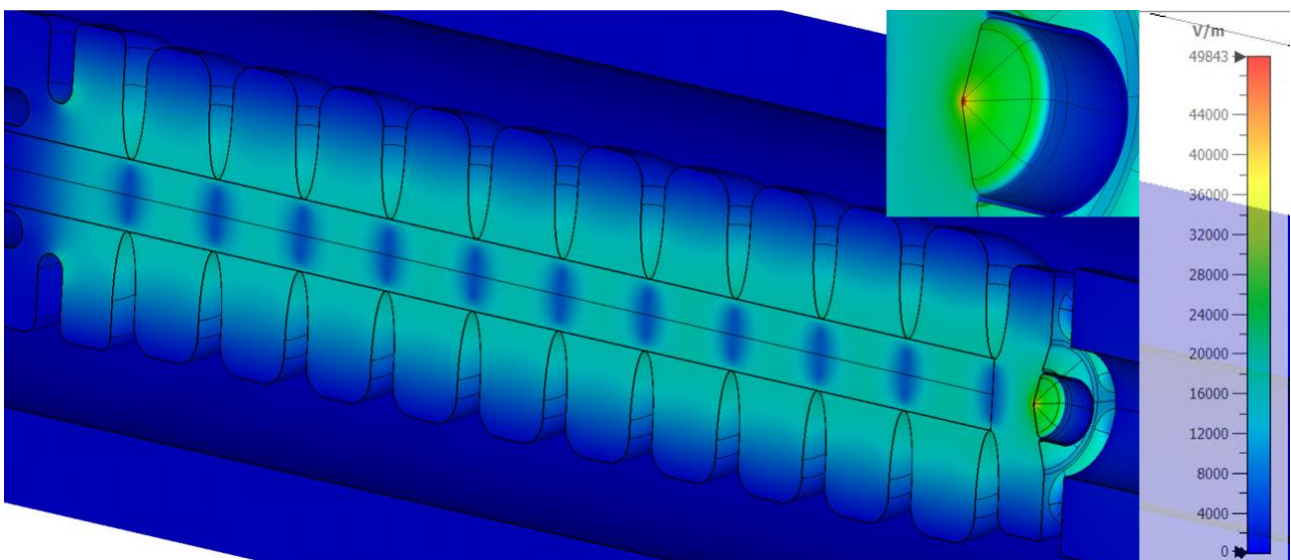


Figure 8: Field Emission cathode geometry determined through electromagnetic simulations.

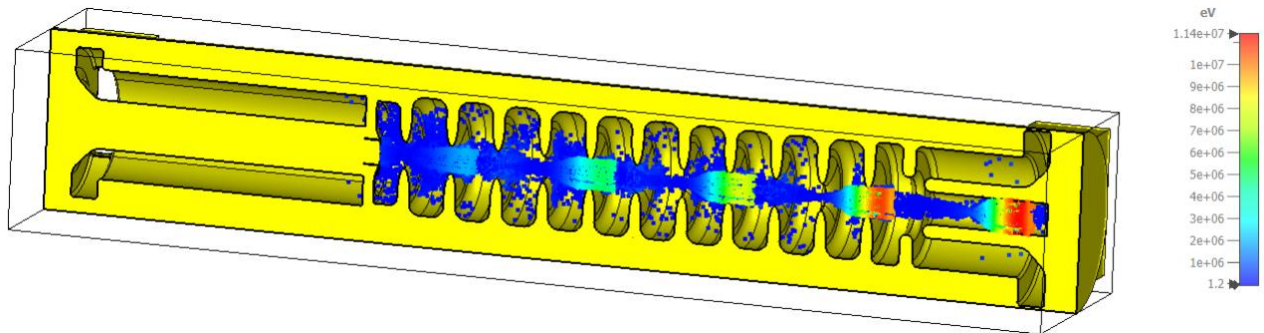


Figure 9. field emission distribution contrasted with that of a thermionic cathode

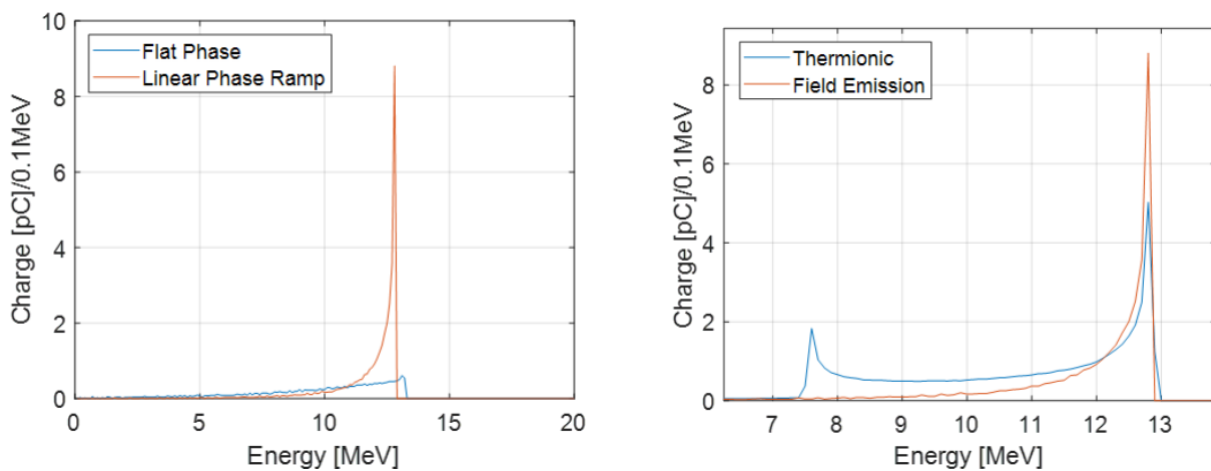


Figure 10. Simulations of the energy spread achieved with and without phase ramping.

Realisation of Travelling-Wave RF gun and Field Emission tips

With the known geometry of the cathode, the next step was its realisation. All the oxygen-free high conductivity copper pieces for this task and the original TW gun (Figure 11) were machined at VDL ETG Precision. The parts were initially pre-turned and milled, after which the final single point diamond turning machining and UP milling steps were carried out. The completed pieces were then measured using a CMM, before being cleaned and inspected. Once the parts were illustrated to be within tolerance, they were shipped towards PSI. The final field emission cathode and CMM measurement of the tip are illustrated in Figure 12. Here we see that the tip of the field emitter has a radius of approximately 150 μm , which is then tapered down to the cathode edges. This leads to significant field enhancement on the tip of the cathode (recall Figure 8) while also maintaining enough bulk material to mitigate catastrophic damage to the emitter in the event of a breakdown (expected due to the large local electric field).

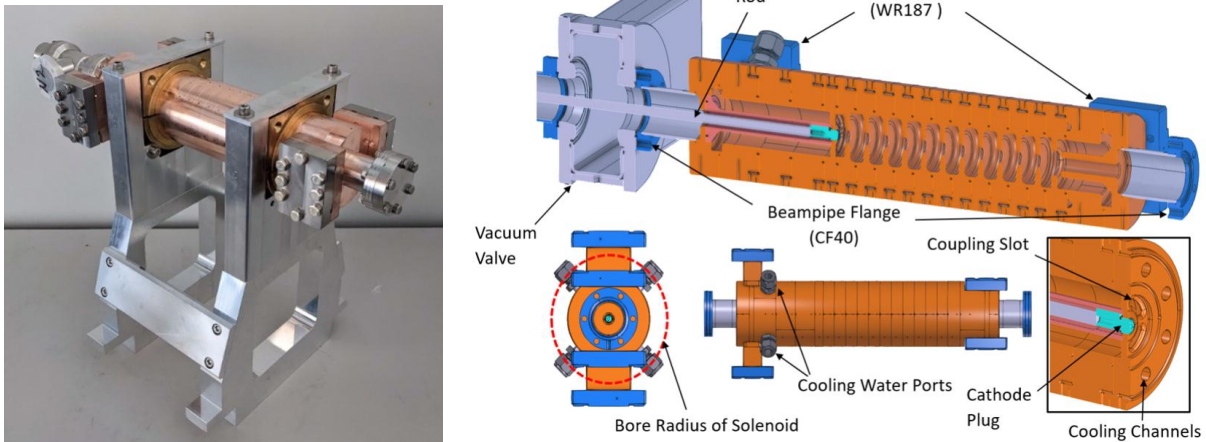


Figure 11. Diagram of the mechanical layout and realised TW RF gun where the field emission cathodes can be mounted.

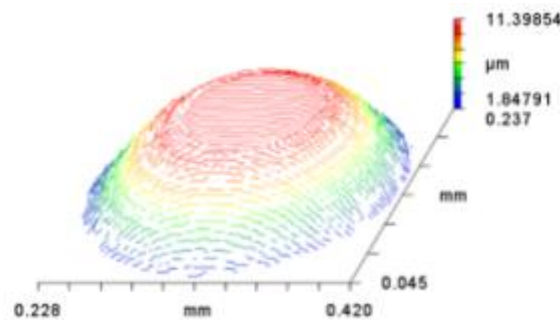


Figure 12. The machined field emission tip and measurement of the realised tip.

Low Power Testing

The low-power testing of the traveling-wave (TW) RF gun was conducted in a controlled PSI cleanroom environment to minimise contamination inside of the device. Two measurement methods were employed for the test: S-parameter measurements and bead-pull testing, both of which provided insights into the gun's electromagnetic properties and resonance characteristics. For the measurements, a Rohde & Schwarz 8 GHz network analyzer (ZVA8) was used to evaluate the reflection coefficient (S11) across the operating frequency range (Figure 13). The results indicated excellent matching when the cathode was tuned to its optimal position, with the S11 value measuring below -30 dB. This low reflection level confirmed minimal power loss and efficient coupling of RF

energy into the structure. Additionally, bead-pull measurements were performed to map the field distribution on the beam axis of the gun and verify the uniformity of the accelerating fields. These measurements ensured that the field profile matches the simulation predictions, further validating the gun's design. Overall, the low-power tests found strong agreement with the electromagnetic simulations (Figure 8), setting the stage for the high-power conditioning and further performance validation.

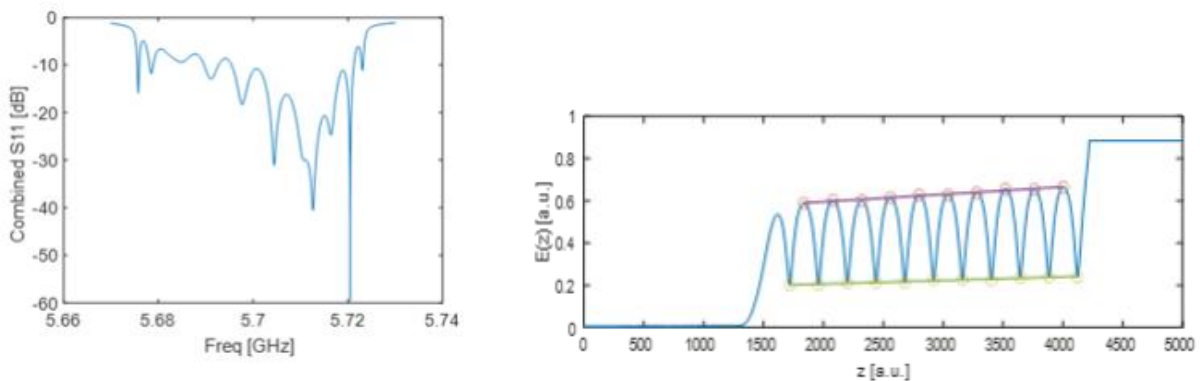


Figure 13. The low power measurement of the TW RF gun. The left-hand figure illustrated the S-parameter measurements with the operational frequency of 5.712 GHz illustrated to have a reflection coefficient (S_{11}) of approximately -40 dB. The right-hand figure depicts the axial fieldmap as illustrated by a beadpull measurement. The red and yellow dots indicate the local maxima and minima of the fieldmap used to calculate the amplitude variation between cells.

LLRF, Vacuum System and GUI upgrade

Before high power measurements could take place, the LLRF system required an upgrade to align it with the SwissFEL LLRF, primarily through software and firmware updates. On the hardware side, additional channels were added to read RF signals from the waveguide network. Furthermore, an extra ADC was added to the LLRF in order to measure the dark current.

The vacuum system was also upgraded, with several new vacuum gauges and controllers added, and an updated user interface. Figure 14 illustrates the GUI for the new vacuum system.

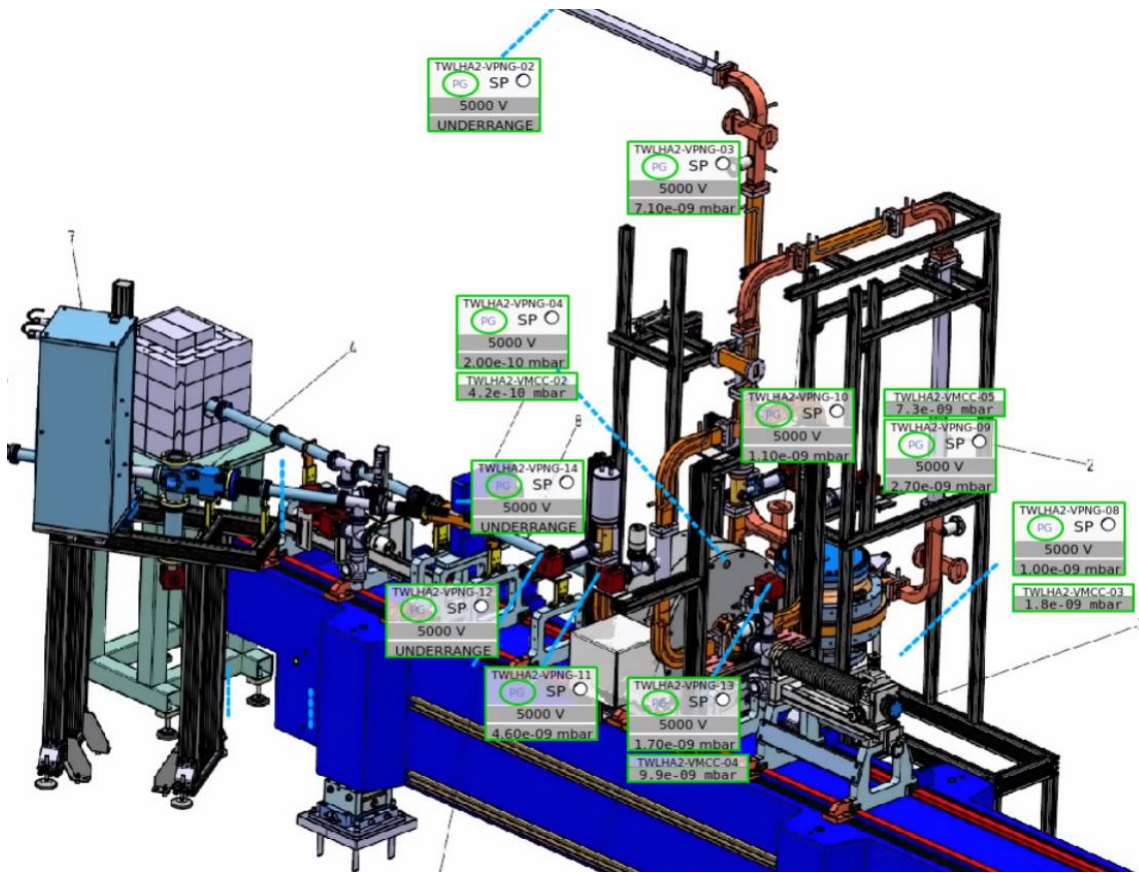


Figure 14. The user interface of the updated vacuum system.

Installation, High Power Conditioning and first dark current measurements

Since its successful realisation and low power testing, the TW RF gun has been installed in the high-power test stand at PSI, marking a significant achievement in its development. Figure 15 displays the installed device within the test stand with annotations of the critical components. Along with the TW rf gun, we see that a BOC pulse compressor has also been installed. This is used in the instance that the peak power required is greater than that possible from the klystron. This is primarily for the use of the TW gun with the photocathodes. Downstream of the TW gun is a faraday cup to measure the dark current. This will eventually be replaced by the diagnostic beamline once the conditioning has concluded. The high-power conditioning of the TW RF began on February 18th, 2025, and the initial high power testing results are illustrated in Figure 16. Here we see that the TW gun is making steady progress towards its goal of 17 MW input power. Once the structure reached an input power of 15 MW, or an average accelerating gradient of 37 MV/m inside the cavity, the first field emission measurement was performed. Figure 17 depicts the measured dark current level illustrating the successful generation of a dark current beam from the TW rf gun, indicating the system operates with a large enough accelerating gradient that the capture of field emission cathodes is possible.

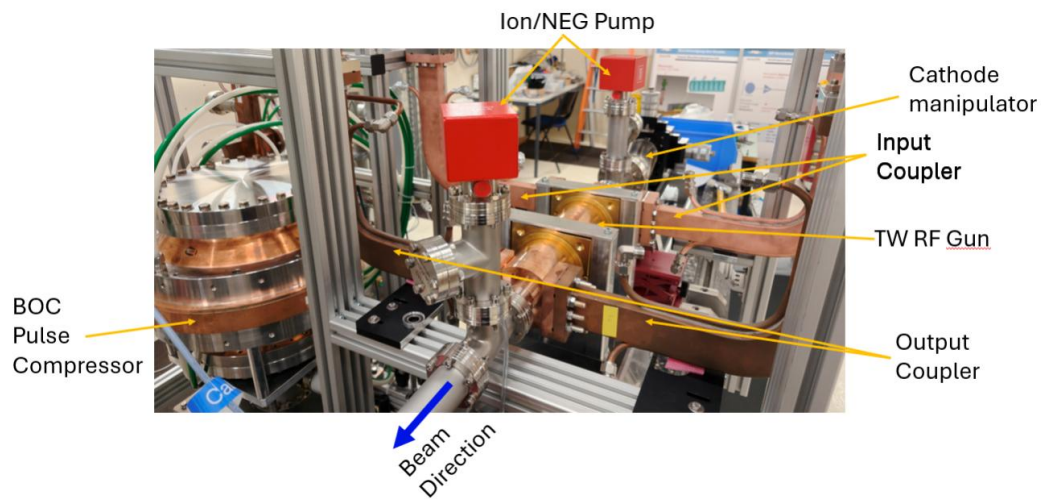


Figure 15. TW RF Photo-gun installed in the WLHA test stand at PSI.

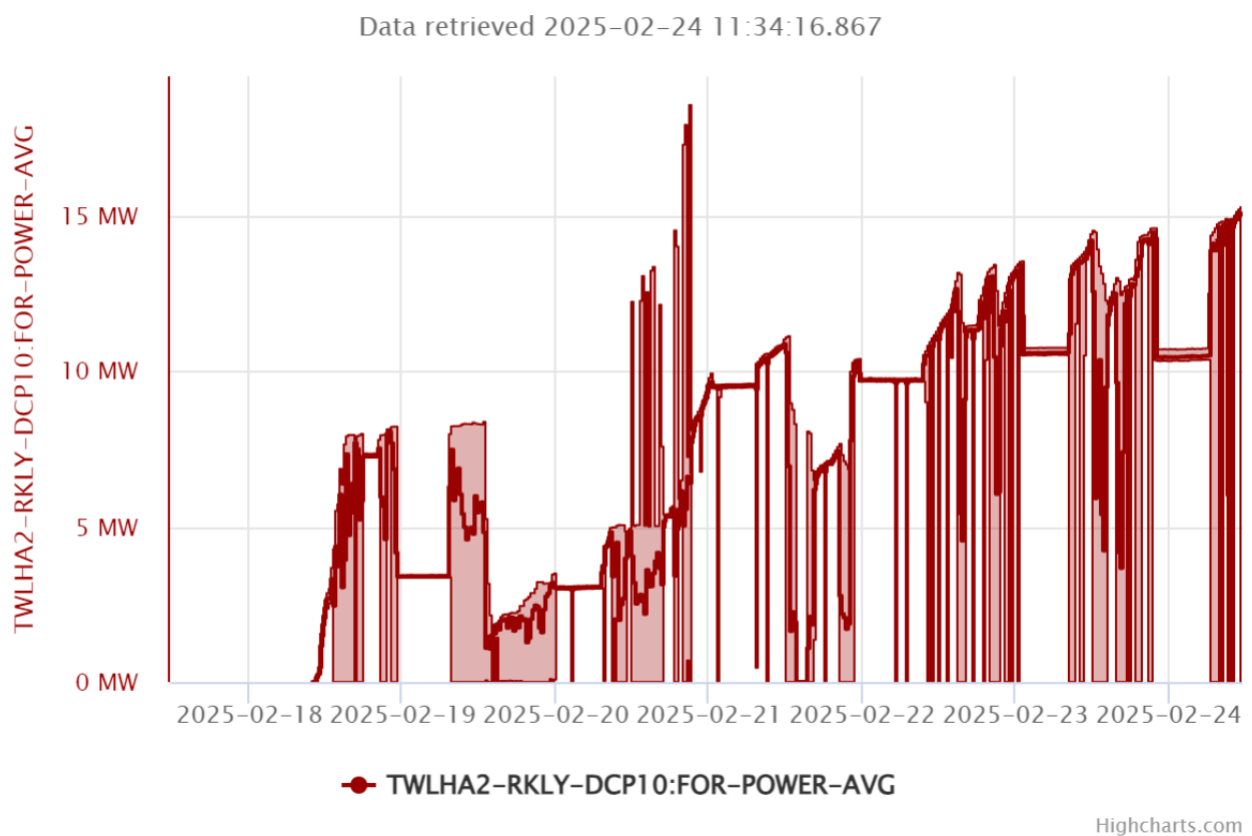


Figure 16. Initial conditioning of the TW RF gun in the test stand.

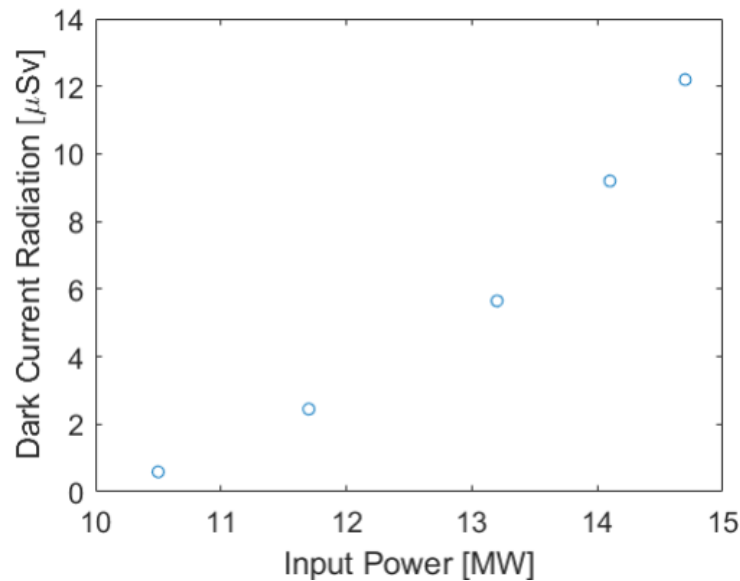


Figure 17. The first dark current measurements from the high-power tests of the gun.

Diagnostics Beamline

The beamline downstream of the TW RF field emission gun features a spectrometer designed to measure the energy spread of the field emission bunches. This feature will be used to diagnose the energy spread improvement expected from the phase velocity manipulation after the high-power conditioning. This spectrometer consists of a C-type bending magnet along with a diagnostic YAG screen developed for SwissFEL. Figure 18 illustrates the layout of the diagnostics beamline with annotations. The beamline components have all been ordered and delivered to PSI. These are being assembled and will be installed after the successful high-power conditioning of the TW RF gun.

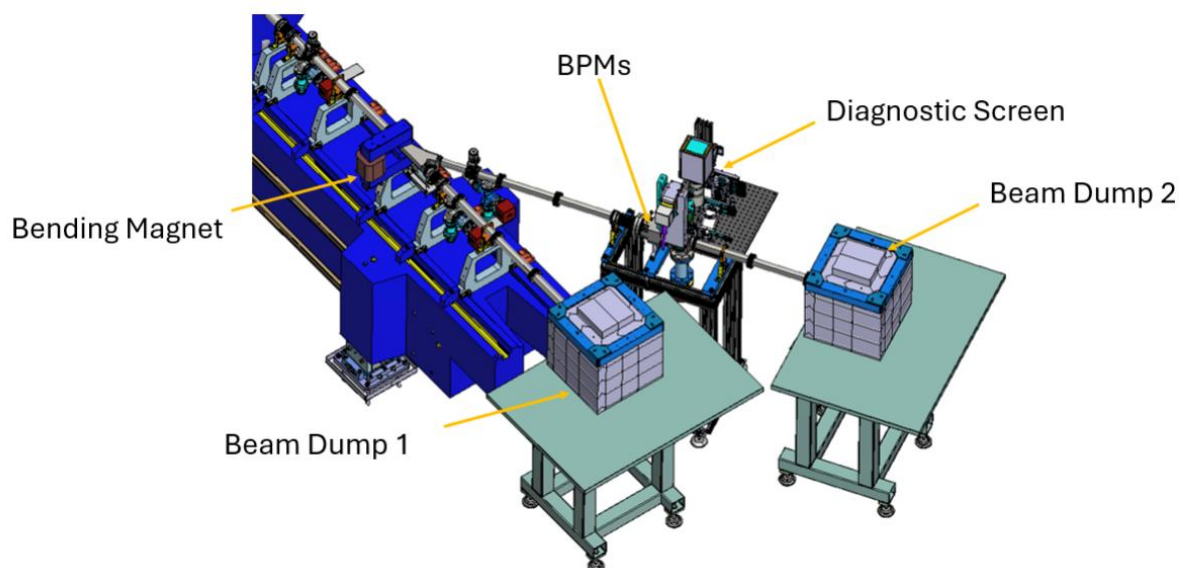


Figure 18. Layout of the beamline for the energy spread diagnosis.

Sustainability and Environmental Impact

In addition to the beam quality and technical details of this work, the TW rf field emission gun offers other advantages when compared to competitive technologies in the area of sustainability and environment impact. The following are a few crucial points where this new device can make improvements on current technologies.

Power Consumption

A key advantage of the field emission over traditional photo-guns is its significantly lower power consumption, achieved by eliminating the high-power laser system. Both systems require a high-power RF modulator with a klystron. These systems generally operate at a power of 10-50 kW depending on the type. Table 1 illustrates two possible klystrons for modulators that could run the system. These each operate with average powers of 15-20 kW. Such systems are required for high power rf gun. However, RF photo-guns also require a high-peak-power laser system, which consumes an additional 10 kW, depending on laser specifications. By omitting the laser system, the field emission RF gun reduces the overall power consumption by the electron source. This lowers operational costs, decreases cooling requirements and reduces the machine environmental footprint making the field emission RF gun a more sustainable choice for facilities focused on reducing their environmental footprint.

Parameter	E37212	E37217	Units
Frequency	5.712	5.712	GHz
Voltage	370	280	kV
Beam Current	344	240	A
Peak RF output power	50	20	MW
Average RF output power	15	20	kW
RF Pulse Length	3.5	2.5	μ s
Repetition Rate	100	400	Hz

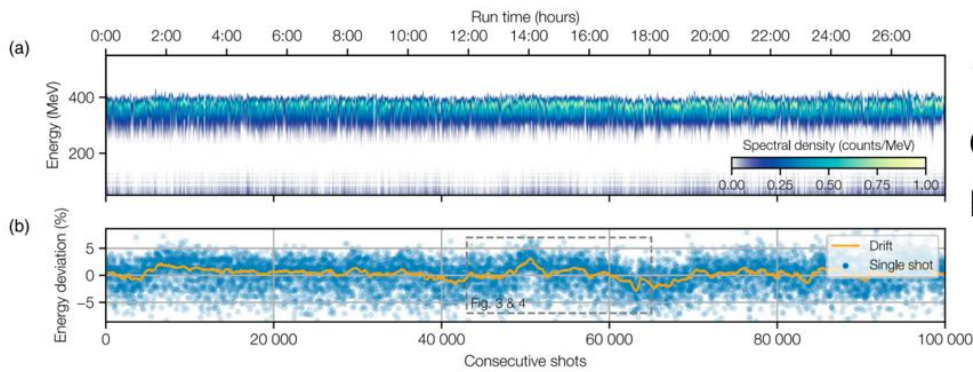
Table 1: Klystron options for the beamline.

Hazardous Substances

In addition to the reduced power consumption, the travelling-wave (TW) RF gun system eliminates the need for an RF circulator, a component commonly used in traditional RF photo-guns to protect sensitive equipment from reflected power. RF circulators often rely on sulfur hexafluoride (SF₆), a gas with significant health and environmental risks, in order to operate at very high electric fields. SF₆ decomposes into toxic byproducts (e.g. S₂F₁₀ or SF₄) during electrical breakdowns, posing health hazards to personnel. Furthermore, SF₆ is a potent greenhouse gas with a global warming potential (GWP) over 23,500 times that of CO₂ [6], persisting in the atmosphere for thousands of years and contributing significantly to climate change. By removing the need for SF₆, the TW RF gun system reduces workplace hazards and aligns with environmental sustainability goals, offering a safer and more eco-friendly alternative for facilities striving to minimise their environmental impact.

2.4 KAIO ACCELERATOR

Compact high-flux laser-induced plasma accelerators (LPAs) are expected to enable entirely new modalities in medical diagnostics, radiation therapy and industry-scale imaging [1]. LPAs have been moving towards mainstream acceptance and the past few years have seen increased R&D activity aimed at demonstrating reliability and control of LPA beam quality, mainly by using active feedback systems [2,3] and machine-learning algorithms [4,5] to optimize the many laser-plasma interaction parameters and demonstrate reliable operation of LPAs driven by multi-TW peak power lasers at Hz-level repetition rates over many consecutive hours (cf. Fig. 19). Although such efforts will undoubtedly make LPA operation more reliable for research purposes, the actual market deployment of LPA technology is hampered by the fact that it is almost entirely based on Titanium:Sapphire (Ti:Sa) lasers that are not reliable and cost-effective enough, and offer too low particle flux for the development of industry-grade LPA-based applications.



100-TW LPA
operated 28h in a
row!

Figure 19. Continuous operation of a Joule-class 10 Hz Ti:Sa laser-driven LPA [1].

In an LPA, the accelerating properties of the plasma wakefield are optimal when driven in the so-called “bubble” regime, for which the laser pulse is spatially comparable to the plasma wave. This resonance condition helps to establish some basic scaling laws [6] for the net electron energy gain as a function of laser pulse energy and duration [6]. So, as one can typically generate 100 MeV- to GeV energy electrons using Joule-class 30 fs lasers operating at a few-Hz (e.g. Fig.19), reducing the pulse duration to a few femtoseconds, few-MeV electron beams can be produced with pulses containing only a few mJ of energy, thus enabling the use of kHz Ti:Sa laser technology [7,8].

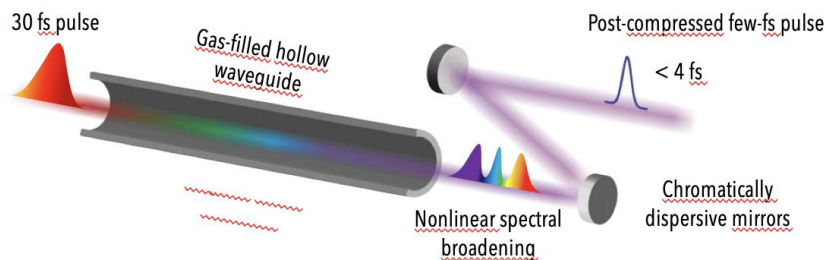


Figure 20. Principle of laser post-compression by nonlinear spectral broadening in a gas-filled hollow waveguide [9].

Pioneered more than 20 years ago, the most widespread method for generating few-mJ, few-fs is based on spectral broadening of longer pulses, typically 30 fs, by nonlinear propagation at high intensity inside a hollow waveguide filled with a rare gas [9]. Using dispersive mirror technology, the newly generated laser frequencies can be repackaged to produce shorter pulses (Fig. 20). This technique is at the heart of the laser system operated at LOA, enabling the routine « post-compression » of 30 fs pulses from a 10 mJ kHz Ti:Sa laser system down to a few fs, thereby boosting the peak power of the laser to TW level for driving few-MeV LPA operation [10]. In collaboration with the group of Prof. Jérôme Faure, one of the pioneers of LPA science, we used the kHz train of few-mJ - few-fs laser pulses to demonstrate continuous « hands-off » LPA operation for 5 hours, with a world record in terms of the number of consecutive shots (Fig. 21). However, this rather complex waveguide-based “post-compression” technology underpinning this milestone achievement has already hit its performance limits in terms of energy and average power scalability, impeding the market development of commercially viable LPA value chain.

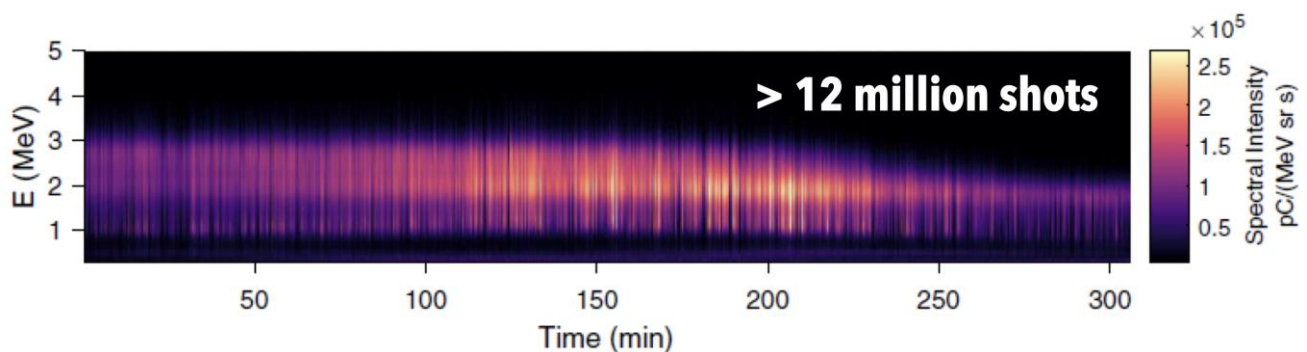


Figure 21. Continuous electron energy spectra recorded on a post-compressed kHz Ti:Sa laser-driven LPA [11].

As shown in Figure 22, a commercial kHz-driven LPA value chain should combine the following three enabling technologies (hence the name KAIO for « Kit-All-In-One »):

1. A reliable and cost-effective high average power (HAP) laser driver
2. An efficient and scalable pulse compression module to boost the laser peak power for LPA.
3. A compact and versatile LPA module that utilizes the post-compressed pulses to produce the desired electron and secondary beams (e.g. x-rays) for targeted applications downstream (e.g. radiobiology, radiotherapy, non-destructive testing).

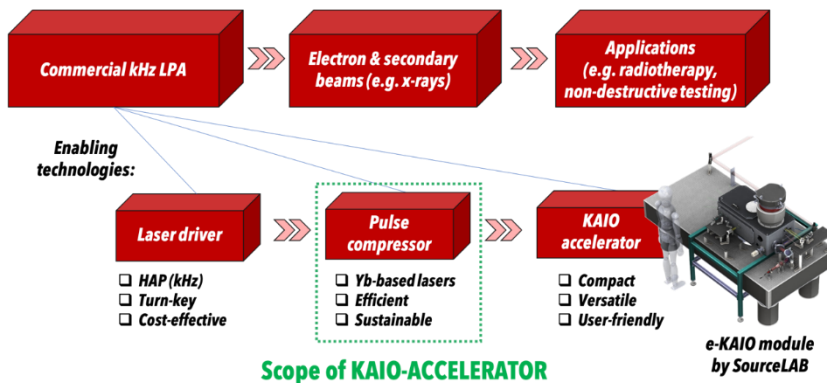


Figure 22. Enabling technologies for a KIAO (Kit-All-In-One) commercial HAP Yb laser-driven LPA value chain (e-KAIO electron accelerator module by SourceLAB shown for reference, <https://www.sourcelab-plasma.com/news/>).

The end goal of KAIO ACCELERATOR project is to develop a compact and modular LPA systems driven by temporally post-compressed commercial HAP ultrafast lasers. The commercial viability of this LPA value chain relies mainly on the specific development of laser pulse compressor modules that enable access to the optimal LPA regime with two key technical advantages:

1. Efficient pulse compression to reduce the amount of laser power needed for acceleration.
2. Sustainability through the enhanced wall-plug efficiency of industry-grade HAP Ytterbium (Yb)-based lasers.

Fig. 23 compares the typical performance of post-compressed Yb lasers to other existing laser technologies. Although Ti:Sa and optical parametric chirped pulse amplifiers (OPCPA) systems can readily produce shorter pulses, the average power and efficiency of post-compressed Yb lasers makes them superior candidates for driving LPA. Recent technology reviews [12,13] predict that in the next coming years, the development of highly efficient post-compression schemes should enable the deployment of industry-grade post-compressed Yb lasers delivering multi-TW peak power at kW average power with wall-plug efficiencies in the 10 % range.

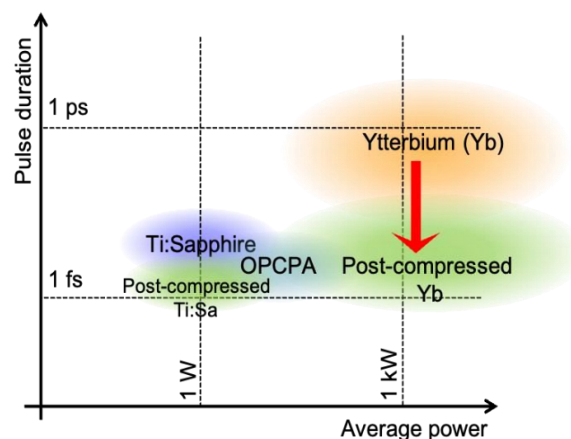


Figure 23. Comparative performance of existing ultrafast laser technology [12,13]

The main issue with conventional waveguide-based post-compression is that it cannot handle high powers as free-space propagation can, making energy-scaling quickly impractical [9]. The solution is to combine the advantage of free-space and waveguide propagation by using a repeated optical imaging system that allows you to distribute the nonlinearity over extended distances, like a periodic lens arrangement allows you to go through multiple foci, each contributing to the overall nonlinearity. By folding this periodic arrangement within a near-confocal cavity formed by curved mirrors facing each other, otherwise called multi-pass cell (MPC), very high interaction lengths can be achieved, yielding high pulse compression factors for high laser powers, while keeping a small footprint. Figure 24 shows the first ever demonstrated MPC-based post-compression results for 30 fs pulses from a mJ-energy kHz Ti:Sa laser system at LOA. The input pulses could be post-compressed down to sub-6 fs duration after 16 passes in a 3-m length MPC filled with just under 0.5 bar pressure of Argon gas, with almost 70% overall efficiency [14]. These very encouraging results provided the main motivation for the KAIO ACCELERATOR project.

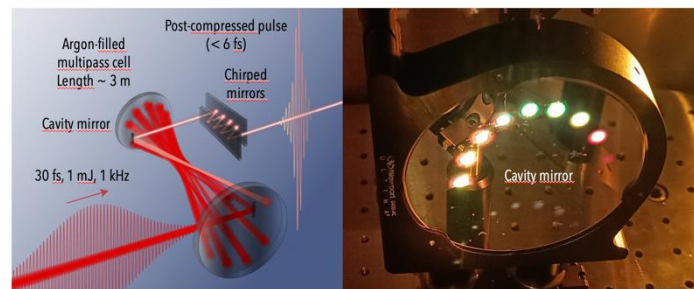


Figure 24. Left: schematic of first MPC-based post-compression of 1 mJ, 30fs pulses from a kHz Ti:Sa laser at LOA. Right: image of the progressive nonlinear spectral broadening visible on one of the MPC cavity end-mirrors [14].

As illustrated in Figure 25, the technical scope of KAIO ACCELERATOR was to develop efficient MPC post-compression modules that can be driven by commercially available ultrafast kHz lasers and therefore be integrated into a commercial LPA value chain. The loan of two commercial laser drivers, respectively based on Ti:Sa and Yb technologies, was successfully brokered by SourceLAB, which also participated in the mechanical design of the different MPC modules. In parallel, DF Photonics Consulting compiled a comprehensive market study of LPA-based technology. Finally, both academic partners, LOA and CNR-INO, planned to benchmark the performance of LPA beams driven by the post-compressed lasers against that of a conventional accelerator beam [15].

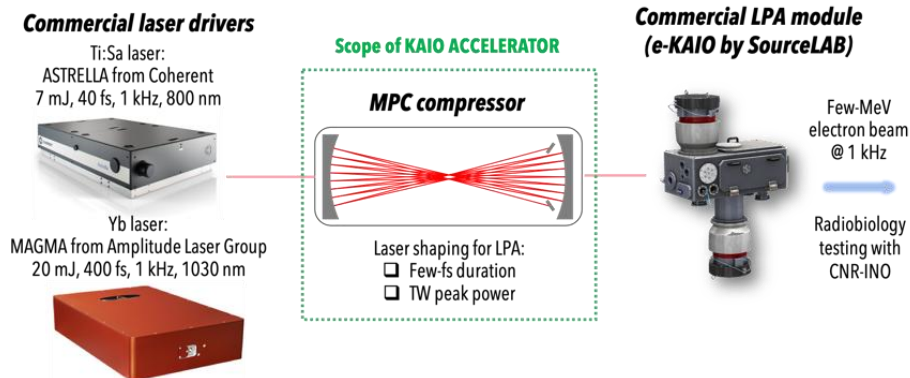


Figure 25: KAIO ACCELERATOR project plan.

The planned R&D flow, spanning over 24 months, was divided into the following work packages:

WP1:

Objective: demonstrate efficient MPC post-compression of the ASTRELLA USP laser from Coherent Inc. [16], the only commercially available industry-grade multi-mJ kHz Ti:Sa laser on the market. As its performance in terms of pulse energy and duration prior to post-compression is comparable to that of the Ti:Sa-based LPA driver used at LOA, MPC-based post-compression performance could therefore be efficiently benchmarked against that of waveguide technology.

Milestone: MPC post-compression of 7 mJ 40 fs pulses at 1 kHz

Contributors: LOA, SourceLAB

Timeline: T0 + 12 months

WP2:

Objective 1: demonstrate MPC-based post-compression of the MAGMA 25 laser from the Amplitude Laser Group [17], which is an integrated Yb-based laser system delivering longer pulses and higher energies (< 400 fs, < 20 mJ), for which a specific MPC compressor design is needed in order to achieve higher compression factors while maintaining high energy efficiency.

Objective 2: Demonstrate continuous few-MeV kHz LPA operation using the e-KAIO accelerator module by SourceLAB driven by MAGMA 25 laser pulses post-compressed down to few-fs duration using a tailored MPC design.

Milestone 1: Post-compression of 20 mJ 400 fs 1030 nm laser pulses at 1 kHz

Milestone 2: Continuous MPC-compressed Yb-driven LPA operation at 1 kHz driven.

Contributors: LOA, SourceLAB

Timeline: T0 + 18 months

WP3:

Objective: Radiobiological study on single-strand DNA breaking using few-MeV LPA beam driven by MPC post-compressed laser [15]

Milestone: Benchmark LPA performance against conventional electron source

Contributors: LOA, CNR-INO

Timeline: T0 + 24 months

WP4:

Objective: Comprehensive market study of high-power LPA-based technology

Deliverable: Detailed report

Contributor: DF Photonics Consulting

Timeline: T0 + 24 months

WP1 was successfully completed by the end of 2023.

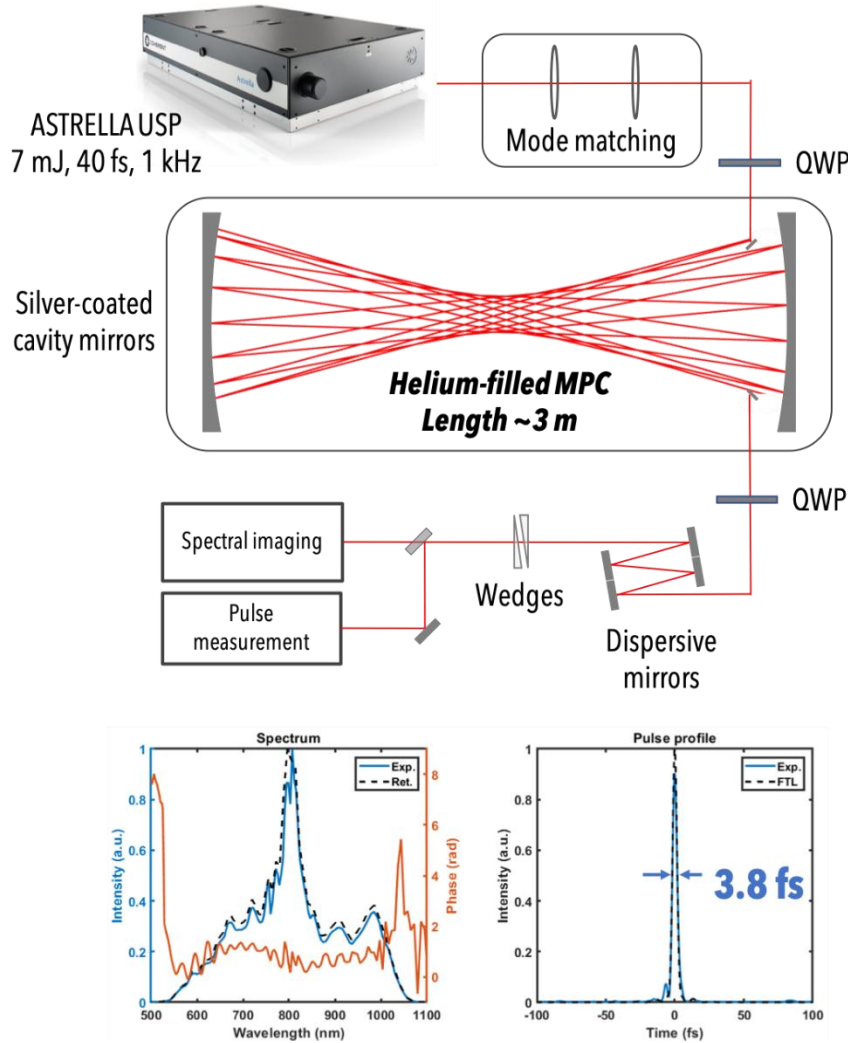


Figure 26. Top: MPC post-compression setup for the ASTRELLA USP laser. Bottom: spectral and temporal profile of the post-compressed pulses (QWP: Quarter Wave Plate).

Figure 26 shows the MPC compressor setup designed for the ASTRELLA USP Ti:Sa laser as well as the spectro-temporal properties of the post-compressed pulses. After 28 passes in a 3-m long MPC filled with 1.8 bar pressure of Helium gas, the 7 mJ 40 fs input pulses were successfully post-compressed down to 3.8 fs duration with 60 % compression efficiency (4.2 mJ measured directly at the output of the MPC) and > 99 % spatio-spectral beam homogeneity. This is the shortest pulse duration (~ 1.5 cycle) ever measured out of an MPC compressor and the overall performance of the MPC post-compressor is comparable to that achieved with our state-of-the-art waveguide post-compressor [10] used for LPA operation at LOA. It is interesting to note that this performance was achieved using cheap « off-the-shelf » silver-coated mirror technology, implying that even higher throughput could be achieved using customized mirror coatings with higher reflectivity.

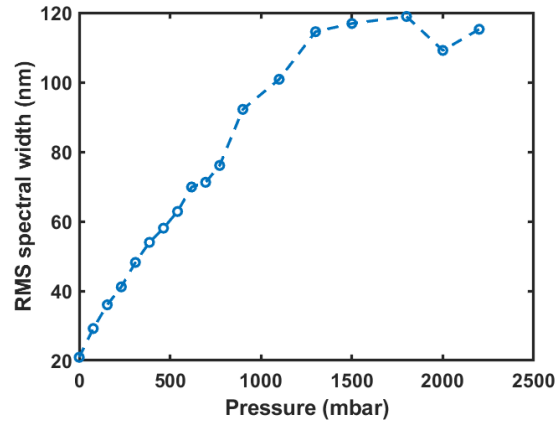


Figure 27. Spectral broadening of the post-compressed laser pulses as a function of gas pressure inside the MPC.

Another interesting result can be seen in Figure 27, which shows the evolution of nonlinear spectral broadening as a function of increasing gas pressure inside the MPC. Optimal post-compression occurs around 1.8 bar pressure, beyond which pulse quality starts to degrade due to the onset of higher order nonlinear spatial effects. This constitutes a universal way setting the fixed-point operation mode of the MPC post-compressor. This successful and encouraging milestone led to a high impact publication in 2024 [18].

WP 2 was only partially completed by the end of the project

This work package suffered significant delays because of the following:

1. delayed delivery and compliance defects of the MPC vacuum chambers by the supplier, who was selected for its lower cost and performance track record. The finalized chambers were found to be fully compliant with our MPC design, albeit delivered > 6 months later than initially planned.
2. Beam stability issues with the MAGMA 25 laser on loan from Amplitude Laser Group (ALG), which were not identified during the installation and worsened with time. These issues were temporarily solved after 6 months by ALG, making the laser sufficiently stable for experiments during the second half of 2024 only. A more long-term solution shall be implemented by ALG during 2025.

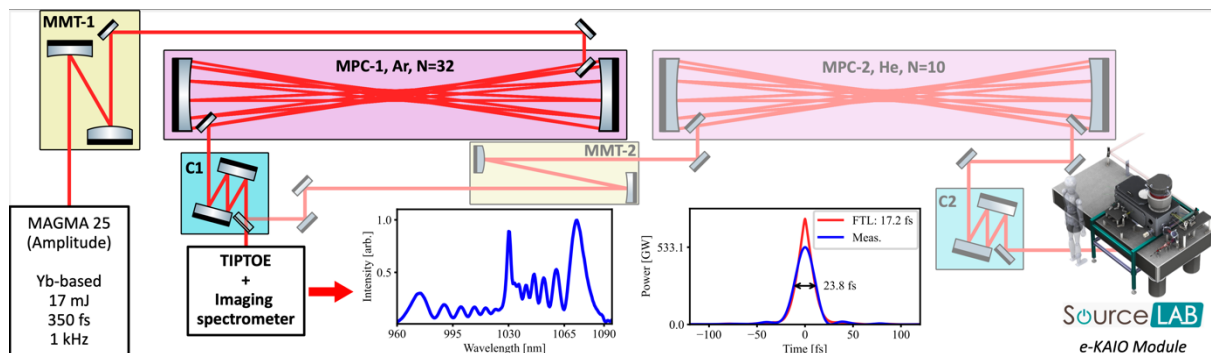


Figure 28. Cascaded MPC post-compressor architecture designed for the MAGMA 25 laser. Bottom: spectrum and temporal profile of the post-compressed pulses out of the 1st stage.

Figure 28 shows the final MPC design adopted for the MAGMA 25 laser specifications (18 mJ, 250 fs, 1 kHz). The cascaded layout chosen because of the near 100 compression factor required [Balla], comprises two consecutive MPC stages: the first is based on high-reflectivity high damage threshold dielectric mirrors adapted highly efficient for post-compression down to 20 fs pulse duration. This approach allows the use of smaller and therefore more intense beam footprints on the cavity end-mirrors without optical damage, and therefore considerably reduces the overall size of the MPC. The second is based on more lossy broadband silver-coated mirrors to reach the few-cycle regime, analogous to the MPC design implemented for the ASTRELLA USP.

As shown in Figure 28, after 32 passes in a 4-m long MPC filled with 0.5 bar of Argon has, the initial 17.3 mJ, 350 fs pulses were post-compressed (at full energy and under vacuum) down to 20 fs duration with with > 98 % compression efficiency. A high-impact publication is in preparation to report this record efficiency for a multi-mJ kHz Yb-based laser. Although this first stage was only implemented at the end of 2024, and no milestone was completed, these results remain extremely encouraging for the next stage. Procurement of materials for the second stage is still in progress and post-compression of the pulses from the first stage at full energy shall be tested during the course of 2025. Different strategies will be benchmarked aimed at controlling the post-compressed pulse quality for such high compression factors [19], such as nonlinear polarization rotation, which we have already demonstrated in an MPC at lower energy [20].

Due to the late start of the Yb laser post-compression experiments, the transport beamline from the MPC post-compressor to the radio-shielded LPA module has not yet been completed. Its design will depend on the final performance of the few-cycle MPC post-compressor stage. The procurement of basic mechanical and vacuum materials should start in 2025, but LPA experiments at full energy are not expected to start before 2026.

WP3 has not been completed but the collaboration between LOA and CNR-INO will remain active in the future

CNR-INO will prepare dosimetry protocols for the planned radiobiological studies [4] using the Yb-driven LPA at LOA. These will heavily depend on

- 1) the expected electron beam specifications and
- 2) available on-site support for biological endpoint evaluation. Radiobiological testing is expected to start after the completion of WP2 during 2026.

WP4 was fully completed at the end of 2024

2.5 DEVELOPMENT OF HIGHLY EFFICIENT MW CLASS CROSS FIELD VACUUM TUBE AMPLIFIER FOR PARTICLE ACCELERATORS DRIVEN BY A SOLID-STATE POWER AMPLIFIER AT 750 MHz

We have developed the computational model of CFA and various components. The cross-field amplifier is close to the fabrication process. Parallel to this, development efforts for field emitter and magnetic field systems are ongoing. Similarly, we are developing high-voltage insulation and RF windows using PEEK material in cross-field vacuum tube.

We have modelled the cross-field amplifier using the commercially available simulation tool CST studio suite. Fig. 29 (a) and (b) show a cross section view of the CFA model also in CST. Figure 29 (c) shows the detailed model prepared for the fabrication process and realized in Solidworks for fabrication.

Modelling and RF Propagation Study

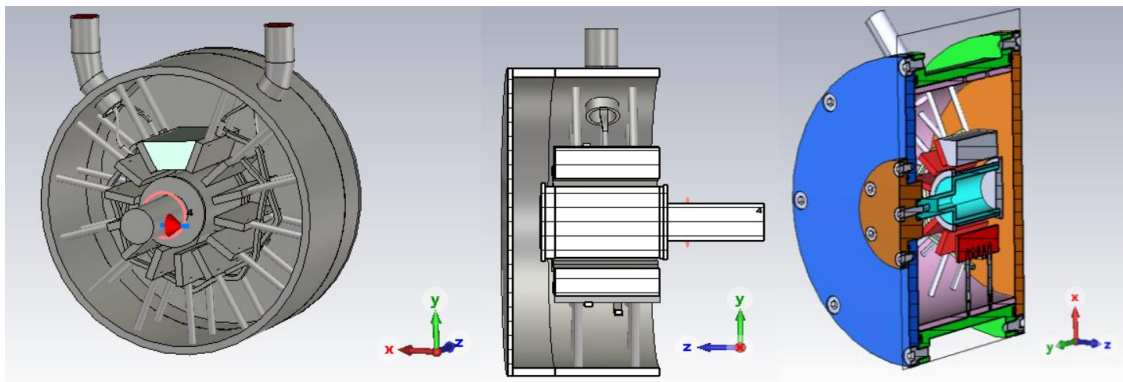


Figure 29. Electromagnetic Model of cross-field amplifier (a) Tilted Transverse Cut (b) Longitudinal Cut (c) Solid Work model for Fabrication

A cross-field amplifier's beam wave interaction study has been investigated, and particle preview is shown in Figure 30 (b). The beam wave interaction predicts 600kW of RF power. The RF power will develop at 713 MHz, as shown in Figure 31 (a). This requires a voltage of -30kV and magnetic field of 0.25 T, the anode current of 100 A is developed. The calculated gain is 27dB, and the efficiency is 20 %.

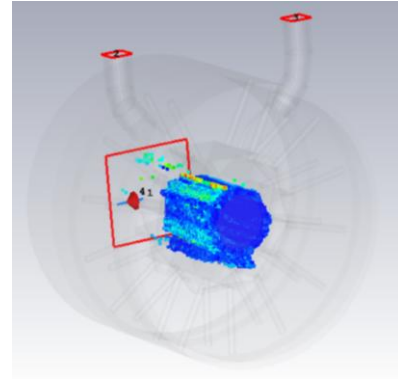
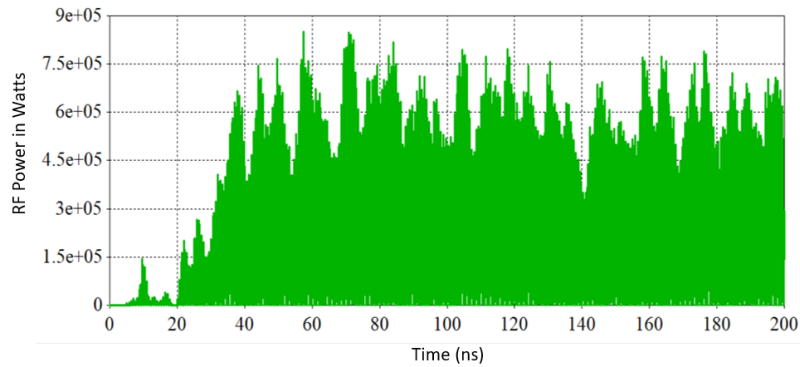


Figure 30 (a) Temporal response of RF power, Figure 30 (b) particle preview of the cross-field amplifier

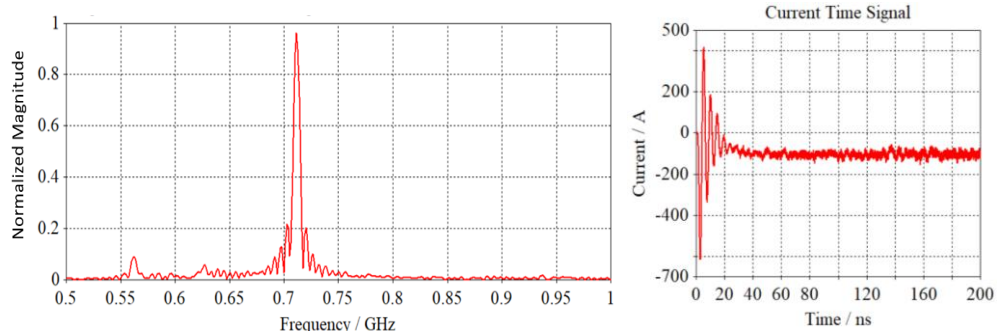


Figure 31 (a) Frequency response of developed RF power, Figure 31 (b) current developed in the cross-field amplifier

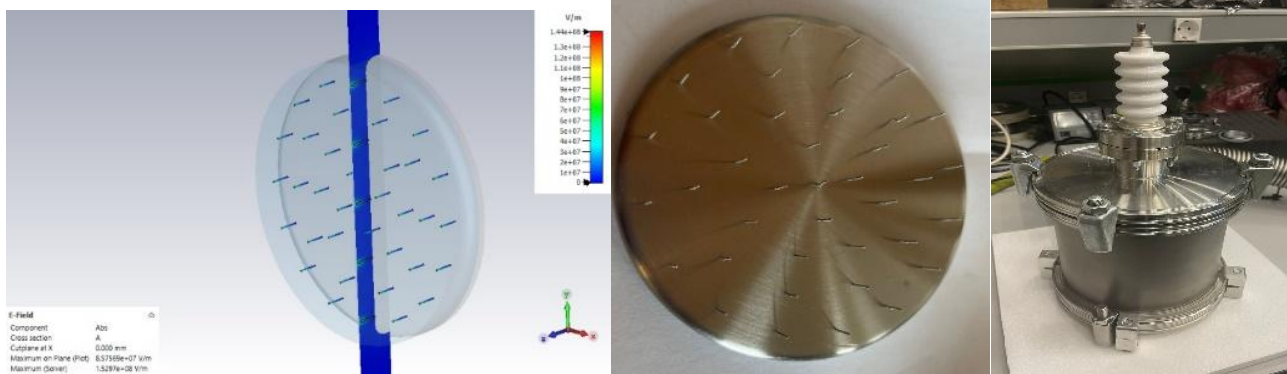


Figure 32 (a) Electric field distribution of field emitter with 30 kV potential difference Figure 32 (b). 3-D printed electron emitter developed at Uppsala University Figure 32 (c). Anode- cathode chamber to test field emitter

Contribution and work performed by each beneficiary/industrial partner

Component	Work	Beneficiary
Slow Wave structure	Design and Modelling	Uppsala University
Magnet System design	Design and Development	Uppsala University
Field Emitter	Design and Development	Uppsala university
Cross-field Amplifier	PIC simulation and Fabrication	Uppsala university
M 100 modulator-based pulse power supply	Purchased	Scandinova AB
Bidirectional coupler, waveguides, RF transitions	Purchased	Exir Broadcasting AB

Other components, such as Circulator, RF load, electromagnet for vacuum tube and other MW components will be purchased from AEP int, The Netherlands and AFT, Germany.

Sustainability and environment impact

The project significantly enhances sustainability and reduces the environmental impact of particle accelerator technologies by improving the efficiency of RF power generation, reducing energy consumption, and minimizing material waste. By replacing traditional filament-based electron emitters with field emission-based electron emitters, the need for heater assemblies is eliminated, leading to lower power consumption and higher RF output per unit of input power. Additionally, the reduced heat load lowers cooling system requirements, cutting down on infrastructure energy costs and enabling more compact accelerator designs. The technology also reduces reliance on critical materials like tungsten and barium oxide, contributing to a smaller environmental footprint while extending the operational lifespan of vacuum electron devices, thereby minimizing electronic waste. Furthermore, this innovation supports green energy applications, including hydrogen production, industrial microwave heating, and radiological treatment, making high-power RF sources more energy-efficient across multiple sectors. Lastly, by ensuring longer operational life and modular designs, the project facilitates easy recycling and repurposing of accelerator components, further reducing electronic waste and the overall environmental impact.

2.6 MILLISECOND FLASH LAMP TREATMENT FOR SRF ACCELERATING CAVITIES

Nb3Sn is one of the state-of-the-art SC materials with high potential for the SC-cavity operated at 4 K. The main goal of FLA project is the development of the technology for the fabrication of 6 GHz cavity made of copper and high TC coatings. The Nb3Sn coating is deposited by magnetron sputtering at elevated temperature. Due to thermal instability of copper at high temperatures the maximum allowed temperature for thin film deposited is about 650 °C that limits the performance of coating film. Therefore, the post grown thermal annealing is required. Within the project we have tested the

ms-range flash lamp annealing (FLA) for improvement of the coating crystallinity without affecting basic properties of copper substrate. Due to very short annealing time, in particular below 25 ms the peak temperature in coating layer can significantly exceed the 650 °C without activation of Cu diffusion that is the main drawback of high temperature annealing. Scientific community is exploring in parallel other materials that can be used as the coating in Cu-cavities. The group of transition metal nitrides like NbN and TiNbN are developed simultaneously with Nb₃Sn technology, and the final material of choice will be selected based on the best cavity performance. NbN and NbTiN samples produced by I.FAST WP9 partners are investigating in this project as well as Nb₃Sn.

Progress and achievements

Design, production and test of the annealing chamber for high-temperature treatment of Cu-cavity by FLA

The main task of the project was to design and test the flash lamp annealing system for the high temperature thermal treatment of superconducting cavities made of copper coated with superconducting layer. The coating is made by magnetron sputtering of Nb₃Sn. The temperature needed for the high quality Nb₃Sn layer deposition is above the softening point of Cu that is below 600 °C. Thermal annealing of Cu above 600 °C causes structural changes of copper that can lead to uncontrollable deformation or even damage the cavity. Therefore, it is expected that ultra-short post-deposition thermal processing of SC-coating like Nb₃Sn will improve the coating crystallinity without affecting the Cu-substrate properties.

The FLA chamber for annealing of the SC-cavity was fabricated and delivered in May 2024. In the recent project period, we focused on the testing of the FLA chamber i.e. vacuum level, preheating system, temperature calibration etc. Finally, the first tests on the Cu-cavity with and without SC-coating was performed. Figure 33 shows the external and internal view of the chamber including instrumentation.

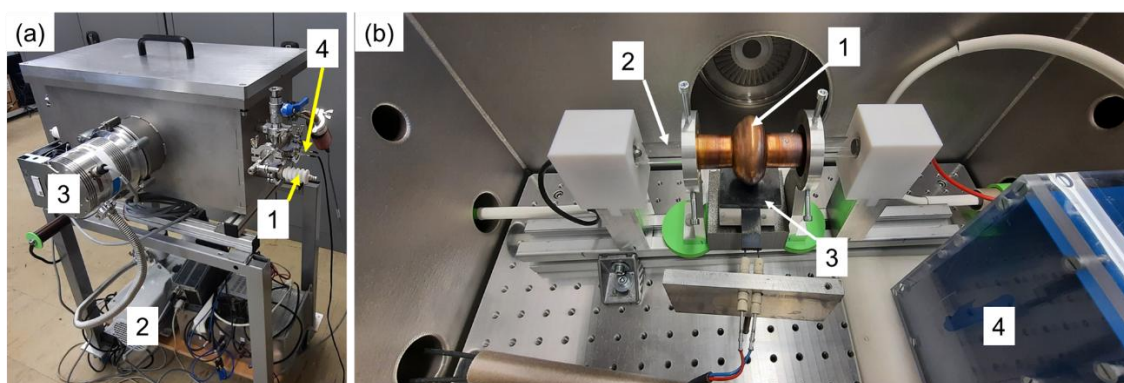


Figure 33. Flash lamp annealing system for the high temperature treatment of 6 GHz or 1.3 GHz cavities. (a) shows the external view of the FLA chamber. 1 and 4 shows the electrical connections to the Xe-lamp and preheating system, respectively, while 2 and 3 are pre-vacuum and turbo-molecular pumps, respectively. (b) shows inner view into the chamber. 1 is the 6 GHz cavity, 2 is the Xe-lamp, 3 is the preheating plate and 4 is high voltage ignition system for the Xe-lamp.

The typical operating voltage of an Xe lamp is between 2 and 4.5 kV. This requires a high-voltage insulation system compatible with the vacuum chamber. Here we have used porcelain vacuum

connectors tested up to 20 kV (1 in Fig. 30a). The preheating system requires rather moderate voltage but high current, so the electrical connectors are much different and marked to market with 4. Numbers 2 and 3 in Fig. 30a indicate the pre-vacuum and high vacuum system. The pre-vacuum is achieved with a conventional rotary pump, while the high vacuum is achieved with a molecular turbopump. The final vacuum level is below 10^{-6} mTorr. Figure 30b shows an internal view of the chamber. 1 state for the 6 GHz cavity under test. The Xe lamp is indicated by number 2. Number 3 shows the hotplate used to preheat the cavity. The preheating will be used to desorb air and water once the cavity is installed in the chamber and ultimately to increase the cavity temperature before the final flash. 4 is the ignition system for the Xe lamp, which operates at approximately 20 kV. The high-power discharge is provided by external power supply. The current configuration has been used to anneal a 6 GHz cavity but can easily be upgraded to a 1.3 GHz cavity. In order to anneal a higher volume cavity, the Xe lamp will be replaced with a longer one. Replacing the lamp is like a plug and play system. The other parts of the cavity remain the same. The system was tested using Nb coated and uncoated 6 GHz Cu-cavities. First, the preheating system was tested. The temperature in the cavity was measured by thermocouple directly mounted on cavity. The target temperature is 450 °C that was achieved after 10 min in vacuum. The temperature of the coating during the flash lamp annealing cannot be measured in-situ due to slow response of the thermocouple. The influence of the flash annealing on the coating will be tested soon using post annealing experiments.

- FLA-chamber is designed, fabricated and tested at HZDR.
- 6 GHz cavity is fabricated by INFN and annealed at HZDR.

FLA on Nb₃Sn on planar Cu-substrate

Development work on Nb₃Sn coatings in WP9 has shown that a process $T \geq 600^\circ\text{C}$ is required to achieve $T_c > 17\text{K}$, with a buffer layer of Nb ≥ 30 microns. Previous results on planar samples of Nb₃Sn, showed the ability of FLA to improve the crystal structure of the coating. At the same time, however, it was seen that the improvement produced by FLA is not sufficient on samples sputtered at $T \leq 400^\circ\text{C}$, because they remain to be non-superconductive. Therefore, it was thought to evaluate the possibility of using FLA to reduce the working T and/or the buffer layer thickness starting from samples that already exhibit a T_c , although not optimal.

A new series of samples grown at $T=500^\circ\text{C}$ and $T=550^\circ\text{C}$ were made at LNL, with two different buffer layer thicknesses, 9 and 30 microns respectively. These samples exhibit a T_c between 13.5 and 15.4 K. HZDR is currently characterizing the samples before irradiation with positron annihilation and then will proceed to FLA treatment in order to improve the crystal structure and raise the T_c .

Sample #	Buffer Layer Thickness	Process T (°C)	T _c (K)
34A	30	500	14.09
35A	9	550	15.41
37A	30	500	13.58
37B	9	500	13.48

Table 2. Nb₃Sn samples coating parameters and T_c as coated (before FLA)

New Nb₃Sn samples will also be produced directly at HZDR, which will have the ability to deposit via DC-MS the copper samples and then proceed to in situ FLA treatment. For these tests, LNL treated 5 copper substrates with SUBU and delivered to HZDR in January 2025. The first results are expected by April 2025.

- 4 samples made at LNL.
- Ongoing Characterizations at HZDR.
- 5 Cu SUBU samples at LNL
- Testing on Sputtering System in Progress at HZDR

FLA on NbTiN and NbN coatings

Similar to Nb₃Sn, the metal nitrides suffer from the defects and strain. The post-deposition flash lamp annealing is one of the methods used for the strain and defect engineering. In cooperation with Prof. Claire Z. Antoine from CEA Saclay, we have shown that the FLA for 23 ms at energy density of 130 Jcm⁻² can synthesize the crystalline phase of TiNbN deposited on silicon substrate by magnetron sputtering at room temperature. Moreover, the project partner from HZDR have installed and tested the magnetron sputtering system equipped with in-situ FLA for deposition of Nb₃Sn and metal nitrides. The first test made on the NbN layer deposited on Si shows significant changes of the crystal properties of the layer after FLA (see Figure 34)

- 2 samples FLA treated at HZDR

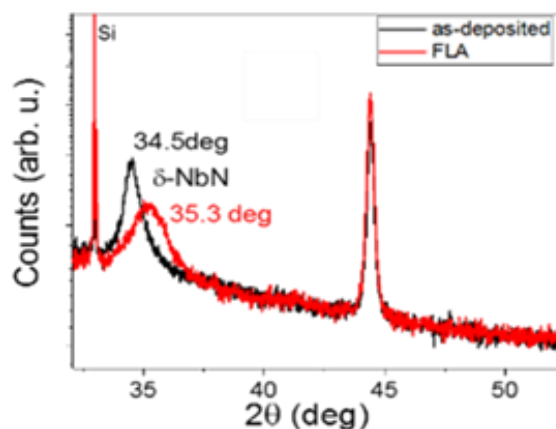


Figure 34. XRD data from NbN layer made by magnetron sputtering and FLA

Fabrication of Cu-cavity with Nb-coating

A Cu cavity produced by Piccoli has been polished and coated with a Nb thin film layer of 3 microns at LNL. Instead of the optimized high temperature coating recipe, a low temperature coating has been performed in order to test the ability of FLA in improved crystallinity and cavity quality factor.

The cavity has been RF tested at 4.2 K and show a quality factor of $3 \cdot 10^6$. We expect that the FLA can increase the Q up to $1 \cdot 10^7$, typical of high temperature coating.

- Cavity spun by Piccoli Srl
- Polishing, coating and baseline RF test made by INFN.
- FLA expected in March-April at HZDR

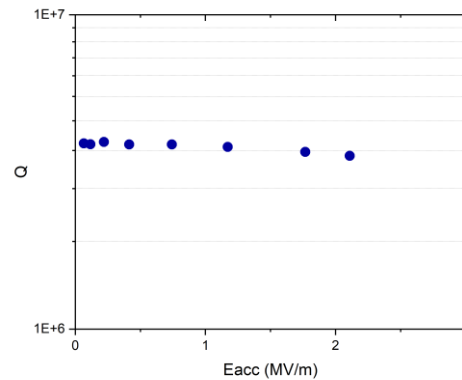
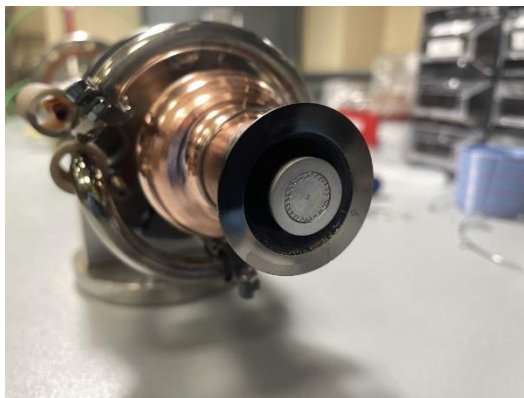


Figure 35. On the left a Nb on Cu 6 GHz cavity coated at LNL. On the right the Q VS E_{acc} RF characterization of the 6 GHz cavity before FLA treatment.

Sustainability and environment impact

The contribution is double.

1. In elliptical cavities large cryogenic power is required to operate the cavities at 2 K, and in some accelerators can even be on the order of MW, resulting in one of the most important operational costs of an accelerator in terms of electrical grid power. The use of superconductors with higher T_c than that of Nb, such as Nb_3Sn or $NbTiN$, allows operation at higher operating T with two major advantages:
 - strong suppression of BCS even at operating T above 4 K;
 - higher efficiency of cryogenic systems.

Therefore, replacing Nb cavities with higher T_c cavities would allow a large reduction (about 60%) in the electrical power requirements of the cryogenic plant. In addition, by working at 4.2 K and thus at atmospheric pressure, there is a reduction in the size and cost of the plant itself, with strong simplification and operational advantages.

2. FLA annealing is defined as a system that uses significantly less energy than conventional annealing methods such as rapid thermal annealing or furnace annealing. Given the same

temperature and coating performance, FLA is approximately 30% cheaper than conventional annealing, which means a significant reduction in CO₂ emissions and electricity consumption. FLA also has a significant economic impact in various disciplines. Considering low-emissivity glass coatings (one of the activities of HZDR), treating the coating with FLA costs about 15 cents/m², while conventional annealing is between 30 and 70 cents/m². Therefore, the use of FLA to functionalise high-temperature SC coatings is important and should be investigated in depth.

2.7 AM APPLICATIONS OF REFRACTORY METALS FOR ION SOURCES

The objective is the development of FEBIAD-like ion sources via Additive Manufacturing (AM) technology, exploring the possibility of improving some specific aspects, such as the reliability of the assembly procedures and the ionization performance.

BENEFICIARY: INFN - Padua Division

Production of Refractory Metals samples and components by AM Technology

Pure Ta and Nb samples production for electrical and thermal characterization:

Once the parameters had been finely tuned to yield samples with high density, specimens were manufactured for the thermal and electrical properties characterization.

Figure 36(a) shows the geometry of the specimen, specifically designed to ensure a uniform temperature distribution in its central section, where the potential drop is measured using a voltmeter, and the temperature is recorded using a pyrometer and two thermocouples (see Figure 36(b)). The optimal sample geometry was determined using ANSYS® software, through combined electro-thermal analyses that considered various geometries for both the specimen and the copper clamps used for sample support and current supply. Figure 36(c) displays the Ta samples produced by Laser Powder Bed Fusion in the DIAM lab. The specimen's axis is aligned parallel to the building platform. Identical geometries were also produced in pure Nb.

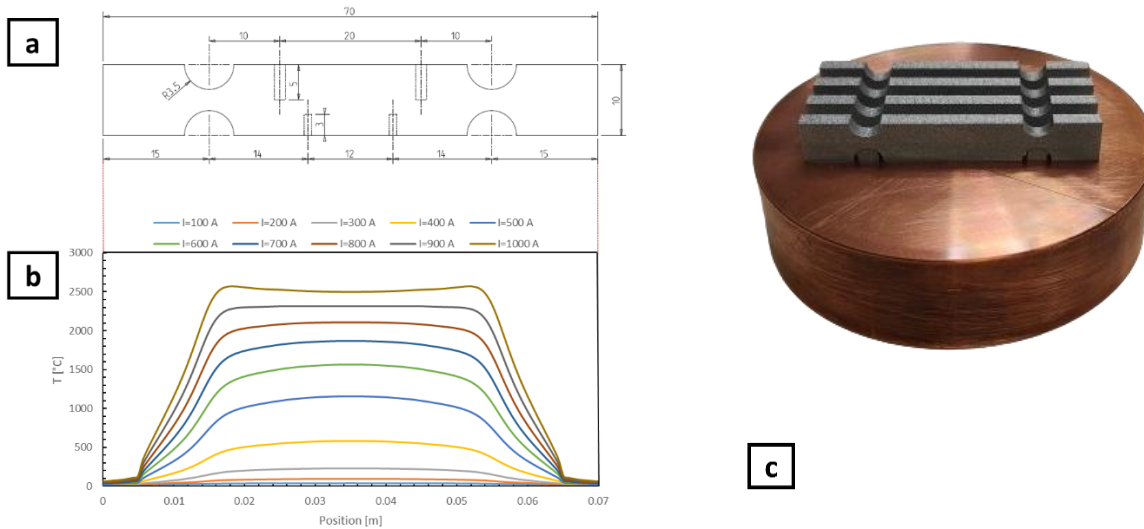


Figure 36. (a) Final geometry used for electrical resistivity estimation and (b) the corresponding homogeneous temperature trend in the useful area. (c) Ta produced samples.

Pure Ta components production for tests

The components of the FEBIAD type ion source redesigned according to the rules of the Design for Additive Manufacturing (DfAM) and the components for the Thermionic emission test set up were additively manufactured utilizing the EOS M100 available at the DIAM lab. These components were produced using the fine-tuned process parameters. Figure 37 illustrates the several components production.





Figure 37. Set of photos of the FEBIAD-type ionization source components and the Thermionic emission test setup additively manufactured in Ta at the DIAM lab.

Development of Refractory Metals alloys by AM Technology

Ta-10W development:

Process parameter optimization is essential for achieving high-density components through Additive Manufacturing (AM) technology, particularly Laser Powder Bed Fusion (LPBF) processes. The EOS M100 machine, located at the Development and Innovation on Additive Manufacturing (DIAM) laboratory of the INFN Padua Division, was utilized for this purpose.



Figure 38. EOS M100 System used for the LPBF process of pure Ta.

The outcomes of the first stage of the components production for process parameter optimization procedure are illustrated in figure 39. This production, aimed at refining the process parameters for the fabrication of the Ta-10W alloy, paves the way for future activities in thermal, electrical, and mechanical characterization.

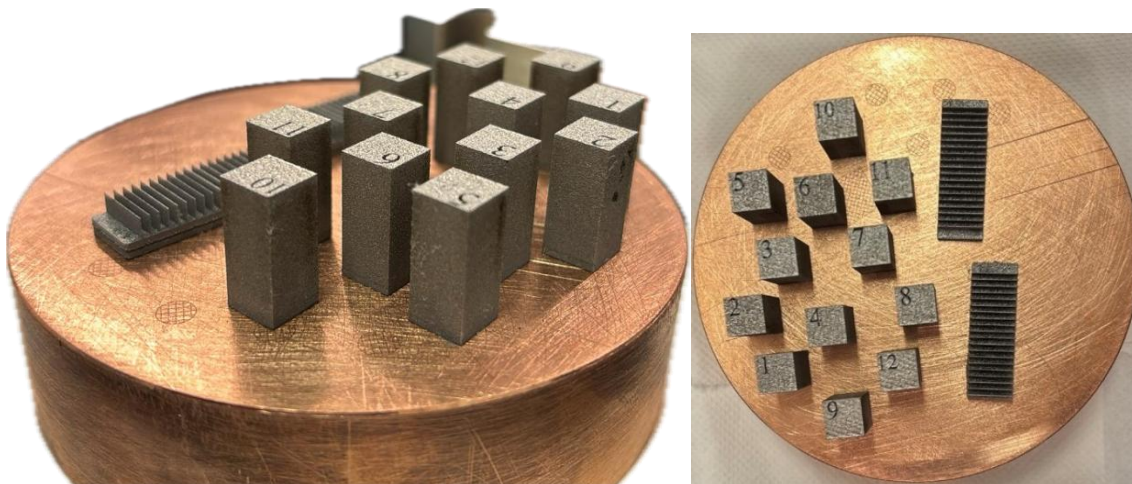


Figure 39. First successful production of Ta-10W samples for process parameters fine tuning.

BENEFICIARY: INFN-LNL

Pure Nb characterization

The samples produced at INFN-PD were characterized in terms of thermal and electrical properties in the 600-2000 °C temperature range and the achieved results were compared with corresponding literature data for standard Nb. For the thermal characterization, disk shaped specimens were utilized in a custom characterization furnace available at LNL. Within the furnace, the sample is heated by thermal radiation with an opportunely ohmic resistor, capable of reproducing a radial temperature pattern on the sample disk, with a hotspot at the specimen centre and the lowest temperature at the periphery. The furnace is equipped with observation windows, from where it is possible directly measure the sample centre and periphery temperatures by means of infrared pyrometers for each heating power level. Thermal conductivity is then estimated by means of a numerical model reliably reproducing the test furnace. Within the model, the sample thermal conductivity, which is the only unknown property, is varied until the numerically calculated temperature matches the corresponding experimental values.

The electrical characterization was conducted on bar-shaped samples that were directly heated by Joule effect. The sample temperature was monitored through an infrared pyrometer, whereas the potential drop at the edges of the sample gauge length was measured by means of a voltmeter. With this kind of information, the calculation of the temperature dependent electrical resistivity was possible.

Figure 40 provides an overview of the measured properties of LPBF Nb, compared with literature data. It is possible to observe that LPBF Nb exhibits a lower thermal conductivity and a higher electrical resistivity if compared to the literature standard Nb. Such effect is most likely ascribable to the unavoidable presence of defects within the LPBF material microstructure.

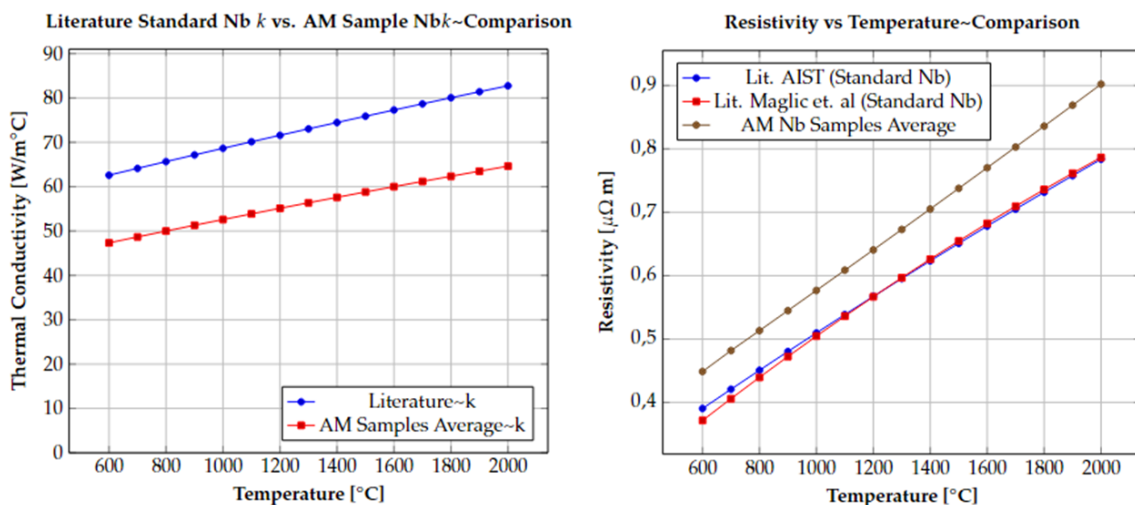


Figure 40. Comparison of the thermal conductivity and electrical resistivity of the AM (LPBF) Nb samples and corresponding literature data for standard Nb.

Pure Ta characterization

Similarly to Nb, also Ta was characterized in terms of thermal and electrical properties in the 600 °C-2000 °C temperature range. For the electrical characterization the same approach described for Nb was utilized, whereas the estimation of the thermal conductivity was performed according to the Wiedemann-Franz equation that correlates the electrical resistivity with the thermal conductivity. The achieved results are reported in figure 41, together with corresponding literature data. Also in this case, it is possible to highlight a lower thermal conductivity and a higher electrical resistivity for the LPBF Ta if compared to the literature standard Ta. This effect can be associated with the more distorted microstructure of LPBF Ta respect to standard Ta.

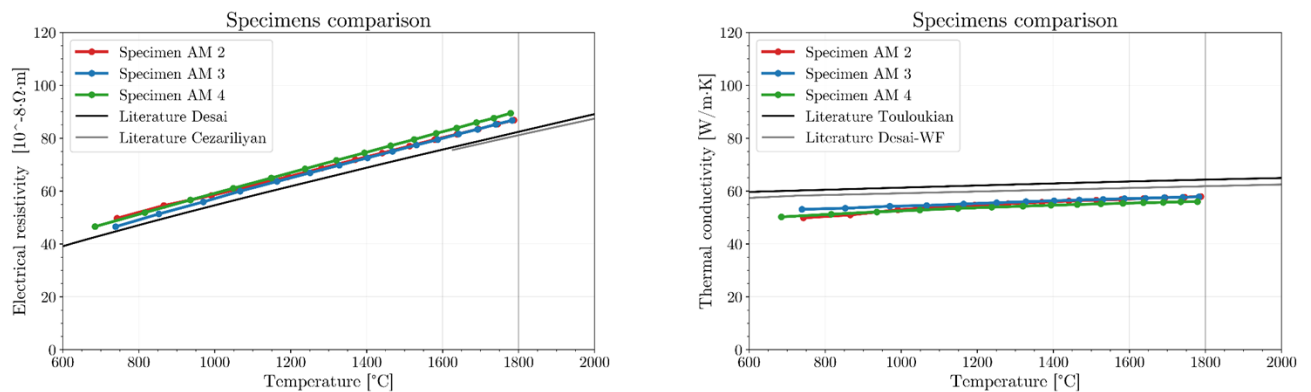


Figure 41. Comparison of the thermal conductivity and electrical resistivity of the AM (LPBF) Ta samples and corresponding literature data for standard Ta.

Online and offline testing of the FEBIAD ion source at the SPES facility

The offline tests performed at CERN with a FEBIAD ion source including a LPBF tantalum components proved the suitability of this technology for the production of working ion source components. For such reason, a FEBIAD ion source including a LPBF tantalum cathode was employed coupled with a silicon carbide target to produce the first SPES radioactive ion beam. Figure 42 exhibits the HPGe spectrum recorded for the mass 28 amu beam extracted for the SPES commissioning with radioactive ion beam. It is possible to observe the presence of a 1778 keV peak, corresponding to the decay of the radioactive isotope ^{28}P , confirming the actual ionization of radioactive species with the LPBF cathode.

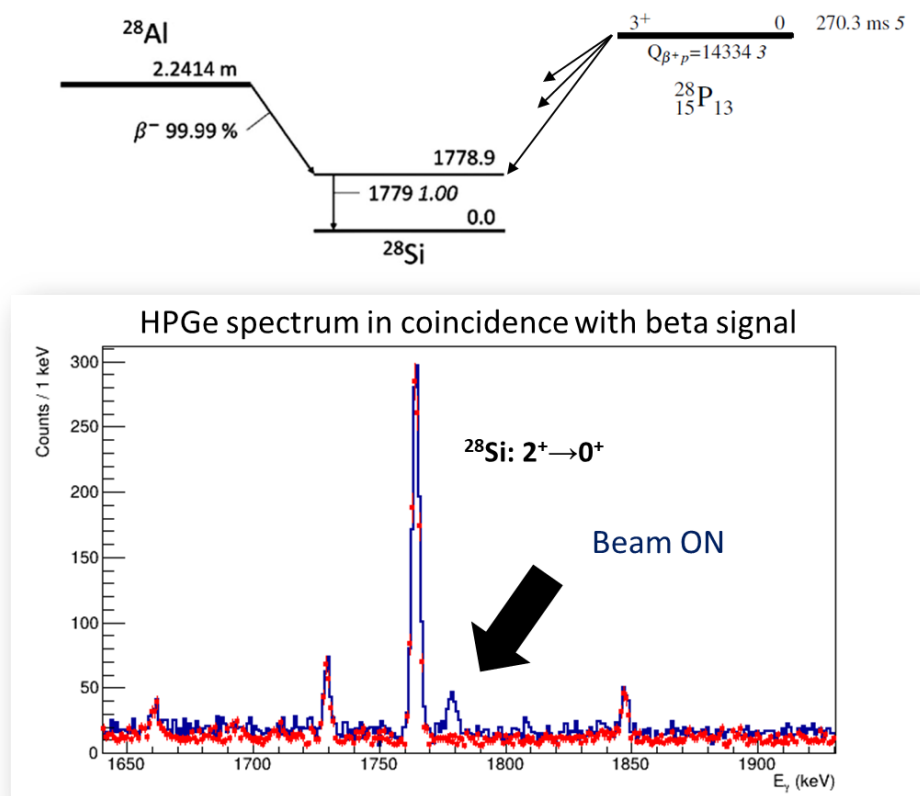


Figure 42. the HPGe spectrum recorded during the SPES commissioning test with the production of the first mass 28 amu radioactive ion beam.

After such important milestone for the SPES project, the FEBIAD ion source employed for the production of the first radioactive ion beam was characterized in detail by injecting a flow of neutral stable atoms of noble gases, with the aim to evaluate the ionization efficiency and the optimal working conditions. Figure 43 reports the typical mass scan recorded when the ion source was fed with a controlled flow of a gas mix including 20% He, 20% Ne, 20% Ar, 20% Kr, 20% Xe. The capability of ionizing all the injected elements is confirmed by the clear presence of the masses corresponding to each of the stable isotopes of the injected elements. In addition, by varying the ion source working parameters, such as the cathode heating power, the anode voltage and the magnetic field intensity, it was possible to identify the optimal working condition maximizing the ionization efficiency for each of the injected elements. Figure 44 reports an example of the typical $^{40}\text{Ar}^+$ beam current pattern observed by varying the anode voltage and the magnetic field.

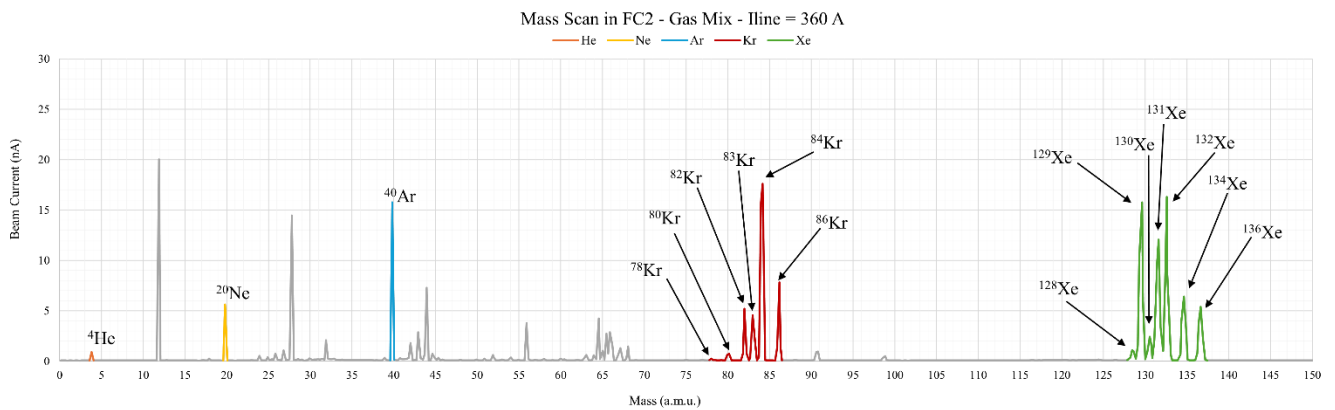


Figure 43. Typical mass scan performed when the ion source was fed with a controlled flow of neutrals from the noble gas mix. The stable isotopes of each of the injected elements are clearly visible.

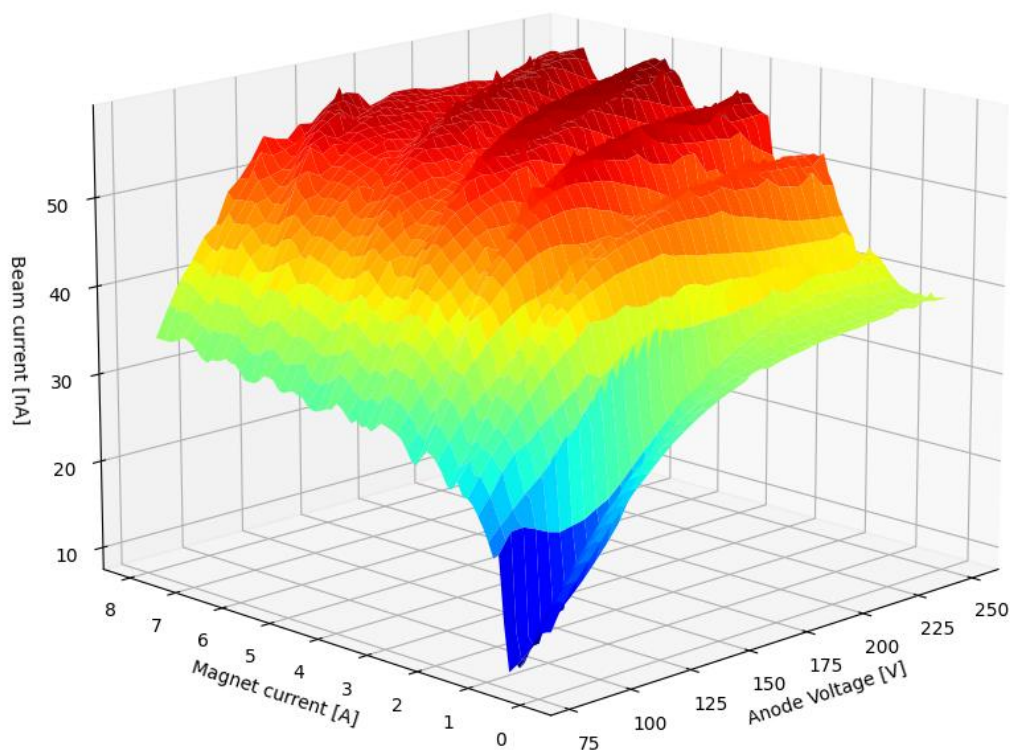


Figure 44. The typical $^{40}\text{Ar}^+$ beam current pattern observed by varying the anode voltage and the magnetic field.

Thermionic emission testing of tantalum cathodes

The offline and online testing of the FEBIAD ion source including a LPBF tantalum cathode highlighted an increased thermal electron current respect to the standard cathodes. The availability of a higher intensity of emitted electron current has a beneficial effect on the

overall ion source performance, therefore, in order to further investigate the factors that affect the thermionic emission, a dedicated set-up was developed and tested (figure 45). Such set-up consists of modified FEBIAD ion source, where:

- two observation holes allow for the real-time direct monitoring of the cathode temperature and anode-cathode relative position.
- A probe is inserted into the anode to collect the portion of the thermionic emission electron flux entering the anode hollow volume without intercepting the anode grid and walls (namely the electron portion available for the ionization).

The parameters of interest that were studied in detail were:

- The influence of the cathode surface finishing
- The influence of the anode surface finishing
- The influence of the anode grid geometry, comparing the standard grid pattern respect to a pattern designed by TRIUMF
- The comparison between LPBF and standard cathodes

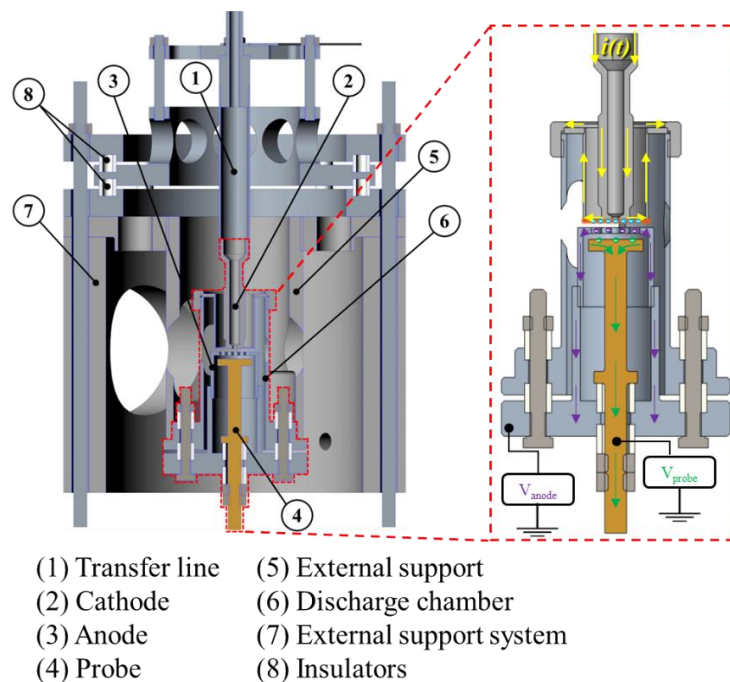


Figure 45. The setup for the thermionic emission tests.

According to the performed tests, no correlation between the anode surface finishing and the thermionic emission was highlighted, whereas the rougher the cathode surface, the higher the

emitted electron current intensity. From the comparison between the standard cathodes (STD) and the LPBF cathodes tested under equal conditions (same temperature, same surface finishing) it was possible to highlight that the thermionic emission for the LPBF component is higher. A possible explanation of this difference could be identified in the finer microstructure of the LPBF component, but further analyses are necessary to deeper investigate this effect. The comparison for the two kind of cathodes is reported in figure 46.

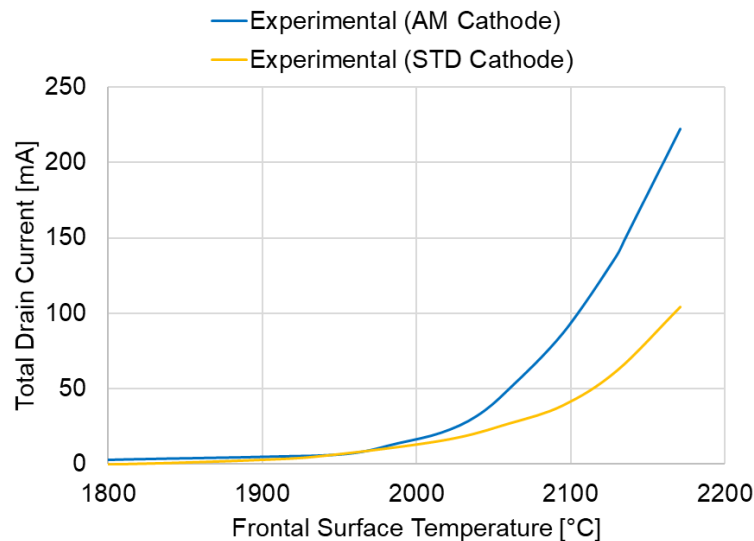


Figure 46. Comparison between the total emitted electron current for the standard (STD) cathode and the LPBF (AM) cathode.

BENEFICIARY: CERN (Isolde Facility, Off-line System) – INFN-LNL

TEST off-line

A first version of an ion source including several additively manufactured tantalum and molybdenum components was assembled and tested at the offline test bench of the ISOLDE facility at CERN (CH). Such ion source included LPBF cathode (tantalum), a LPBF anode (tantalum or molybdenum) and a LPBF extraction that were produced with minor geometrical modifications respect to the standard parts produced by subtractive traditional techniques.

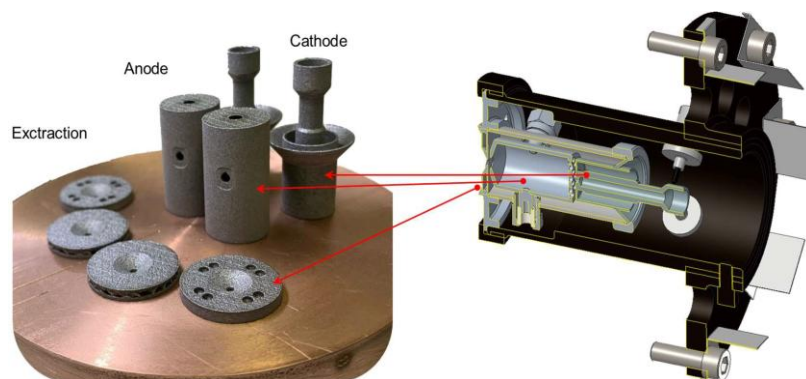


Figure 47. LPBF components employed for the FEBIAD ion source tested at the ISOLDE offline facility.

Several tests were conducted and a procedure for the fully characterization of an ion source was defined for the first time. In particular such experimental route foresaw the high temperature calibration, the measurement of the anode drain current, the evaluation of the ionization efficiency for noble gasses such as Ne, Ar, Kr and Xe and the assessment of the extracted beam emittance. Respect to a standard ion source, the tested prototype exhibited higher anode drain currents under equal working conditions, furthermore similar ionization efficiency and emittance were achieved.

Additionally, once the optimal operative conditions were identified, the tested prototype was continuously run for more than 15 days. Such successful experimental campaign paves the way for the further development of optimized ion source components with free-form geometries.

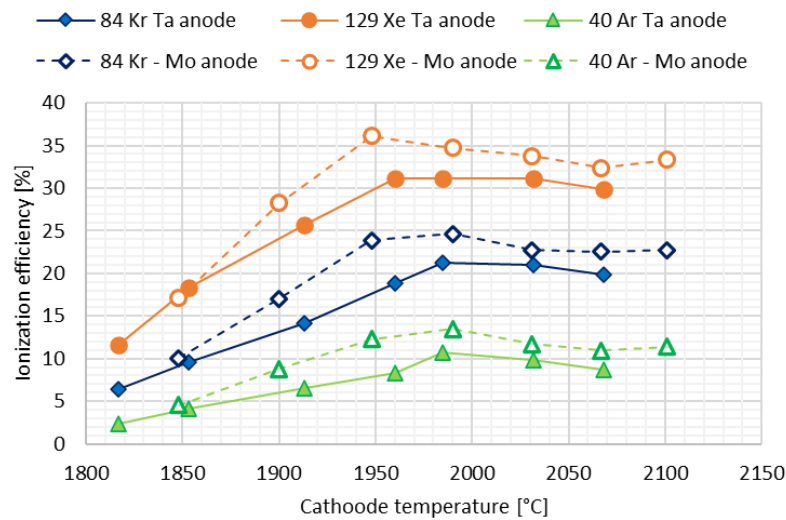


Figure 48. ionization efficiency for Ar, Kr and Xe as a function of the ion source heating current.

PARTNERS:

➤ TRIUMF

TRIUMF proposed a novel geometry for the anode grid, namely the surface facing the cathode. Such design was produced at INFN-PD and. As illustrated in Figure 50, Small features are present in the optimal solution but were removed for AM production.

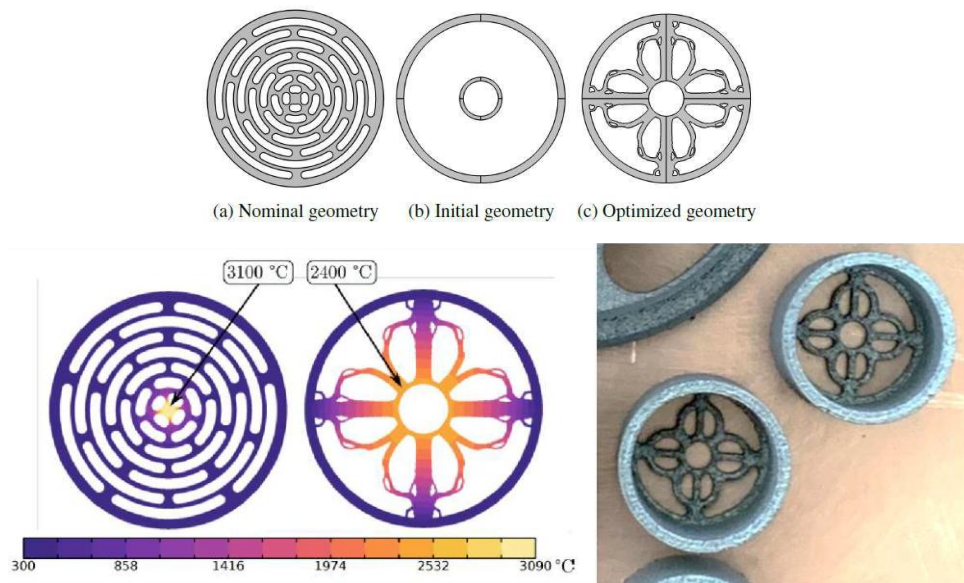


Figure 49. Geometry comparison for the generative design of the grid (top). Temperature contour plot comparison between nominal and improved grid design (bottom left). LPBF Production of the improved grid design. Small features are present in the optimal solution but were removed for AM production.

The TRIUMF anode grid was tested at INFN-LNL making use of the thermionic emission setup and compared with a standard grid in order to evaluate the transparency to the electron flux emitted by the cathode. It was possible to observe that the TRIUMF grid allowed for the transmission to the inner volume of the anode of 15% more electrons, suggesting a possible beneficial effect on the overall ion source performance.

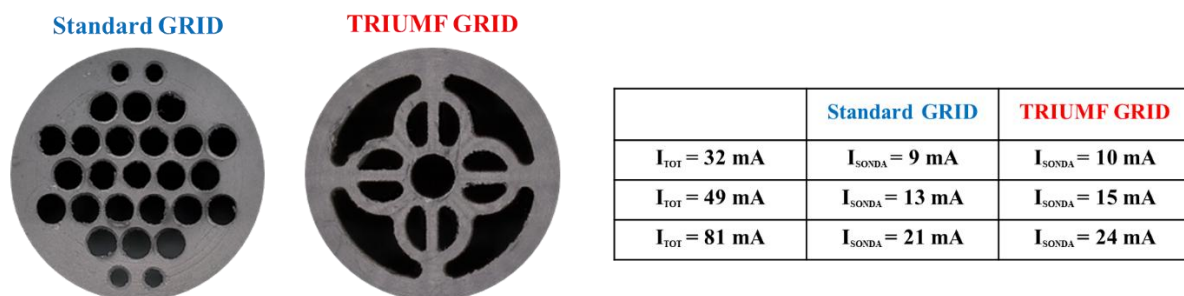


Figure 50. Comparison of the thermionic emission test results between the standard grid and the TRIUMF grid

➤ EOS Electro Optical Systems Finland Oy – EOS GmbH

The Turku division of EOS has extended support for the advancement of Ta-based and W-based refractory metals through an ongoing 6-month internship conducted by Silvia Candela, a PhD student at INFN-PD, at the agency's Finnish headquarters. The undertaken work enabled the testing of powder blends featuring various alloy element ratios and the production of samples with two primary aims:

1. Minimize cracks observed in additively manufactured pure W.
2. Generate defect-free samples with high density.

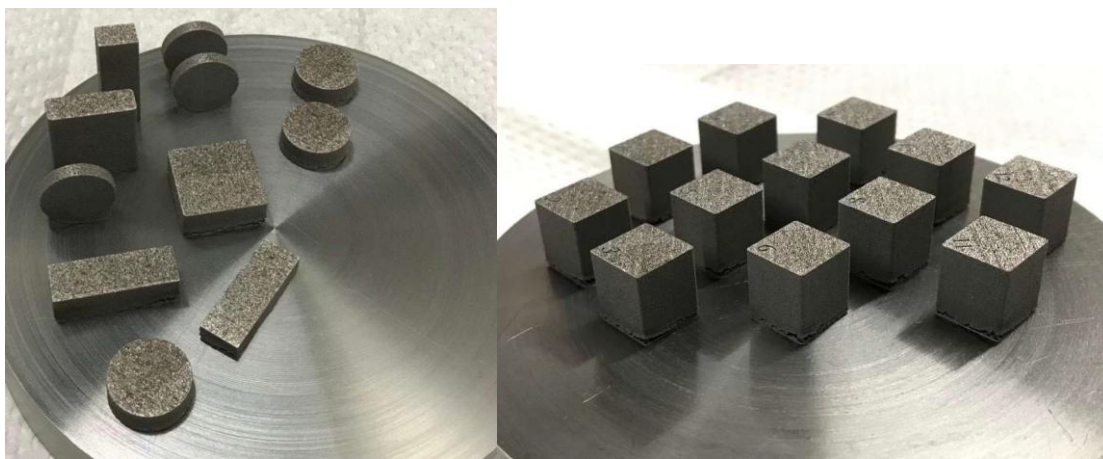


Figure 51. W-based alloys samples production performed at EOS Turku, Finland

➤ TANIOBIS GmbH

Offering pure Ta at a heavily discounted rate.

Offering 10 kg of Ta-10W free of charge.

➤ SAES group

Participation in project meetings aimed at initiating market analysis and exploring the potential for product commercialization.

2.8 DEMONSTRATION OF ADDITIVE MANUFACTURING FOR LARGE AND COMPLEX SHAPED VACUUM CHAMBERS BY PLASMA METAL DEPOSITION (PMD®)

The goal of the present project is the production of vacuum chambers using Plasma Metal Deposition (PMD®), an advanced plasma-based directed-energy deposition (DED) additive manufacturing (AM) process. RHP-Technology GmbH (Austria), an I-FAST partner, has played a key role in demonstrating the viability of PMD for complex structures in the past, particularly in space applications. Building on this expertise, RHP has now explored the potential of PMD for manufacturing vacuum chambers, a critical component in industries such as accelerator science, semiconductor manufacturing, and thin film deposition. PMD is an additive manufacturing technique that uses plasma as an energy source to deposit metal materials layer by layer. This method supports the use of powder, wire, or a combination of both as feedstock for creating large, near-net-shape components with high deposition rates. The process utilizes a plasma torch (Figure 52) where materials, in this case in form of wire(s), are injected into the plasma plume for melting or sintering. Between the electrode and the copper torch, a difference of potential of 20 V is imposed; then, argon (in this case known as pilot gas) is flushed in between these two parts, causing its ionization and leading to the formation of a high-temperature plasma plume. In turn, the plasma plume forms an electrical connection between the electrode and the workpiece to initiate the main arc. An inert gas stream (shielding gas) is then applied around the arc to prevent oxidation and contamination. Meanwhile, the feedstock material (wire) is fed into the main arc, causing its melting [1]. Finally, as the feedstock material is molten, the torch (print head) moves about, leaving a trail of molten deposited metal, similar to other DED processes. The result is a 3D-printed object in near-net shape, that is, in a condition that requires minimal machining to be ready to use.

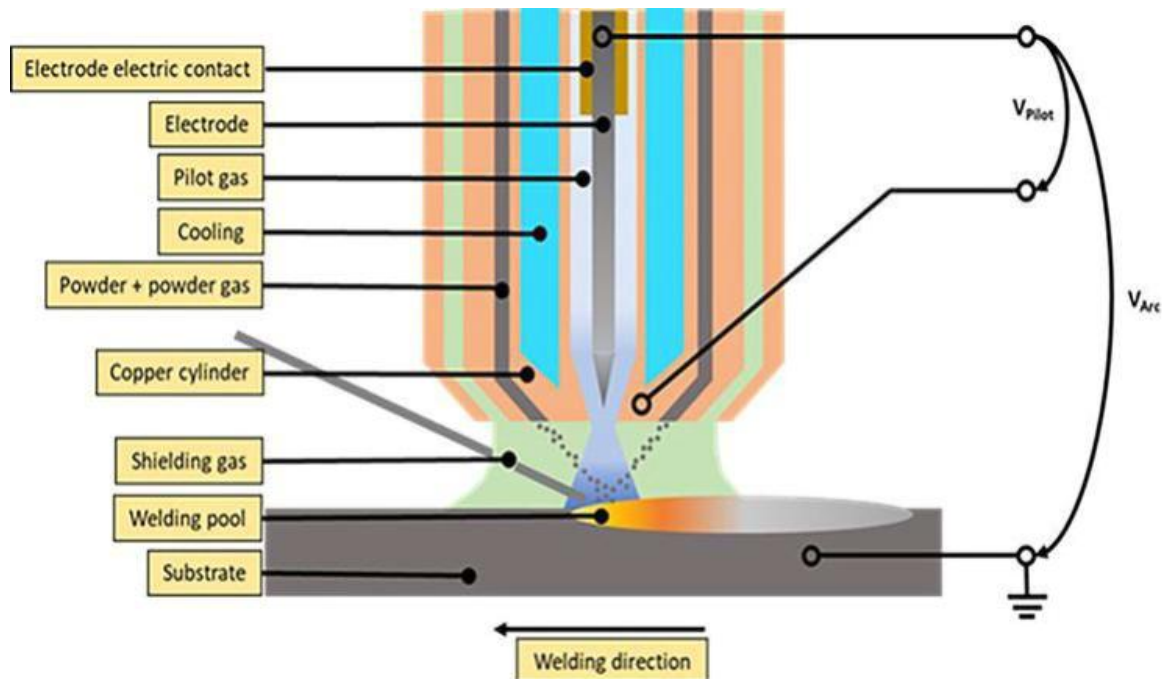


Figure 52. Overview of the plasma torch, as well as the core working principle of the Plasma Metal Deposition [1]

One of the main advantages of PMD over traditional manufacturing methods for many objects, including vacuum chambers, is its ability to produce complex geometries with significantly less material waste. Conventional methods rely on extensive machining, where large amounts of material are removed from a solid block, leading to inefficiencies, high costs, and longer production times [2,3]. Additionally, these processes often require multiple welding steps to assemble different components, increasing the risk of defects, leaks, and residual stresses in the final structure [4,5]. In contrast, PMD enables near-net-shape manufacturing, where material is added precisely where needed, minimizing waste and reducing the number of required integration steps. This not only streamlines production but also enhances the structural integrity of the chamber by eliminating many post-hoc welded joints. Another crucial advantage of PMD is its ability to make high-performance materials, such as titanium, a more viable option for vacuum chamber manufacturing. Titanium offers exceptional strength-to-weight ratio, corrosion resistance, and high-temperature stability, making it an ideal choice for demanding applications; however, its high cost and difficult machinability have traditionally made it prohibitive for large-scale use [6]. With PMD, only the necessary material is deposited, drastically reducing material waste and making titanium more cost-effective. Additionally, PMD reduces the need for extensive machining, further lowering production costs and lead times. This opens the door for wider adoption of titanium and other advanced materials in vacuum chamber manufacturing, enabling improved performance without the traditionally associated cost barriers.

To experimentally address the feasibility of PMD to manufacture vacuum chambers, RHP designed a generic demonstrator with an integrated standard ConFlat (CF) flange, without the need of welding or sourcing commercial off-the-shelf (COTS) components such as flanges. The project was split into four phases, as follows:

- Vacuum chamber design and tool path generation
- Manufacturing of vacuum chamber via PMD
- Evaluation of vacuum chamber
- Technology assessment

Ultimately, these activities were performed with the goals of:

- Reducing the material waste by at least 30%
- Minimizing integration steps by replacing welding operations with a streamlined toolpath-based process
- Lowering stock material requirements, using only wire and a building platform instead of multiple prefabricated components
- Decreasing the number of sourced and assembled parts from more than 20 to just 2
- Cutting production lead times to less than two weeks, compared to several weeks using traditional methods
- Improving cost efficiency, particularly for high-value alloys such as titanium

Vacuum chamber design and tool path generation

Vacuum chamber design

Prior to the vacuum chamber design, research was conducted on COTS vacuum chamber designs. The motivation for this was both to establish a baseline for comparison and to ensure that the eventual PMD demonstrator would be compatible with existing systems. Pre-existing designs (mostly COTS, but also custom builds) could be split into two main categories: (i) “traditional designs”, comprised of chambers with protruded flanges, which are added to the main body mostly via welding, and (ii) “free-form designs”, where flanges were pre-machined directly into the body, without the need of welding, forming a monolithic vessel. This distinction regarding design approaches can be visualized in Figure 53.

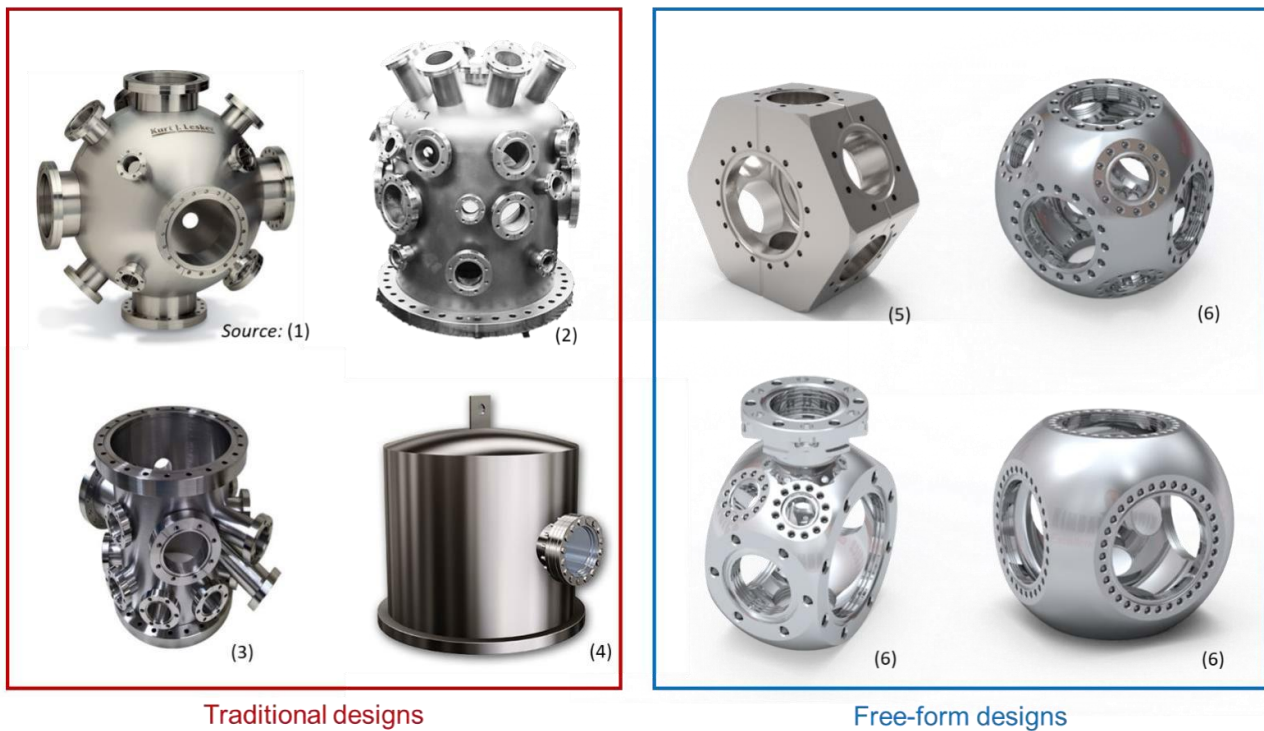


Figure 53. Design approaches for traditionally-manufactured vacuum chambers. Sources: (1) Kurt J. Lesker; (2) custom built; (3) Tigfusion; (4) Demaco; (5) Vacom; (6) Kimball Physics

Research on COTS designs revealed a trend in modern vacuum chambers toward integrated flange ports, often featuring spherical or polygonal geometries using a highly modular approach. These complex shapes are challenging to achieve through traditional sheet forming and welding, being more readily manufacturable using CNC milling instead. In these cases, the manufacturing method consists of carving the desired shape of the vessel using a solid metal block (such as a bar or a billet) as precursor material, a process normally referred to as hog-out.

On the other hand, the high material waste associated with the hog-out processing makes these designs impractical for larger dimensions, which is why such complex chambers are typically limited to just tens of millimetres in size [7]. Moreover, this issue also accounts for the limited use of high-

performance materials such as titanium, which, despite their advantageous passivating oxide layer, are often deemed impractical due to the significant material waste associated with conventional manufacturing methods. Therefore, based on this research and on characteristics of PMD as a process (and AM in general), a few design priorities were identified, as summarized by Table 3. Ultimately, the vacuum chamber demonstrator was designed as a spherical-shaped vessel, with an internal diameter of 450 mm. Ports for up to six flanges were included (two DN250CF and four DN125CF).

Design Aspect	Requirements & conditions	Decision
Shape	Must highlight the PMD capabilities in terms of complex designs and near-net shape geometries. Ideally, if not by AM, the geometry should be only accomplishable via milling from a solid block.	Spherical
Size	Must be large enough to justify the use of PMD as an alternative to milling from a solid block. Must be processable with available machinery.	ø450 mm
Flanges	Standard ConFlat dimensions. Preferably varied sizes. Must be manufacturable via post-processing CNC milling.	DN250CF DN125CF
Other features	Wall thickness (around 10-12 mm) is normally large enough to dispense the use of internal reinforcement (e.g., ribs).	None
Material	Ideally a high performance but expensive material that could not be processed via traditional manufacturing due to economical constraints.	Ti-6Al-4V

Table 3. Overview of design approach for PMD vacuum chamber demonstrator

Ti-6Al-4V (also known as Ti Gr.5 [6]) was selected as the material of choice, despite its limited use in vacuum technologies due to its inherent high cost; however, its competitiveness with other materials becomes evident when it is processed using additive manufacturing techniques (such as PMD), which significantly reduce material waste and enable more efficient production. In such a scenario, Ti-6Al-4V (and other titanium alloys for that matter) can offer potential benefits, such as a potential reduction in outgassing rate in comparison to more common materials such as stainless steel, as well as an improved corrosion performance due to the passivating oxide layer naturally forming on the surface of the process material [8]. With these considerations in mind, the demonstrator was drawn in three stages: “as-printed”, “sub-scale” (w/ upper DN250CF machined) and “full-scale” (all flanges machined), see Figure 54. RHP was the leader of this task, responsible for proposing designs and creating 3D-models; SBI provided support through general consulting, offering expertise in machine capabilities and process optimization by proposing modifications to enhance the processability of the demonstrator on their equipment, including dimensional adjustments, geometrical considerations, and other refinements.

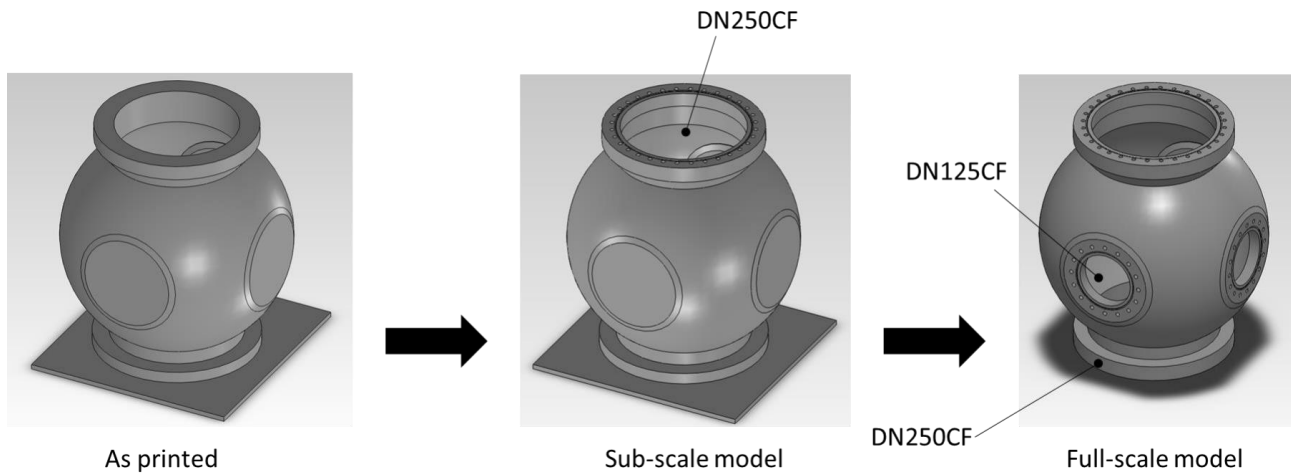


Figure 54. Implemented vacuum chamber design

Another critical aspect was the wall thickness, which, in this case, was not a direct design choice but rather an inherent characteristic of the PMD process. The 3D-printed seams produced by PMD typically range between 8 and 12 mm, depending on the material. For titanium alloys, this value is approximately 10 mm, which consequently determined the wall thickness of the designed demonstrator. However, intended lateral flange ports were specifically designed to accommodate standard CF flanges, which require a greater thickness than the 10 mm resulting from standard PMD. For instance, flanges conforming to the DN125CF standard have a thickness of 21.336 mm (0.84 in), nearly twice the expected wall thickness, necessitating additional considerations in the design process. Ultimately, the finalized design featured a wall thickness of 10 mm for the main chamber body, while the flange ports were reinforced to 24 mm to ensure compatibility with standard CF flanges. A schematic cross-section of the chamber in the “as-printed” condition, with relevant dimensions, is presented in Figure 55.

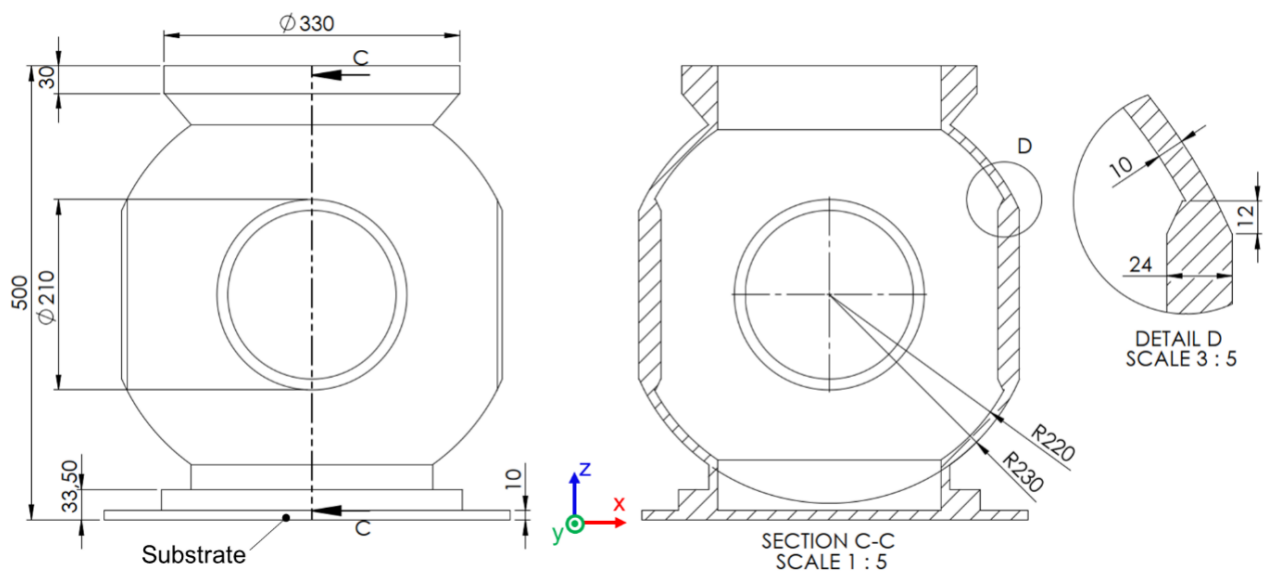


Figure 55. Schematics of the vacuum chamber in the as-printed condition. Z denotes the build direction

Tool path generation

In the present context, tool path refers to the programmed trajectory that the print head (i.e. plasma torch plus fed wire) follows during material deposition or removal. For PMD (and AM in general), the tool path dictates how the material is progressively deposited layer by layer, influencing the final geometry, surface quality, and structural integrity of the part. The tool path for most AM machines (including the one used in this project) is defined using G-code, a programming language specifically designed for computer numerical control (CNC) and additive manufacturing applications. The language consists of a series of numerical and textual commands that instruct the machine on how to move, position, and as such, control parameters such as speed, direction, layer height, and extrusion rates. Finally, G-code commands dictate the deposition path, ensuring that material is added layer by layer according to the designed geometry. Therefore, by manipulating the tool path, one can achieve different deposition patterns, which was important for this project. As mentioned previously, flange ports needed to be designed with a certain thickness that was not achievable by a single printed seam (single-seam pattern); to address this issue, an oscillatory movement was implemented into the tool path (oscillation pattern). A visual representation of both deposition patterns can be seen in Figure 56(a). However, since printing the entire chamber with oscillation would lead to an enormous material and energy expenditure (as well as much increased weight), the tool path must be programmed in such a way that only flange ports would be produced by oscillation, while the flangeless wall would be produced by single-seam. This led to the presence of transition points, see Figure 56(b). Since there were four flange ports on the demonstrator model, there were eight transition points per deposited layer.

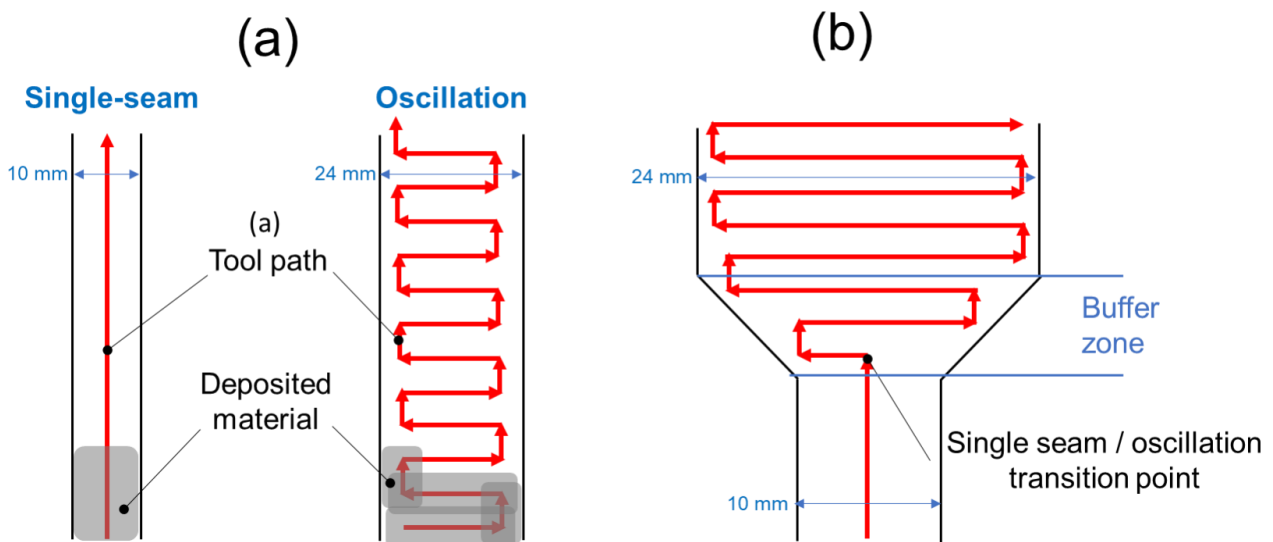


Figure 56. (a) Visual representation of single-seam and oscillation deposition patterns; (b) transition between both patterns

Transition points are of enormous importance for the process, since they dictate a change of thermal profile within the print, demanding therefore precise parameter adjustments. This will be addressed in better detail in later Sections of this report. Concerning tool path, coupling both single-seam and oscillation patterns into the same model can come with its own computational challenges, being therefore not trivially done automatically by software solutions. These solutions, popularly called

slicers, are vastly used to convert CAD models into G-code instructions; for 3-axis system, many are distributed free of charge, while for 5-axis, commercial solutions are normally required. While the consortium had such a solution available for use, it was not capable of programming a tool path with the specific requirements mentioned in the previous paragraphs. Therefore, a custom slicer was developed using Microsoft Excel. This solution was specifically tailored to the proposed design geometry and requirements, making it a one-size approach with limited applicability to other geometries. By utilizing a decision tree based mostly on trigonometric functions, the custom slicer generated the tool path point by point, automatically identifying transition points where the print head switched between single-seam and oscillation modes. An example of such a transition is illustrated in Figure 57. A flow chart with the decision tree used for the tool path generation is available on the original report. For each layer, a complete tool path was calculated, with some examples being presented on Figure 58. Each slice was 1 mm thick, meaning that the entire vessel consisted of 500 individual slices bundled together to form an entire sequence with more than 300,000 command lines. However, given the model's predominantly radial symmetry and to ensure a continuous process, the Z coordinate was incremented gradually after each command rather than only at the end of each layer. This approach eliminated process stoppages that would otherwise be required for the machine to lift the print head before proceeding to the next layer. This strategy, commonly referred to as spiral mode, is a feature that is challenging to implement in conventional slicer software.

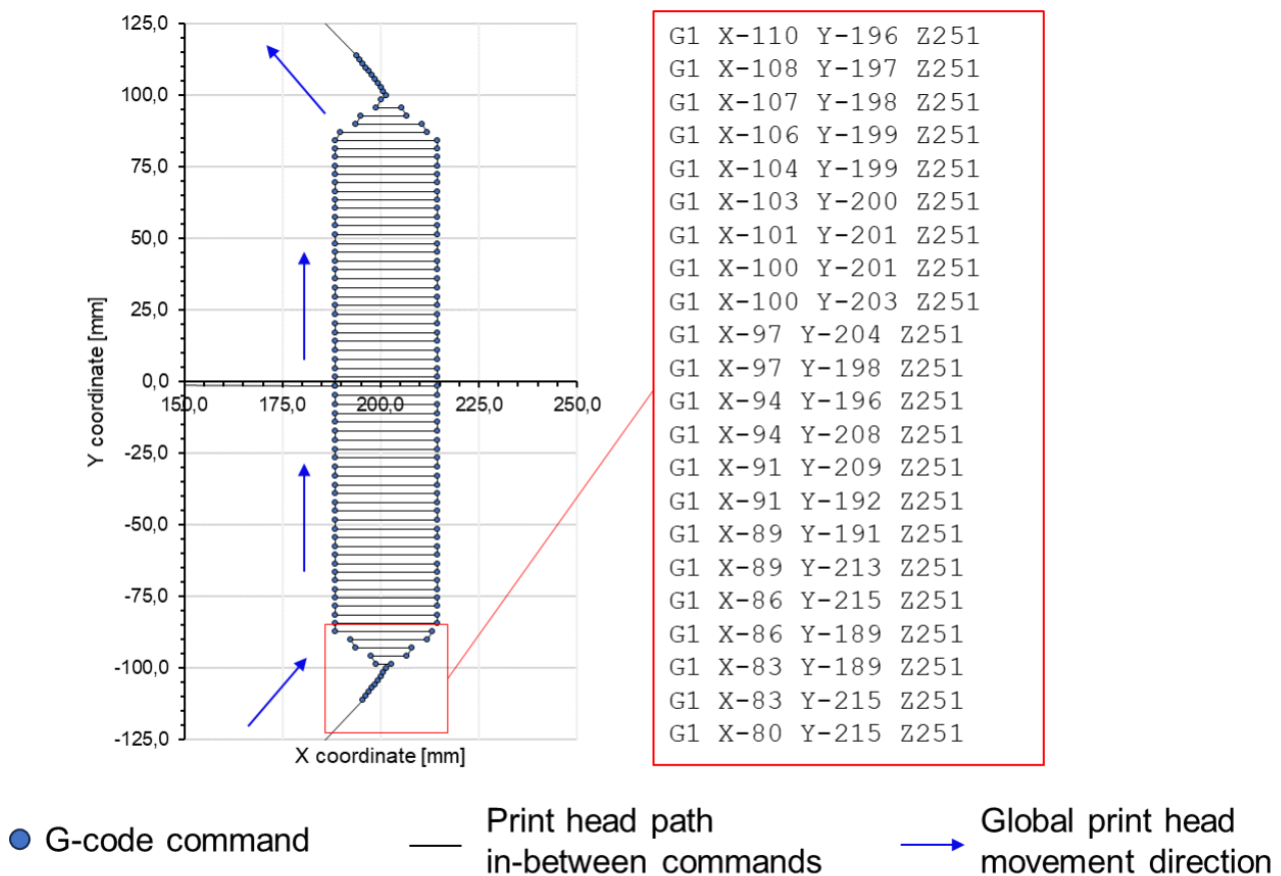


Figure 57. Example of tool path visualized using MS Excel. G-code commands on the transition between single-seam and oscillation are highlighted

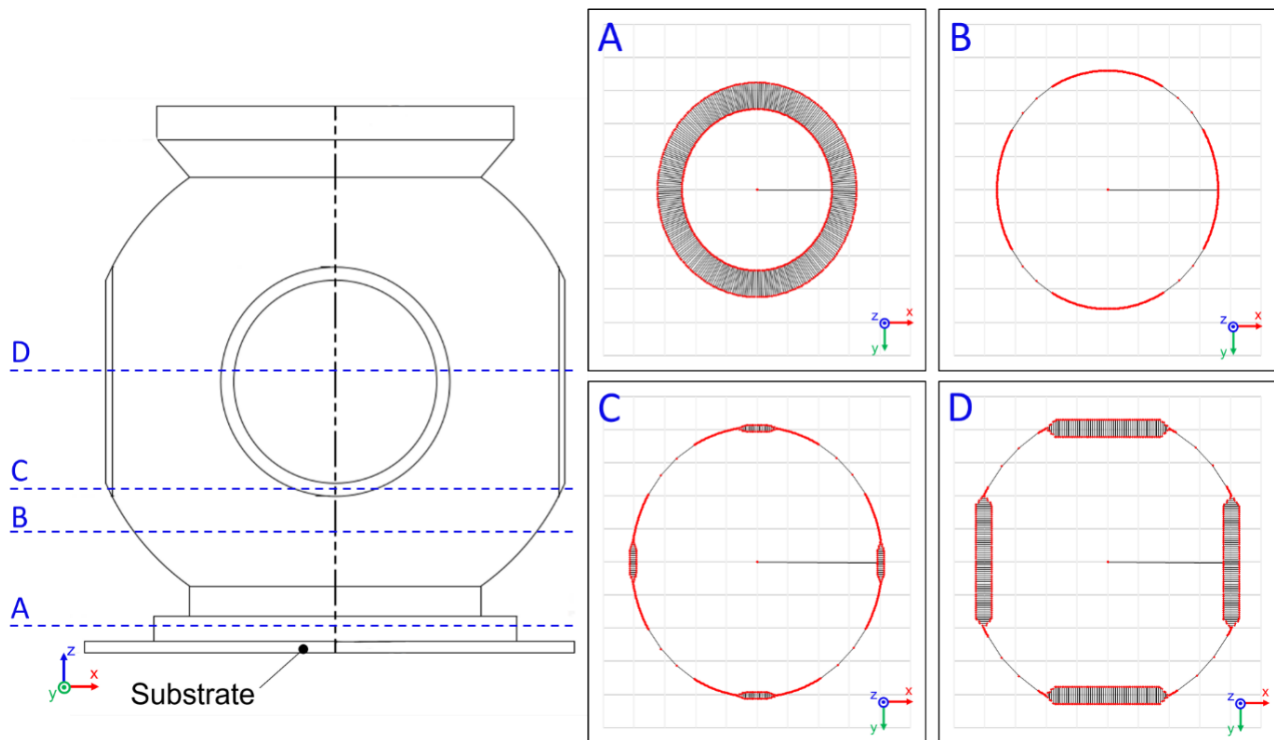


Figure 58. Overview of tool path used at different heights of the demonstrator model

Finally, to optimize the use of the turntable available on the printing machine, Cartesian coordinates X and Y were converted into polar coordinates R and θ (represented in G-code as Y and A, respectively). This ensured that the print head remained stationary in the X direction, with only Y controlling the radial position (R) and the turntable adjusting the angular position (θ). This approach is generally recommended, as minimizing unnecessary movement reduces machine shaking and jerking, ultimately contributing to process stability.

Manufacturing of vacuum chamber

Selection of process parameters

For PMD (and most AM techniques in general), the use of either single-seam or oscillation patterns has directly consequences concerning thermal profiles and gradients acting upon the printed model. For one, single-seam patterns, with their higher global print head speed, result in shorter exposure times per unit length, leading to a relatively cooler deposition. Conversely, oscillation patterns involve slower global movement while the print head oscillates back and forth, prolonging heat exposure in localized regions and resulting in a hotter deposition. Consequently, to maintain a stable printing process, parameter adjustments are required. In single-seam regions, a higher plasma current is required to compensate for the reduced heat input and prevent lack of fusion. Additionally, the increased print head speed in these areas necessitates a higher wire feeding rate to ensure sufficient material deposition. Conversely, oscillation regions demand a lower plasma current to mitigate excessive heat buildup, as the prolonged exposure naturally leads to higher temperatures. Moreover,

the significant melt pool overlaps inherent to oscillation patterns create a tendency for material accumulation, which must be counterbalanced by reducing the wire feeding rate. For this project, the demonstrator model incorporated both single-seam and oscillation patterns, with a gradual transition between the two. As previously mentioned, these transition points are critical, particularly due to the mentioned differences in thermal behaviour and process parameters. Effectively managing the shift between single-seam and oscillation was the most challenging aspect of the demonstrator manufacturing process. This challenge was compounded by the fact that, despite extensive experience with 3D printing large parts using various materials, the specific expertise required for this particular transition was not initially available within the consortium and had to be developed throughout the project. This in and of itself constituted an innovative aspect of the project. Considering these requirements, ramps for two key parameters (namely plasma current, wire feeding rate) were defined, as shown in Figure 59. During the oscillation pattern, the plasma current and wire feeding rate were set to 135 A and 15 mm/s, respectively. As the oscillation neared the transition back to single-seam, the wire feeding rate was reduced to 5 mm/s at the start of the buffer zone (see Figure 56(b)). This adjustment was made to prevent excessive material buildup in the buffer zone, which could result in bumps that would need to be corrected the next time the print head passed through. At the center of the buffer zone, the current was reduced to 110 A, as prolonged oscillation deposition caused significant heat buildup. Lowering the current before transitioning to single-seam helped cool the deposition and minimized excess heat for the next pattern. At the exact oscillation-to-single-seam transition point, the current and wire feeding rate were immediately increased to 170 A and 30 mm/s, respectively, and maintained at these values until the next transition point (single-seam to oscillation), where the cycle resumed.

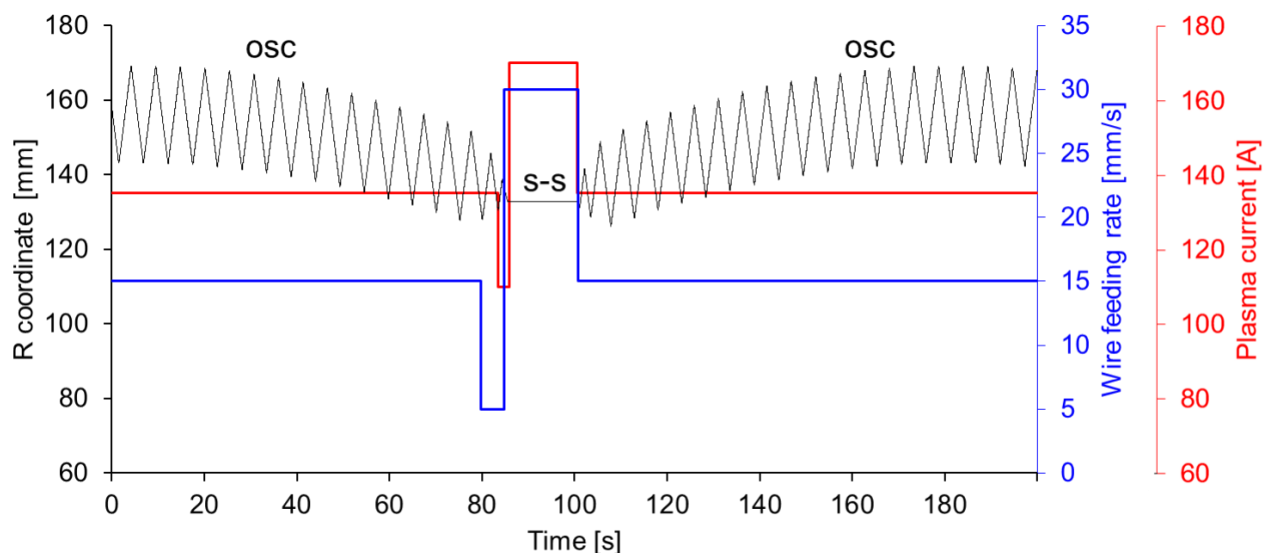


Figure 59. Evolution of plasma current and wire feeding rate at transition zones between oscillation and single-seam patterns. On the R coordinate plot, “osc” denotes oscillation and “s-s”, single-seam pattern

As previously discussed, the higher current and wire feeding rate required for single-seam deposition can be seen both as a necessity and an opportunity, given the higher deposition speed in these regions.

Since the system operates in polar coordinates, the deposition speed is directly proportional to the angular velocity of the turntable, as illustrated in Figure 60.

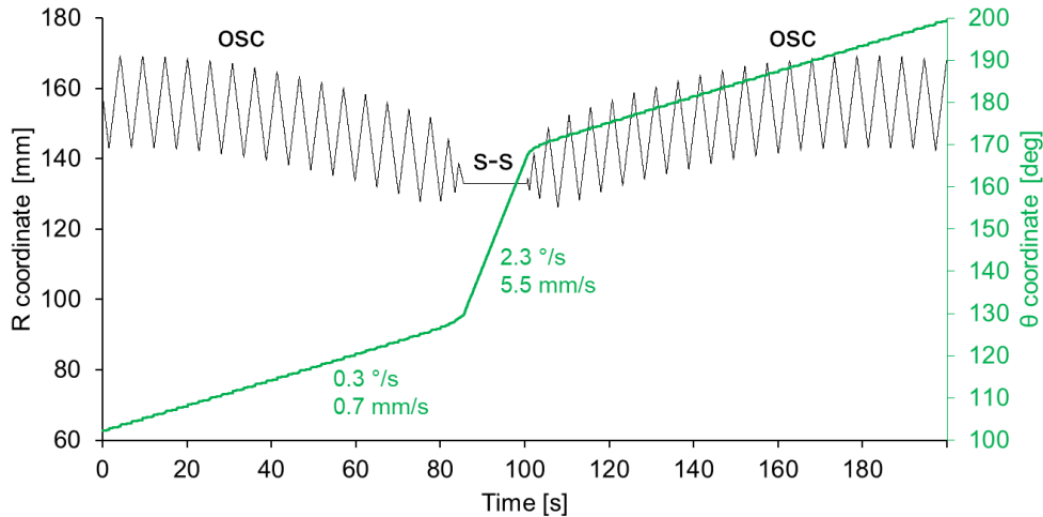


Figure 60. Evolution of polar coordinates for different deposition parameters. Linear velocity (in mm/min) calculated considering a radius of 132 mm

For the single-seam deposition pattern, an angular velocity of 2.3 °/s was implemented, which, at a radius of 132 mm (as the Figure example), corresponds to a linear deposition speed of 5.5 mm/s. In contrast, the oscillation pattern used for the lateral flanges was nearly eight times slower, at 0.3 deg/s (0.7 mm/s for $r = 132$ mm). This significant difference justified the selective use of the oscillation pattern only at the flange ports, where increased wall thickness was required.

The remainder (i.e. non-essential) process parameters were kept mostly constant throughout the print job, with their respective values being summarized in Table 4.

Parameter	Description	Value
Voltage	Potential between electrode and part	<i>osc</i> : 17 V <i>s-s</i> : 20 V
Plasma gas flow	Gas used to generate plasma	1.5 l/min
Protection gas flow	Gas used to protect the melt pool	3.0 l/min
Oxygen concentration	Value set	26 ppm
Wire feeder units	Number of wire feeders working simultaneously	<i>Lower/upper flange</i> : 02 <i>Main chamber body</i> : 01
Wire diameter	Set-up parameter	1.6 mm
Substrate material	Set-up parameter	Ti-6Al-4V
Substrate thickness	Set-up parameter	10 mm

Table 4. Set of non-essential parameters used during the manufacturing of the vacuum chamber demonstrator

Set-up and machinery

The AM activities via PMD were performed using an M3DP metal-DED 3D-printed machine, produced by SBI GmbH (Austria). This is a 5-axis, Gantry-system based machine with an enclosed chamber. At the available configuration, it was capable of a build volume of 600 x 600 x 600 mm, with minimum layer height and width of 0.7 mm and 3.0 mm, respectively. Feedstock wire was loaded as spools, with dual extrusion being possible and in fact used during certain sections of the vacuum chamber (more details in the following sections). To mitigate oxidation on the printed chamber, during the process the chamber was flooded with argon (Ar) until an oxygen concentration of 80 ppm was reached, being then kept throughout the process. An exemplary unit of the machine is shown in Figure 61.



Figure 61. M3DP machine, manufactured by SBI GmbH and used for additive manufacturing activities covered by the HVac project at RHP.

Manufacturing of chamber via PLASMA METAL DEPOSITION (PMD)

The 3D-printing of the vacuum chamber demonstrator was split into three main sections: the lower flange, the main chamber body and the upper flange. Specificities concerning the manufacturing effort are reported in the upcoming subsections.

Lower flange

Designed as a near-net shape model of a standard DN250CF flange, this section was considered the most straightforward to manufacture among the three, as it featured a fully radially symmetric oscillation ring, seamlessly transitioning into a single-seam cylinder on top. Pictures of the lower flange section during its processing are shown in Figure 53. Early in the production of this section, to achieve faster deposition rates, the high stability of the process allowed for on -the-fly parameter adjustments. The wire feeding rate was increased from 15 mm/s to 50 mm/s, utilizing both wire

feeders simultaneously. Additionally, the process was running colder than expected — an occurrence often observed in the initial layers due to increased conductive heat losses from the larger contact surface with the surroundings. To compensate, the current was raised to 190 A until the single-seam cylinder portions, where it was subsequently reduced back to 170 A. This section was completed in 7 hours of (net) printing time.

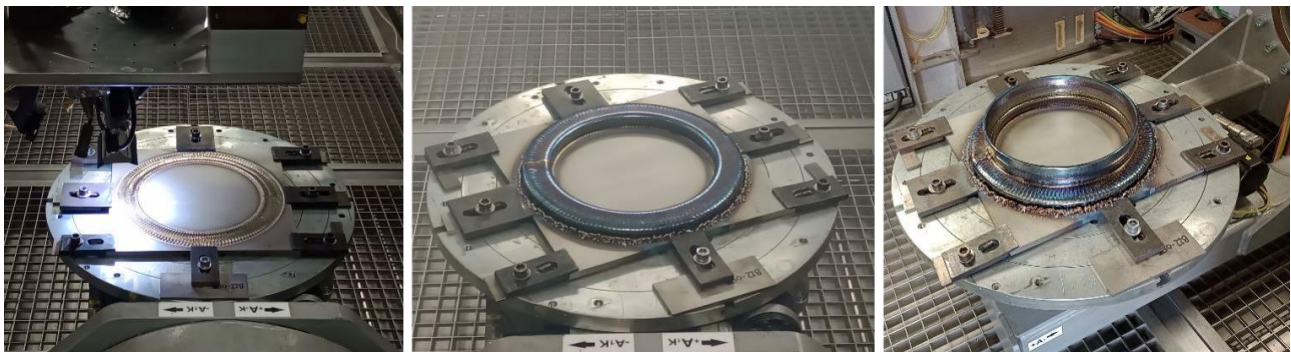


Figure 62. Pictures of the PMD process during the manufacturing of the lower flange section. From left to right: printing of first layer; finished lower flange; finished section, with flange and cylinder.

Chamber body and lateral flanges

In contrast, the chamber body was the most difficult section to manufacture, due to the reasons described earlier. It consisted of three sub-sections, namely: lower bowl, main ring and upper bowl. As the name suggests, the lower and upper bowls served as the caps for the printed vacuum chamber body, which consisted solely of single-seam depositions. These were the only areas where the tilt table feature of the printing machine needed to be utilized, as the steep angles inherent to the spherical geometry would have otherwise made the print impossible. Despite not exhibiting any single-seam/oscillation transitions, these regions could be effectively printed with the process parameters originally planned for single-seam depositions. On the other hand, the main ring was the core of the chamber and the only region where the single -seam/oscillation transition issue was present. However, despite the anticipated challenges, the constant tool path transitions and parameter adjustments were successfully managed without major setbacks, though some defects were present. Figure 63 illustrates some important stages of the chamber body manufacturing. Overall, this section took 37 hours of net printing time to be completed.

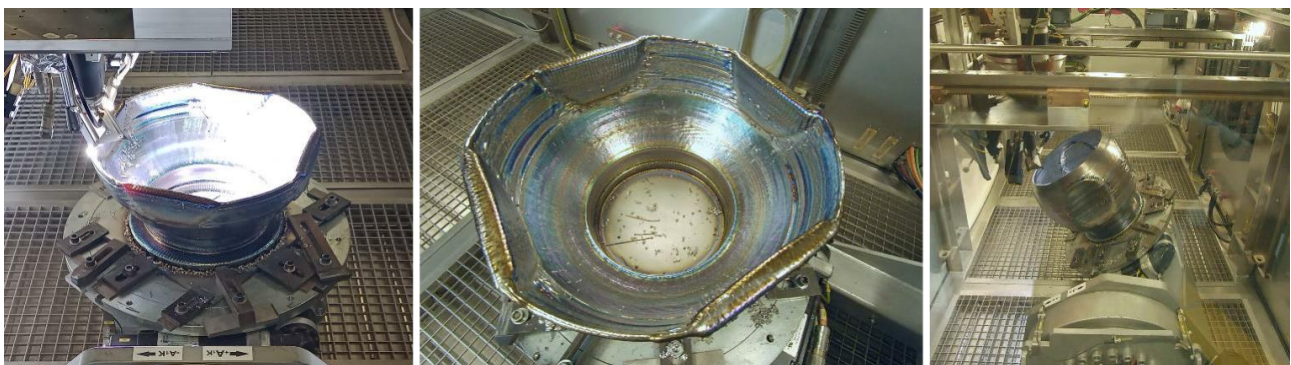


Figure 63. Pictures of the PMD process during the manufacturing of the chamber body section. From left to right: printing of a lateral flange; chamber at 50% completion stage; printing of upper bowl using tilt table

Upper flange

The upper flange section was the final part to be produced and was originally intended to mirror the lower flange made earlier. Since it is located at the upper side of the chamber, with no substrate support, it was initially planned that this section would be printed with the assistance of the tilting table. However, it was not anticipated that, while the partially-printed chamber fit well within the machine's dimensional envelope when sitting upright on the build platform, it in fact exceeded this envelope when tilted sideways, making the use of the tilt table in this case impossible. The alternative was to forgo the transition cylinder, similar to the one printed in the lower flange section, in favour of a ramp-like shape. This is illustrated in Figure 64, along with other representative images of the process. This ramp was printed using an oscillation pattern, with a gradually increasing amplitude, which grew until it matched the amplitude originally planned for the upper flange.



Figure 64. Pictures of the PMD process during the manufacturing of the upper flange section. From left to right: beginning of the upper flange section being printed; final upper flange section, showing the ramp-like shape used to support the upper flange; final look of the entire chamber in the as-printed condition

While this issue could also be considered a setback, it did not impact the progress in any substantial way. This section took slightly less than 7 hours of net printing time to be completed. In total, the demonstrator was completed in 54 hours.

Post processing steps

Following the manufacturing via PMD, the upper flange was processed via subtractive manufacturing (CNC milling), through which it was possible to produce an exact rendition of a standard DN250CF flange, to be later used for the vacuum tests (see Figure 65). This operation marked the transition from “as-printed” to “sub-scale model” stages.



Figure 65. Vacuum chamber demonstrator before (left) and after (right) post-processing milling operation. Flange size correspond to standard DN250CF.

The transition from the “sub-scale model” to the “full-scale model” (as described earlier in Figure 51) would involve the machining of all the remaining flanges (one lower DN250CF and four lateral DN125CF ones). This was planned to be completed following the vacuum testing, as a means to rule out additional sources of potential leakage. However, due to delays concerning the vacuum testing, the complete “full-scale model” could not be produced within the timeframe of the present project.

Manufacturing of adaptors for vacuum test

Since the only outlet of the chamber was a the upper DN250CF flange, it was necessary to machine custom flange adaptors to enable proper vacuum system integration for tests later. The DN250CF size was too large for any available vacuum pump, requiring a reduction to more common flange sizes such as DN160CF and DN100CF. Additionally, adaptors were needed to accommodate vacuum gauges, valves, and other instrumentation essential for process monitoring and control. These demanded even smaller flange sizes, such as DN16CF and DN25CF. In this case, the adaptors were based on modified COTS components, such as blind flanges, nipples, and zero-length adaptors. The modifications involved an initial machining step to produce mounting ports for nipples and half-nipples, followed by welding using plasma. As explained later, two vacuum tests in two different facilities were conducted; for each, an individual adaptor was produced. For Vacuum Test 01 (performed in-house), a DN250 blind flange was drilled with ports for a KF160 full nipple and a KF16 half nipple. These two were then mounted on the machined flange and welded (Figure 66). Likewise, for Vacuum Test 02, done at an external service provider, the adaptor consisted of a DN250CF-to-DN100CF zero-length adaptor, with a port for a DN25CF half nipple next to the center hole.



Figure 66. Adaptor used for Vacuum Test 01, performed in-house. Left: blind flanged machined with full and half nipples positioned accordingly. Right: final adaptor after welding

Evaluation of vacuum chamber

Visual inspection

The visual inspection involved checking for defects resulting from the PMD process, as well as an initial assessment of whether the designed features were accurately reproduced, particularly in terms of geometry, prior to 3D-scanning. Regarding surface quality, the vacuum chamber demonstrator exhibited no unexpected features beyond those anticipated in advance. This means that it possessed a characteristic colorful surface (Figure 67) that is significantly common in titanium alloys processed by additive manufacturing. This is a result of oxidation, which tends to occur, readily, albeit at limited capacity, even with concentrations as low as 80 ppm, since titanium is known for its strong affinity for oxygen; in fact, this is the main reason why it is commonly used as getter material, once its oxide layer is removed [9]. However, this very oxide layer is also known for its superior corrosion resistance properties, making it beneficial for certain applications [6], even vacuum-related [8]. Furthermore, it has been suggested that this layer acts as a barrier to bulk gases like hydrogen, preventing their diffusion from the vessel walls into the chamber, which ultimately decreases its outgassing rate [8].



Figure 67. Overview of the vacuum chamber in the as-printed condition

Overall, the demonstrator was in good condition, with no critical defects that would compromise functionality. However, some deposition inconsistencies and solidified droplets were observed around the lateral flange ports, as shown in Figure 68. These areas correspond to the transitions between oscillation and single-seam patterns, which were expected to present some challenges during processing, as explained previously. Additionally, the bottom of the flange ports was also affected by the pattern transition, as the oscillation had to begin over a much thinner single-seam layer. This resulted in partially unsupported material, causing some droplets to roll down due to gravity. However, over time, these very droplets acted as a makeshift support, allowing the oscillation amplitude to expand.

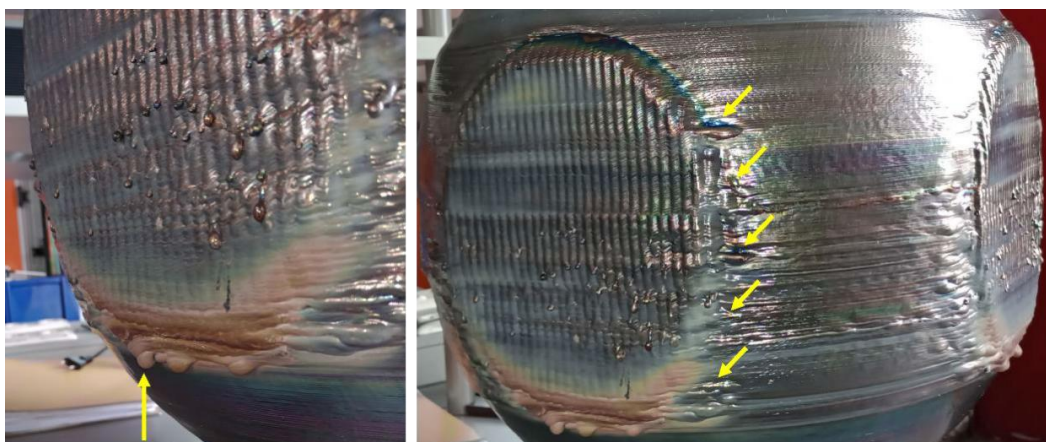


Figure 68. Main inaccuracies observed on lateral flange ports upon visual inspection. Left: arrow indicates presence of solidified droplets, characteristic of a melt pool rolling down due to gravity; right: arrows indicate deposition inconsistencies at the oscillation/single-seam transition.

While these deposition inconsistencies could pose a structural weakness and a potential leakage point during vacuum testing, this type of detrimental impact was not observed, as reported in the upcoming sections. Additionally, occasional droplets were observed in the middle of the flange port, but their significance is minimal, as these areas are intended to be machined away in the final full-scale model. Another area exhibiting deposition inconsistencies, albeit with minimal practical impact, was the interior of the upper flange. These defects manifested as alternating regions of material accumulation and deficiency, resulting in a rough surface. However, much like the droplets in the middle of the lateral flange ports, these irregularities were largely eliminated during milling in the production of the upper flange.



Figure 69. Left: material deposition inconsistencies indicated at the interior portions of the upper flange; right: closer look at the defects

3D-Scanning

The 3D-scanning of the vacuum chamber demonstrator was performed using an absolute arm laser 3D-scanner, with results shown in Figure 70. Material accumulation and deficiency deviations were quantified by comparing the fabricated sub-scale model to its pre-designed CAD file (Figure 53). An overall trend was observed where the lower hemisphere of the chamber had excess material, while the upper hemisphere exhibited a deficiency. The reasons for this phenomenon in this specific case are not fully understood, but it could be reasonably attributed to the effects of gravity and material flow during the PMD process. As the material is deposited, gravity may have caused molten material to gradually settle more heavily in the lower hemisphere of the chamber, layer after layer. Moreover, it could be argued that the hotter the region, the longer the metal remained liquid, with a less viscous melt pool, enabling more material to flow downward and solidify below its intended area. In this scenario, a direct correlation might exist between material shortage and process temperature: the upper regions tend to be hotter due to their reduced contact area for heat dissipation, whereas the lower areas cool faster, encouraging the material to solidify closer to its original molten state. Nevertheless, further investigation into the material flow dynamics and deposition parameters would be needed to confirm either hypothesis.

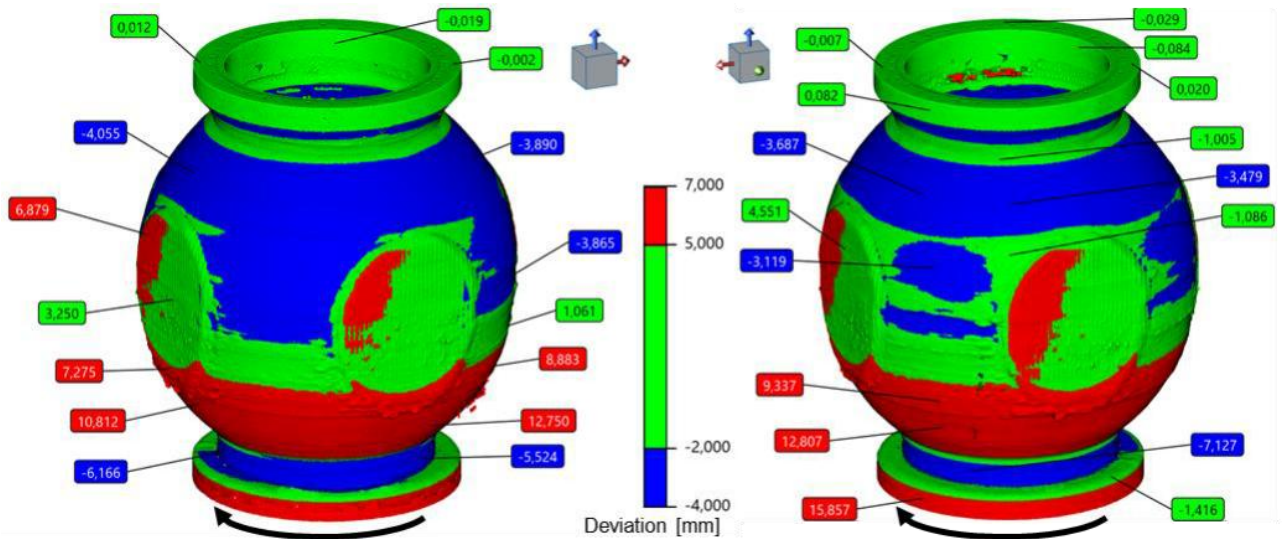


Figure 70. Representative images of 3D-scan of vacuum chamber demonstrator (sub-scale model) at different view angles: Arrows at the bottom of the images denote the rotational direction of the turning table during the PMD process

Another area where deviations were observed is on the lateral flanges, where there was an overall excess of material. This is typically expected in this type of deposition pattern due to the overlap of material between each oscillation period, as illustrated in Figure 56(b). However, a more specific pattern was noticed, with the material excess being more prominent at the beginning of the oscillation regions. This supports the hypothesis that hotter deposition leads to a decrease in the deposited material. As mentioned earlier, oscillation patterns concentrate heat, and this effect is more pronounced when the path to be deposited via oscillation is longer. In these situations, oscillation regions tend to get progressively hotter toward the end, which suggests that similar to the upper/lower hemisphere phenomenon, material at the end of the oscillation was hotter and therefore more likely to flow downward, resulting in a lack of material in comparison to the beginning of the oscillation areas.

Vacuum tests

In order to reduce risks in terms of equipment damage, vacuum tests were performed on the demonstrator (sub-scale model) in two steps. The first test was carried out using rough vacuum pump together with a turbomolecular pump to identify major leakage spots in both the chamber and the manufactured adaptor. Then, since no leakage nor major contamination sources were identified, a second test, this time on a high vacuum testing setup, was performed. This second test, performed by a subcontractor, caused a delay in the project progress, since the initial foreseen subcontractor was not able to perform the test and therefore another partner had to be identified. The first test (Vacuum Test 01) was performed in-house with equipment (pumps, sensors) that were able of reaching pressure levels down to 10^{-6} mbar. This test enabled a valuable first assessment of mechanical integrity of the chamber, possible leakage spots (either on the chamber itself or on the welded adaptors), as well as the calculation of leakage rate. Subsequently, a second and high-level test (Vacuum Test 02) was performed by a subcontractor (FOTEC Forschungs- und Technologietransfer GmbH, Austria), with equipment capable of reaching lower pressures levels than the in-house setup. In this case a vacuum

level of down to the 10^{-8} mbar level was performed. The results of both tests will be presented in greater detail in the following subsections.

Test 01 (in-house)

Fig. 71 shows the setup used for Vacuum Test 01, which was carried out at RHP-Technology. The setup consisted of a mechanical pump—powerful enough to reach a 10^{-4} mbar pressure connected to a turbomolecular pump (10^{-6} mbar) through a shut-off valve. The latter pump was connected to the demonstrator via the KF160 port installed on the manufactured adaptor. Likewise, a vacuum gauge was connected to the KF16 nipple right next to it. The mechanical pump act as roughening pump and was shut off when pressure reached 3×10^{-3} mbar. At this point, the turbomolecular pump was turned on.



Figure 71. Overview of setup used for Vacuum Test 01. (1) Mechanical (roughening) pump; (2) shut-off valve; (3) turbomolecular pump; (4) vacuum gauge; (5) demonstrator

With this setup, the vacuum level reached a value of 1.6×10^{-6} mbar after 108 hours of consecutive pumping. Since the system was purely analogical, no proper pumping curve was registered; however, a couple of readings at irregular intervals were performed manually on the vacuum gauge, which enabled to provide a rough estimation of the pressure level evolution over the course of the test campaign (see left panel, Figure 72). Based on this information, it is possible to estimate that the system reached a pressure plateau before 60 hours of pumping, with the subsequent 48 hours not yielding significant improvement on the pressure levels. To estimate the leakage rate, the internal pressure was registered at regular intervals after the pumping process, once both pumps were turned

off (see right panel, Figure 4-6). Based on this data, the leakage rate of the system was determined to be approximately $2.9 \times 10^{-6} \text{ Pa.m}^3/\text{s}$. Concerning the structural integrity of the chamber, no distortions were detected upon visual inspection following Vacuum Test 01.

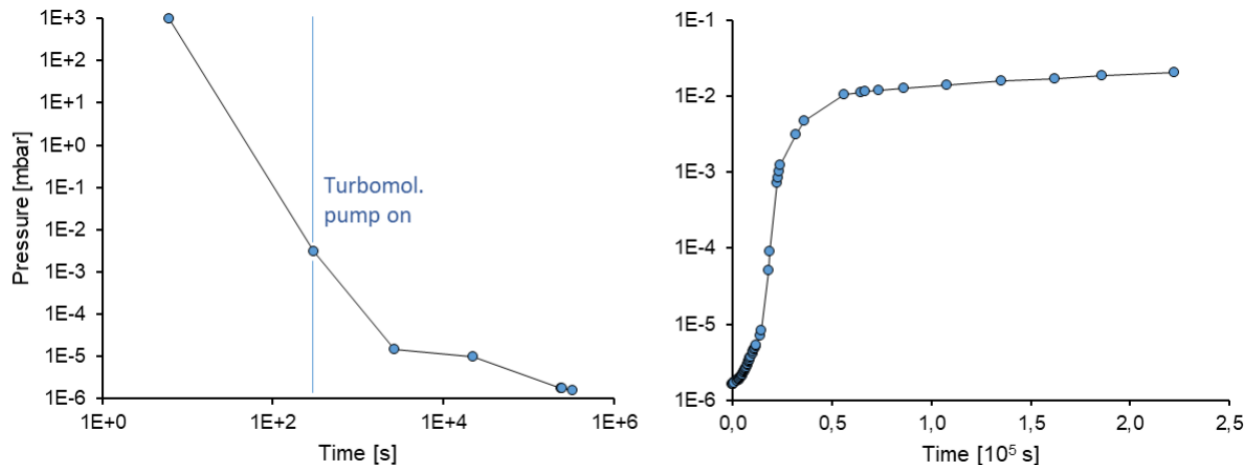


Figure 72. Pressure levels registered at different time intervals during Vacuum Test 01. Left: pressure during pumping; Right: pressure after pumping stopped. Blue dots denote individual measurement points

Test 02 (external)

As previously mentioned, Vacuum Test 02 was conducted at a subcontractor. The decision to seek an external service provider was driven by two main factors: (i) the first vacuum test suggested that the demonstrator not only was leak-tight, but it also could achieve a lower vacuum level with an improved setup, and (ii) the consortium lacked the capability to assemble such a setup independently. Due to the unavailability of the initial foreseen subcontractor, finding a suitable partner for these tests took significantly longer than anticipated, delaying the process considerably, especially considering also that new adaptors had to be procured and modified accordingly (as mentioned earlier). The setup implemented at the subcontractor consisted of single turbomolecular pump, capable of reaching pressures lower than 10^{-8} mbar , mounted directed on the DN100CF end of the zero-length adaptor. On a separate port (on the same adaptor), a vacuum gauge was mounted on the DN25CF half nipple. Around the chamber, with the goal of promoting a gentle degassing (or conditioning), 750-W electric heater straps were wrapped around the demonstrator, which enable the outer walls to reach a temperature of 58°C . The setup can be visualized in Figure 73. With this setup, the demonstrator chamber was capable of housing a pressure of $7.0 \times 10^{-8} \text{ mbar}$ after 163 hours of continuous pumping, with intermittent use of the electrical heaters. The evolution of the pressure over pumping time can be seen in Figure 71. The heaters facilitated the release of trapped contaminants and water, as evidenced by the sharp pressure increase when they were activated. While this does not qualify as true baking—typically requiring temperatures between 100°C and 200°C —it still contributed to achieving a lower final pressure.

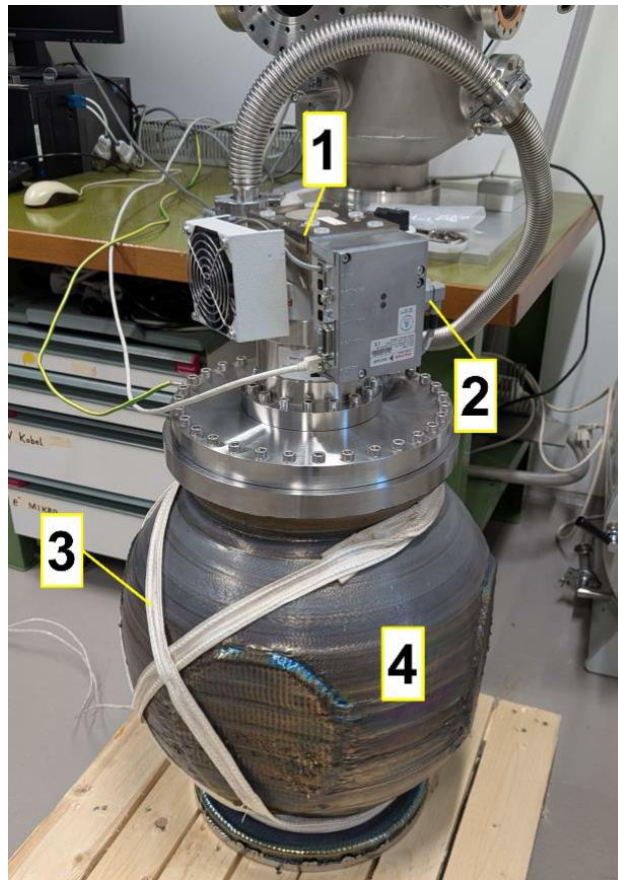


Figure 73. Overview of setup used for Vacuum Test 02. (1) Turbomolecular pump; (2) vacuum gauge; (3) tape heater; (4) Demonstrator.

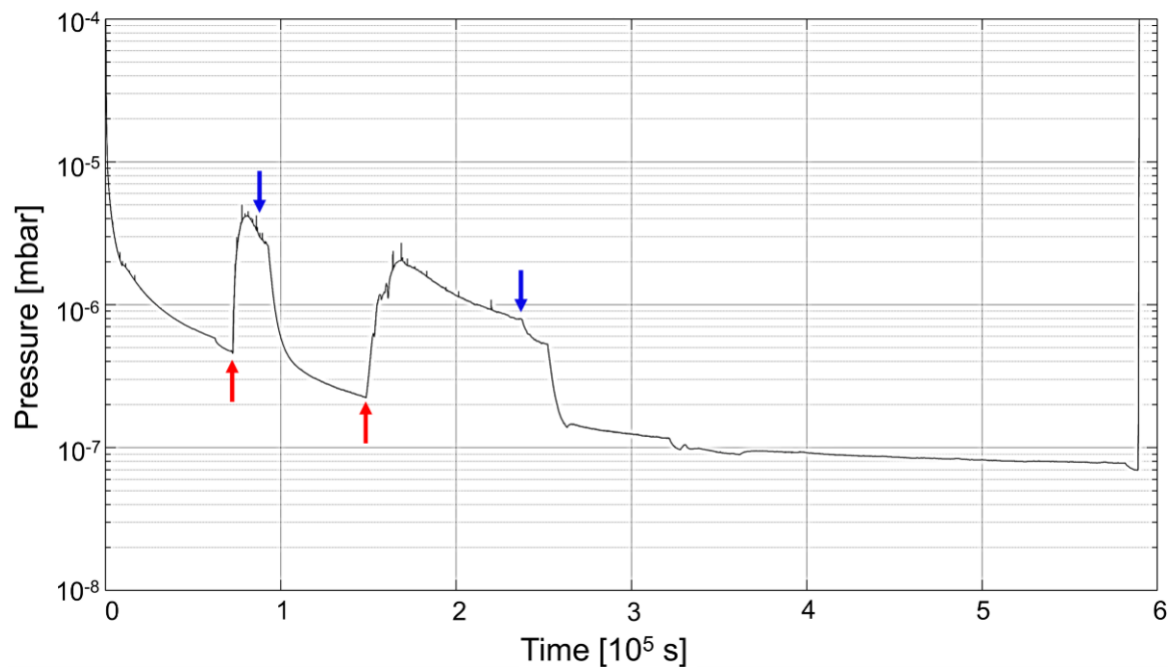


Figure 74. Pressure levels recorded throughout Vacuum Test 02. Red arrows indicate when the heater was turned on, while blue arrows mark when it was turned off.

3 Scientific publications, dissemination, and communication of work

- **HIGHEST**

- Abstracts submitted to IPAC 2025 and EUCAS 2025 conferences. Author: S. Calatroni
- Meeting at KIT 16.11.2023 <https://indico.cern.ch/event/1359573/>
- Meeting at ICMAB 31.1.2024 <https://indico.cern.ch/event/1359609/>
- Meeting at CERN 5.7.2024 <https://indico.cern.ch/event/1409300/>

- **TW RF GUN**

- Lucas, T.G. et al, Toward a brightness upgrade to the SwissFEL: A high gradient traveling-wave rf photogun. Phys. Rev. Accel. Beams 26, 103401 (2023)
- Lucas, T.G. et al, Application of A Reduced Phase Velocity High Brightness Photogun For MeV Ultrafast Electron Diffraction, Proceedings of International Particle Accelerator Conference (Nashville, USA, 2024).
- Christ, J. et al, Simulation Of Coupled Space Charge And Wakefield Effects For A Prototype Tw-Gun At Swissfel, Proceedings of International Particle Accelerator Conference (Nashville, USA, 2024).
- Lucas, T.G. et al., A Discussion of Key Concepts for the Next Generation of High Brightness Injectors. International Linear Accelerator Conference (Liverpool, UK, 2022).
- Lucas, T.G., Breaking Convention: Novel Normal-Conducting Electron Sources for Higher 6D Brightness, 41st International Free Electron Laser Conference. (Warsaw 2024)
- Lucas, T.G., Linac24 (Oral Poster by E. Prat on behalf of T.G. Lucas) (Nashville 2024)
- Lucas, T.G., Modelling and observation of intrabeam scattering in photoinjectors, First annual workshop on Longitudinal Electron beam Dynamics for coherent Sources (LEDS'23) (Rome 2023).
- Lucas, T.G., A Travelling-Wave Radio-Frequency Photogun for a Brightness Upgrade to SwissFEL at the 67th ICFA Advanced Beam Dynamics Workshop on Future Light Sources (Luzern 2023).
- Lucas, T.G., A Versatile High Brightness Travelling-Wave Radio-Frequency Photogun, Physics and Applications of High Brightness Beams, (San Sebastian 2023).
- Lucas, T.G., Craievich, P. and Reiche, S., A Discussion of Key Concepts for the Next Generation of High Brightness Injectors. Invited talk to the International Linear Accelerator Conference Liverpool, UK, 2022).

- **KAIO**

- Louis Daniault, Jaismeen Kaur, Geoffrey Gallé, Cedric Sire, François Sylla, Rodrigo Lopez-Martens, Sub-2-cycle post-compression of multi-mJ energy Ti:sapphire laser pulses in a gas-filled multi-pass cell, 11th EPS-QEOD Europhoton Conference on Solid-

State, Fibre, and Waveguide Coherent Light Sources
(<https://doi.org/10.1051/epjconf/202430704063>)

- Louis Daniault, Jaismeen Kaur, Geoffrey Gallé, Cedric Sire, François Sylla, and Rodrigo Lopez-Martens, Sub-2-cycle post-compression of multi-mJ energy Ti:sapphire laser pulses in a gas-filled multi-pass cell, Optics Letters 49, 6833-6836 (2024)

• **AMPLIFIERS**

- January 7, 2025, Anshu Singh delivered an invited lecture at the National Institute of Technology Patna, India, titled "Development of Micro Magnetron under the Marie S. Curie Fellowship Program."
- At the International Vacuum Electronics Conference (IVEC) on April 27, 2024, in Monterey, USA, Anshu Singh and Dragos Dancila, presented a poster titled "Design and Simulation of 76 GHz Spatially Harmonic Magnetron."
- During the SUNERGY 2023 conference held at Uppsala University from October 24-26, Anshu Singh, Dragos Dancila and Viplab Sanyal, presented a poster entitled "Microwave-Assisted Green Hydrogen Generation: A Key Technology for SDG-7 & 13."
- May 24, 2023, at the Swedish Microwave Days in Stockholm, Sweden, Anshu Singh and Dragos Dancila delivered a talk on "Vacuum Electron Device Technology: Key to Clean and Safe Energy Generation (SDG-7) for Climate Stabilization (SDG-13)."

• **FLA**

- 2-3/12/2024; 13th WP9 Meeting; <https://events.hifis.net/event/1875/>; Berlin (HZB)
- 12/02/2025; 14th WP9 Meeting; <https://indico.cern.ch/event/1514304/>; Zoom
- Pira - Nb3Sn on Cu thin film SRF cavities for new generation LINACS operating at 4.5 K - An oral talk at the 2024 International Workshop on Future Linear Colliders (LCWS2024), Tokyo, Japan, 8-11 July 2024

• **AMIS**

- Meeting with industrial partners involved in the project in November 2024 – @ Formnext – Frankfurt, Germany
- Periodic meetings: Individual Work Package members convened monthly – online and in-person mode

• **HVAC**

- The 3D-printed vacuum chamber demonstrator manufactured within the present project has become a signature exhibit at RHP-Technology booths during conferences and exhibitions across Europe (see Figure below). Since its production, it has been showcased at the following conferences:
 - Metal Additive Manufacturing Conference (MAMC), Vienna (AT), 2023

- Formnext, Frankfurt (DE), 2023 [SBI booth]
- V2023 – Vacuum & Plasma Conference, Dresden (DE), 2023
- Vacuum Technologies for Tomorrow (V2T), Grenoble (FR), 2024
- Plasma and Surface Engineering Conference & Exhibition, Erfurt (DE), 2024
- Big Science Business Forum, Trieste, 2024 [10]
- Industry Space Days (ESA-ESTEC), Noordwijk (NL), 2024
- Space Tech Expo, Bremen (DE), 2024
- Together with the Athena X-Ray telescope demonstrator—built by PMD as part of an ESA project and also visible in Figure below — the chamber stands as a hallmark of PMD's capabilities within the company, acting as a key marketing piece to showcase the technology potential to clients and partners.



- Despite the rapid advancements in AM, the application of DED techniques (such as the PMD itself) for producing vacuum chambers remains largely unexplored in scientific literature. Vacuum chambers are critical components in a wide range of industries, including aerospace, semiconductor manufacturing, and scientific research. However, most studies on AM for vacuum-related applications have focused on Powder Bed Fusion (PBF) techniques, rather than DED [11,12]. DED processes such as PMD offer unique advantages for fabricating large-scale metallic structures (such as e.g. vacuum chambers, but also pressure vessels, brackets, tools, etc.). The advantages include high deposition rates, material efficiency, and the ability to process a wide range of alloys. Therefore, the

HVac project represents a unique opportunity to bridge this knowledge gap by providing insights into the feasibility of manufacturing vacuum chambers and any other medium-to-large object using a DED AM technique. These insights can be listed as follows:

- Understanding the impact of deposition strategies, oscillation patterns, and process parameters on defect formation.
 - Addressing the challenges of scaling up DED for larger vacuum chambers, including thermal management, deposition path planning, and distortion control.
 - Exploring hybrid manufacturing approaches, where DED is combined with conventional machining and post-processing techniques.
 - Investigating the performance of an alternative alloy (in this case, Ti-6Al-4V) for vacuum-related applications.
- In a nutshell, the findings of the HVac project can provide a good support for future research in DED AM for vacuum applications, PMD or not. This knowledge can be applied not only to research focused on high-energy physics, but also space technology, and advanced manufacturing.

4 Future plans / Conclusion / relation to other IFAST work

HIGHEST

Conclusion

The HIGHEST project concluded all expected deliverables with success and with very promising results for future RF applications. The quality demonstrated in RF tests by the new large-size tapes is comparable to state-of-the-art commercial 12-mm wide tapes. This development allowed bringing the initial TRL3 to TRL4, as anticipated. These new large-size tapes are compatible with the development of novel RF high-gradient applications, in particular with the flat-disc test device at SLAC, and with potential new applications at lower frequencies, which require larger dimensions. In parallel, it has been demonstrated the feasibility of preparing X-band segmented structures using standard narrow 12-mm tapes. This technological demonstrator, presently under test at high-gradient and cryogenic conditions, allows bringing the technology to the maturity of TRL6. This level of maturity is adequate for initiating design of future applications, with a strong potential in terms of sustainability and energy savings. It should be underlined that this was achieved thanks to extreme focus and dedication of all partners, advancing of several years the originally expected timeline to attain TRL6, motivated by the expected goals and the extreme relevance for future sustainable projects.

PM4HEK

Conclusion

We aim to have the demonstrator assembled and tested before October. We had preliminary discussions with CANON on the feasibility to build the klystron that will fit the solenoid. No showstopper was identified even though a redesign of the magnet may still be necessary to fit additional constraints. Other klystron manufacturers interested in this development have contacted us to explore the possibility of future developments.

TW RF GUN

Using a combination of electromagnetic and PIC simulations, the geometry for the field emission cathode could be determined. This geometry was sent to VDL ETG where it was fabricated through single-point diamond turning. This completed Deliverable 1 of the project. Prior to the installation of the TW rf gun, the LLRF system of the beamline was updated to bring it inline with the SwissFEL standard. Furthermore, the RF diagnostics were incorporated into the waveguide network for accurate measurement of the RF signals (Milestone 2). Deliverable 2 of the project is close to completion with the conditioning to 17 MW mostly complete. Following this, we will install diagnostic beamline (Milestone 1) to characterise the beam quality (Deliverable 3). Finally, despite the loss of our OEM, the lead scientist was able to deliver the market research report (Milestone 3).

Delays, Issues and Proposed Updated Timeline

The development of the traveling-wave (TW) RF field emission gun has progressed greatly. However, it has faced hurdles in the progression of the project. A few significant factors have led to delays in the project that mean that some of the goals have not yet been met. The first factor that led to delays was the underestimation of the available technical support during the building of the test stand. This work occurred during a time when PSI was realising the upgrade to other large infrastructure, and this led to fewer resources to assist in the building of the beamline. Another factor that led to delays was an initial miscommunication that led to the funding being distributed incorrectly between the PSI and VDL ETG. These two factors led to delays in the expected project timeline. We aim to finish the project within the IFAST project, including the 6-month extension. With the current conditioning of the gun, the next step will be to install the beamline, whose components are all available. Finally, the characterisation of the beam will occur, and final report delivered.

Conclusion

The development of the field-emission traveling-wave (TW) RF gun has demonstrated significant progress in advancing high-brightness electron sources for accelerator applications. Through extensive simulations, precise fabrication, and rigorous testing, the project has progressed significantly towards illustrating the feasibility of using field-emission cathodes within a traveling-wave RF structure. Initial low-power and high-power conditioning tests have yielded promising results, with successful dark current generation and beam characterisation efforts underway. Despite challenges such as infrastructure delays and funding allocations, the project remains on track for completion within the extended IFAST timeline. The TW RF gun presents distinct advantages over conventional electron sources, including simplified operation, reduced power consumption, and the

elimination of costly laser systems. These benefits position it as a strong candidate for applications in radiotherapy, ultrafast electron diffraction, and industrial accelerators. Moving forward, the final phases of high-power conditioning and beam quality characterisation will solidify the gun's performance capabilities. Furthermore, continued market research and industrial collaboration will be crucial in transitioning this technology from a research prototype to a commercially viable product. With its innovative design and strong potential for real-world applications, the field-emission TW RF gun represents a significant step toward next-generation electron sources for industrial applications.

KAIO

Conclusion

Despite the low level of completion of the WPs, the technical milestones achieved during the project are highly encouraging, in particular the demonstration of MPC post-compression of an industry-grade multi-mJ kHz Ti:Sa laser at levels already competing with state-of-the-art commercial waveguide-based post-compression technology. The completion of the remaining project milestones is expected to lead to pioneering technical breakthroughs, high-impact publications and significant progress toward the development of commercially viable LPA technology (fully integrated system or individual sub-systems such as a stand-alone MPC).

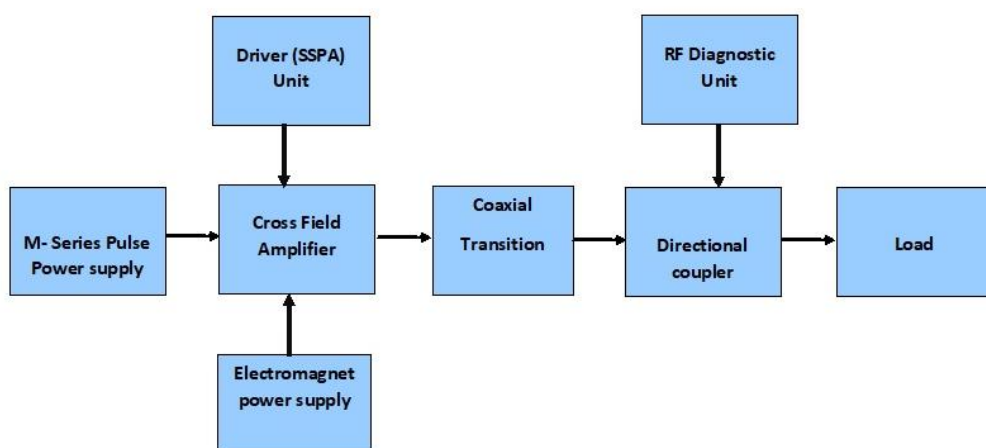
AMPLIFIERS

The advancements in field emitters, magnetic field systems, and slow-wave structures extend beyond CFAs, impacting particle accelerators, medical imaging, industrial heating, and radar systems. Field emitters eliminate heater assemblies, reducing energy consumption and improving electron beam stability, benefiting accelerators, X-ray sources, and industrial microwave heating. Magnetic field systems enhance beam control for microwave tubes, plasma propulsion, and RF heating. Slow-wave structures optimise electron-wave interaction, benefiting TWTs and dielectric laser accelerators for satellite communications and radar. As an amplifier counterpart to the magnetron, the CFA enables high-power RF amplification with better phase and frequency control, which is ideal for radar and broadband RF systems. Its high efficiency and scalability support industrial and scientific microwave heating. These innovations drive sustainability, cost reduction, and reliability in high-power RF applications. The impact extends to new research, industrial commercialisation, and energy-efficient solutions. The project contributes to strengthen European Union's leadership in vacuum electronics and microwave technology.

Proposed updated timeline

We are still working on the development of the crossed-field amplifier. The particle-in-cell simulation study has been completed. The PIC simulation predicts an RF power of 600kW at 713 MHz and the beam-wave interaction is visible. Further optimization is needed. Our strategy is to optimise the beam-wave interaction during the fabrication and testing to achieve the proposed performance metrics. The timeline for CFA development and testing is given in the table below.

Activities	2025							
	Feb	Mar	Apr	May	Jun	Jul	Aug	Sep
Fabrication/Development of CFA								
T1.1 Anode Fabrication								
T1.2 Cathode Fabrication								
T1.3 Magnetic System Development								
T1.4 Coaxial RF window								
T.5 HV insulation development								
Integration and Testing								
T 2.1 VSWR testing								
T.2.2 Magnetic Field Testing								
T 2.3 Integration								
T 2.4 Vacuum Leak Testing								
T 2.5 RF Testing								



Conclusion

The TRL has increased by measuring in the lab the first 3D printed field-emitter prototype. Our advancements in crossed-field amplifier development have successfully attracted and secured additional resources, bolstering our research capabilities. We contributed to the e-Emitter project proposal within the Marie Skłodowska-Curie Actions (MSCA) Doctoral Network, although the project did not receive funding. However, Dr. Anshu Singh, a Marie Skłodowska-Curie Postdoctoral Fellow at Uppsala University was coopted to work on the IFAST project. And additional funding was obtained from Vinnova, Sweden's innovation authority, to work on the commercialization aspects of field emitters for high-power vacuum electron devices (VEDs).

FLA

The high energy consumption for cooling of superconducting cavity contributes significantly to the operation costs of the accelerators. Therefore, there is a strong need for the developing of new materials enabling the cost reduction. Recently we have received a new founding for the developed of high-quality SC coating made by magnetron sputtering and flash lamp annealing. The project is supported by Hi-Acts Use Case Initiatives 2025 and received the funding support of 50 kEuro. The project duration is from 1 of January to 31 of December 2025. Our achievements were noticed by NovAccel Co. Ltd. Japan, who expressed his wish to cooperate on the development of high Tc SC-coating for Cu-based cavities. The LoI from NovAccel Co. Ltd. Japan is attached.

As part of the project, we designed and manufactured the Mobile-Flash tool. Initially, Mobile-FLA was designed for high-temperature processing of superconducting layers deposited on Cu substrates, in particular Cu cavities. We realised that the ability to transfer the system to the customer could greatly expand the application of annealing in the ms range. Our system allows the annealing of three-dimensional objects with a coating layer made both inside and outside the object. The ability to anneal irregularly shaped objects with temperature-sensitive substrates allows us to extend the application of FLA to the thermal treatment of implants, where adhesion between coating and substrate is critical. In addition, the use of controlled atmospheres and ultra-high-temperature processing allows the formation of various alloys, such as nitrides or oxides, which can be used for corrosion protection.

Conclusion

We have started with TRL 3 by performing experiments on planar samples. During the project the TRL was increased to level 4. The real cavity was annealed, and the system can be used for thermal treatment of 6 GHz and 1.3 GHZ cavities.

The Project achieved its two main results:

1. demonstrate the possibility of being able to use FLA to modify the crystal structure of superconducting films of Nb₃Sn and NbTiN
2. construct a UHV implant for the treatment of elliptical cavities.

These results were achieved through the synergy between this IIF project and WP9 of I.FAST. In addition to a fruitful exchange of information with the partners involved, there was also an effective exchange of samples especially with STFC and CEA.

From this basis a new phase of the R&D has already started, which aims to define effective process parameters to implement the FLA process in the Nb₃Sn sample deposition protocol developed in I.FAST WP9.

AMIS

Conclusion

Building upon the successful thermionic emission test at LNL and the successful offline tests at CERN, the LPBF tantalum cathode was integrated into a FEBIAD ion source and employed at the SPES facility to produce the first radioactive ion beam. This achievement demonstrates the technology's operational functionality in a real-world setting, aligning it with TRL 7. In the near future, it will be tested again at the SPES facility, at the ISOLDE facility at CERN, and in other facilities within the collaboration, paving the way to confirm the progress achieved over these years of development. Through extended and repeated use, the system qualification will be further consolidated, potentially leading to its commercialization (TRL 8 - 9).

HVAC

Technology Readiness Level assessment

Plasma Metal Deposition (PMD) as an AM technology

As an Additive Manufacturing technology, the PMD process has been extensively benchmarked and analysed across various aspects, including material combinations, process parameters, printing strategies, material properties and even application-related tests. Collaborations with key partners, such as the European Space Agency, have been integral to this effort. Prior to the HVac project, the technology could be considered to sit at a TRL of 5, with a solid understanding of how to produce radially symmetric or planar objects with slight overhangs (up to 30°). A variety of materials, including steel, aluminum, magnesium, titanium, and Inconel®, had been successfully processed, with their properties well established. The dimensions of printed parts had reached up to 400 mm. Following the HVac project, the PMD process was expanded to accommodate deviations from radial symmetry, the use of deposition pattern transitions, and an increase in the dimension envelope to 500 mm. The vacuum chamber demonstrator represents the largest part produced with this technology to date. While efforts toward series production and automation are still underway, the HVac project has elevated the PMD process to a TRL of 6. Figure 75 presents a visualization of the PMD technology roadmap across various projects, using vessel and chamber examples.

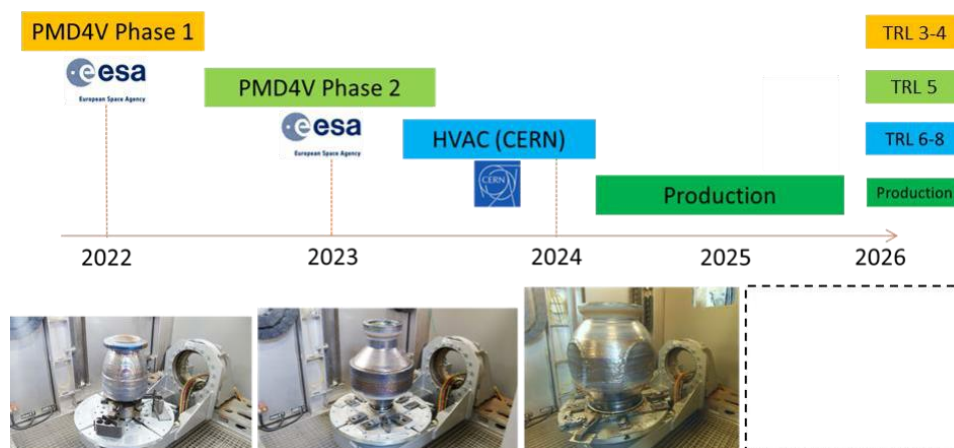


Figure 75. Roadmap of PMD as an AM technique. Given examples are related to pressure vessels and vacuum chambers.

Plasma Metal Deposition (PMD) as a vacuum chamber manufacturing route

It is estimated that for this specific application—namely, the manufacturing of vacuum chambers—the PMD technology was at a TRL of 2 prior to the present project. Although PMD had previously produced pressure vessels within the framework of past projects (as mentioned earlier), vacuum chambers had never been manufactured before, with the demonstrator built during the HVac project being the first of its kind. While the general concept of the technology had been established, its overall feasibility remained uncertain, particularly from a materials and surface preparation perspective. Given challenges such as outgassing and the critical importance of surface preparation, it was unclear whether the as-printed surfaces were suitable for vacuum applications, let alone high vacuum and beyond. Meanwhile, this project successfully demonstrated the feasibility of PMD technology to produce vacuum chambers for high-vacuum applications. Laboratory tests showed that the PMD vacuum chamber can achieve pressures as low as 10^{-8} mbar, potentially making it suitable for applications such as electron microscopy and sputter coating (which still would need further evaluation in an application-relevant environment). Nonetheless, it is reasonable to estimate that the PMD vacuum chambers have now reached a TRL of 4 following the results of the HVac project. Based on the results of this project, PMD vacuum chambers are not yet suitable for particle acceleration, as this application requires significantly lower pressures (10^{-10} to 10^{-12} mbar) that have not been achieved so far. However, it is important to note that no proper baking was performed during this project, which means the current demonstrator could potentially achieve pressures up to one order of magnitude lower than the results observed only by doing so. Consequently, future work would likely focus on surface treatment and how adjustments to printing strategies could improve outgassing properties.

Scalability analysis

At this stage, the consortium began exploring strategies to scale up the PMD process for manufacturing significantly larger vacuum chambers, which represents a natural progression for PMD both as an AM technology and as a method for vacuum chamber production. This effort first involved designing vessel mock-ups and conducting brainstorming sessions together with SBI. Some examples of vacuum chamber mock-ups are presented in Figure 76. These mock-up chambers were largely generic, each incorporating specific structural features that could present manufacturing challenges.

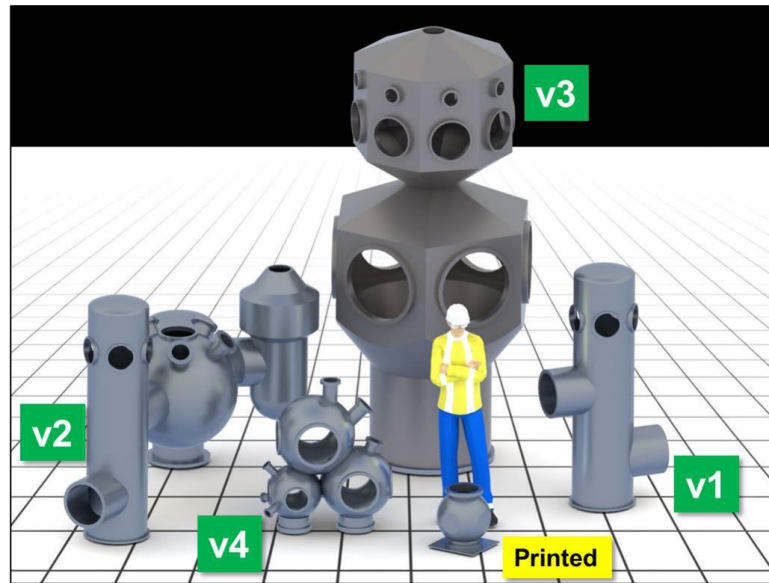


Figure 76. Examples of mock-up 3D-printed vacuum chambers designed for scalability analysis.

V1 included overhanging sections in the form of two lateral connections extending in opposite directions. V2 built upon V1, integrating different concepts for direct assembly of several chambers at once. V3 was a particularly tall chamber (5 m high), posing significant challenges in both size and mass (even for light materials such as aluminum). Lastly, V4 combined three spherical chambers, resembling the demonstrator chamber produced in this study. Currently, none of these chambers could be produced with the available machinery. Next, SBI selected a specific mock-up design (V3 in this case) and proposed two feasible machine design solutions for producing a significantly larger vacuum chamber in a realistic fashion. Each solution has its own advantages and drawbacks, which will be discussed in the following sections.

Design Concept 1

Machine Design Concept 1 featured a tilt-turning table, which is similar to other SBI systems such as the one used in the present project. Conversely, this would not use a gantry system as it currently does, but a robot arm instead, which would be mounted on a rail. The rail would be positioned parallel to the ground, and the machine would offer limited tilting capabilities (i.e., only up to the robot arm's wingspan). This design prioritized first and foremost vertical space, eliminating the need for a tall building with a high ceiling. A mock-up of this concept is shown in Figure 77.

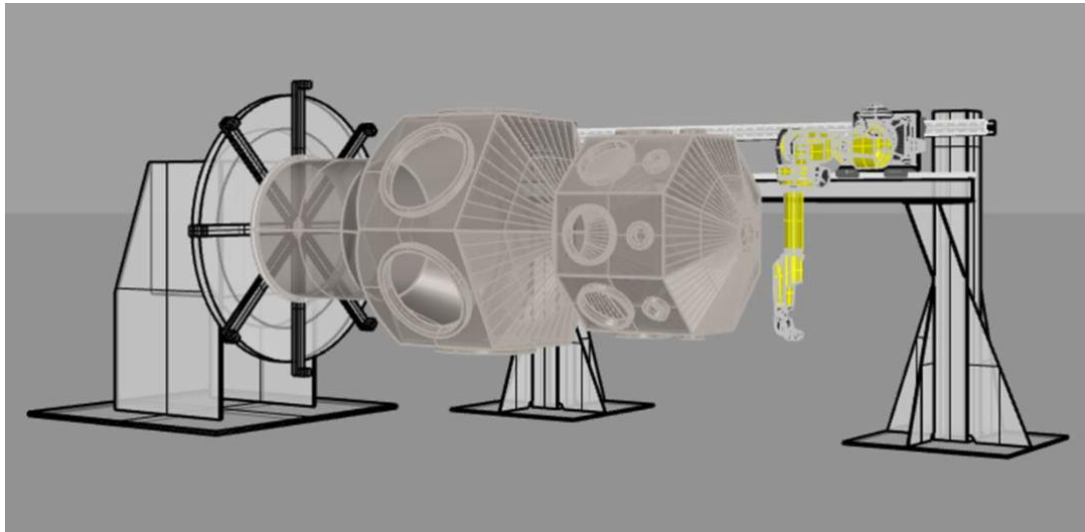


Figure 77. Illustration of the machine Design Concept 1, with mock-up chamber V3 clamped onto the tilt-turning table.

Design Concept 2

Machine Design Concept 2 features a turning table without tilting capabilities, paired with a robotic arm that moves along a vertical rail (instead of horizontal). In this setup, the turning table rotates the workpiece while the robotic arm travels vertically, meaning that it would require less footprint at expense of vertical clearance. A mock-up of this concept is shown in Figure 75.

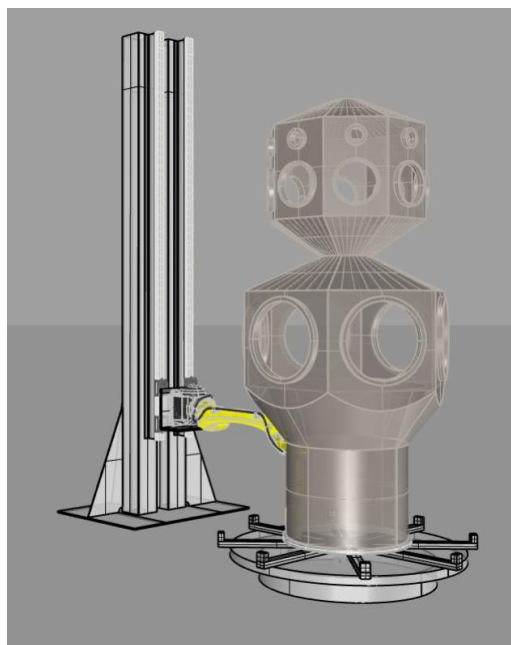


Figure 78. Illustration of the machine Design Concept 2, with mock-up chamber V3 clamped onto the tilt-turning table.

Comparison between Concepts

There are major pros and cons for either of the presented Concepts. These features were split into five main aspects, namely footprint, operation, maintenance, structural concerns and safety risks, as shown in Table 5.

Aspect	Design Concept 1	Design Concept 2
Footprint [excluding chamber]	35 m ² of area, 2 m height	10 m ² of area, 7 m height
Operation	Difficult to mount the substrate, since it must be clamped in a vertical position. Part would need to be tilted back to the upward position once process is finished (with a forklift or overhead cranes).	Easy to mount the substrate (similar to current solutions). Parts do not need to be tilted around during offloading.
Maintenance and repairing	Easier maintenance and repairing in general, since machine parts are closer to the ground	More difficult maintenance, with some machine parts high off the ground. In case of sudden process stoppage, repairing requires special attention.
Structural concerns	Large shear and bending stresses on the tilt-turning table due to the momentum created by a heavy part being printed horizontally. Requires foundation underground to act as counterweight	More manageable stresses. May become a concern for heavy parts from materials such as steel and Inconel
Safety risks	Standard safety precautions required	Elevated heights may require special equipment. Risk of parts breaking off printed objects and falling out

Table 5. Overview of pros and cons of Design Concepts 1 and 2 under different aspects.

Local versus Global shielding gas concepts

For many AM applications, including PMD, shielding gas is essential for ensuring proper processability. It protects the molten material from contamination by atmospheric elements like oxygen and nitrogen, which could affect the material's integrity and properties. The gas helps maintain a stable environment, preventing oxidation and improving the overall quality of the final part. For either design, there was a need to define the shielding gas concept. In the present activity, two were proposed namely local shielding and global shielding. On one hand, “global shielding” involves flushing inert gas, typically argon, into the environment where the printing process occurs. This method is commonly used, including in the machinery for this project, and would require large chamber volumes of 129 m³ for Concept 1 and 100 m³ for Concept 2. To adequately flush the chamber, the amount of argon needed is determined by multiplying the chamber volume by a factor

of 3, resulting in a requirement of 387 m³ for Concept 1 and 300 m³ for Concept 2. On the other hand, “local shielding” entails actively blowing inert gas into a bubble around the print head as it moves. This setup would be attached to the robot arm, eliminating the need for large chambers and resulting in a more compact and less intrusive design. However, it comes at a significant cost in gas consumption, with an expenditure of 100 l/min. For example, the V3 chamber, which takes 1620 hours to manufacture at a 1.1 kg/h deposition rate, would require 9730 m³ of argon, making this method up to 32 times more costly in gas usage compared to the global shielding approach.

Discussion and Final remarks

Considering the ease of operation, part handling, and structural stability, Concept 2 emerges as the better scalability option between both evaluated Design Concepts. While it introduces height-related safety concerns, these can be mitigated with proper safety protocols and maintenance planning. The simpler workflow and reduced mechanical stresses make it a more practical and reliable solution in the long run, especially for scaling up PMD processes. Concerning local vs. global shielding, given the massive difference in gas consumption, global shielding is the superior choice for cost efficiency. While local shielding provides more flexibility and avoids the need for large chambers, its extreme gas usage makes it economically unfeasible for long build times. Therefore, despite the higher initial infrastructure investment, global shielding remains the more practical and cost-effective approach for PMD applications.

Conclusion

In conclusion, this project has made significant strides in advancing the capabilities of the PMD technology, particularly in the context of manufacturing vacuum chambers for high-vacuum applications. The successful demonstration of the PMD vacuum chamber, capable of reaching pressures of 10⁻⁸ mbar with a low leakage rate, has not only proven the feasibility of this manufacturing approach, but also positioned it as a promising solution for industries requiring tailor made chamber geometries; PMD could fill the niche without the need to machine from a block. The project has expanded the understanding of how PMD (or virtually any DED process in general) can be optimized to produce large, complex geometries, with intricate deposition pattern transitions. Furthermore, the creation of two design concepts for the manufacturing system highlighted the challenges and potential of scaling up production. Moving forward, the project has set the stage for further improvements in surface treatment and process optimization, which are expected to enhance the outgassing properties and overall performance of 3D-printed vacuum chambers. At the moment, PMD vacuum chambers have already been proven qualified candidates to be implemented in high-vacuum applications such as electronic microscopy and sputter coating, as previously mentioned. However, there is a good indication that the process has an untapped potential to also become viable for applications such as particle acceleration and high-energy physics—which require substantially higher vacuum levels—once a more thorough evaluation of the relationship between surface quality and outgassing properties is carried out. Furthermore, as the PMD as a technology progresses to a TRL of 6-7, that is, into the realm of commercial production, future efforts will need to focus on automating the manufacturing process to improve repeatability and quality. Automation topics, as

well as geometrical upscaling and performance improvement under vacuum are all relevant areas of interest that can be considered logical expansion fields for the topics addressed during the HVac project. As such, the prospect of triggering follow-up projects is not only intriguing, but desirable. Ultimately, this project has not only demonstrated the technical feasibility of PMD for vacuum chambers but also opened new opportunities for commercialization and innovation in high-vacuum technology. The demonstrator has already become a key asset in marketing and outreach efforts, highlighting the companies' advanced manufacturing capabilities on a global stage.

General conclusion

All the information collected from each report has been carefully transferred to this document.

Fruitful collaboration and synergy have been established with the WP3: Industry Engagement. The first project's business case survey was performed in March 2024 with Dr. D. Safi as the Knowledge Transfer and Business opportunities in accelerator R&D representative. We arranged periodic meetings with the most interested and TRL-advanced projects in P4. We followed their business case analysis progress and tried to identify their needs in collaboration with the Knowledge Technology Transfer from STFC and DESY. These activities will be summarised in a separated report and presented at the 4th Annual Meeting in Krakov.

5 References

TW RF GUN

- [1] Lucas, T.G. et al, Dependency of the capture of field emitted electrons on the phase velocity of a high-frequency accelerating structure, Nuclear Inst. and Methods in Physics Research, A 914C (2019) pp. 46-52.
- [2] Francescone, D. et al, Design study of a compact injector for a synchrotron light source IEEE Transactions on Nuclear Science (2025) (Accepted).
- [3] Lucas, T.G. et al, Application of A Reduced Phase Velocity High Brightness Photogun For MeV Ultrafast Electron Diffraction, Proceedings of International Particle Accelerator Conference (Nashville, USA, 2024).
- [4] T. G. Lucas, et al., Toward a brightness upgrade to the SwissFEL: A high gradient traveling-wave rf photogun. Phys. Rev. Accel. Beams 26, 103401 10.1103/PhysRevAccelBeams.26.103401
- [5] R. Ganter et al. HIGH CURRENT ELECTRON EMISSION FROM MICROSCOPIC TIPS, Proceedings of FEL 2006, BESSY, Berlin, Germany.
- [6] Myhre, et al, 2013: Anthropogenic and Natural Radiative Forcing. In: Climate Change 2013: The Physical Science Basis. Contribution of Working Group I to the Fifth Assessment Report of the Intergovernmental Panel on Climate Change. Cambridge University Press, Cambridge, United Kingdom and New York, NY, USA.
- [7] CERN courier, 15 December 2020: <https://cerncourier.com/a/adapting-clic-tech-for-flash-therapy/>
- [8] L. Zhou, et al. Development of a high-gradient X-band RF gun with replaceable field emission cathodes for RF breakdown studies, Nuclear Instruments and Methods in Physics Research Section A: Accelerators, Spectrometers, Detectors and Associated Equipment Volume 1027, 11 March 2022, 166206.

KAIO

- [1] Albert et al., 2020 roadmap on plasma accelerators, New Journal of Physics 23, 031101 (2021)
- [2] Maier et al, Decoding sources of energy variability in a laser-plasma accelerator, Physical Review X 10, 031039 (2020) (22)
- [3] Bohlen et al, Stability of ionization-injection-based laser-plasma accelerators, Physical Review Accelerators and Beams 25, 031301 (2022)
- [4] Shalloo et al, Automation and control of laser wakefield accelerators using Bayesian optimization, Nature Communications 11, 6355 (2020)

- [5] Jalas et al, Bayesian optimization of a laser-plasma accelerator, Physical Review Letters 126, 104801 (2021)
- [6] Lu et al., Generating multi-GeV electron bunches using single stage laser wakefield acceleration in a 3D nonlinear regime, Physical Review Accelerators and Beams 10, 0613001 (2007)
- [7] Guénot et al., Relativistic electron beams driven by kHz single-cycle light pulses, Nature Photonics 11(5), 293-297 (2017)
- [8] Salehi et al., MeV electron acceleration at 1 kHz with < 10 mJ laser pulses, Opt. Lett. 42(2) 215-218 (2017)
- [9] Nisoli et al., Compression of high-energy laser pulses below 5 fs, Optics Letters 22(8), 522-524 (1997)
- [10] Ouillé et al., Relativistic-intensity near-single-cycle light waveforms at kHz repetition rate, Light: Science & Applications 9, 47 (2020)
- [11] Rovige et al., Demonstration of stable long-term operation of a kilohertz laser-plasma accelerator, Physical Review Accelerator and Beams 23(9), 094301 (2020)
- [12] Nagy et al., High-energy few-cycle pulses: psot-compression techniques, Advances in Physics 6(1), 1845795 (2021)
- [13] Viotti et al., Multi-pass cells for post-compression of ultrashort laser pulses, Optica 9, 197-216 (2022)
- [14] Louis Daniault et al., Single-stage few-cycle nonlinear compression of millijoule energy Ti:Sa femtosecond pulses in a multipass cell, Opt. Lett. 46, 5264-5267 (2021)
- [15] Andreassi et al., Radiobiological Effectiveness of Ultrashort Laser-Driven Electron Bunches: Micronucleus Frequency, Telomere Shortening and Cell Viability, Radiation Research 186, 245-253 (2016)
- [16] <https://www.coherent.com/lasers/amplifiers/astrella>
- [17] <https://amplitude-laser.com/products/femtosecond-lasers/lasers-for-science/magma/>
- [18] Louis Daniault, Jaismeen Kaur, Geoffrey Gallé, Cedric Sire, François Sylla, and Rodrigo Lopez-Martens, Sub-2-cycle post-compression of multi-mJ energy Ti:sapphire laser pulses in a gas-filled multi-pass cell, Optics Letters 49, 6833-6836 (2024)
- [19] Escoto et al., Temporal quality of post-compressed pulses at large compression factors, Journal of the Optical Society of America B 39, 1694-1702 (2022).
- [20] Kaur et al., Simultaneous nonlinear spectral broadening and temporal contrast enhancement of ultrashort pulses in a multi-pass cell”, J. Phys. Photonics 6, 015001 (2024).

HVAC

- [1] Galván, E.A.; Meléndez, I.M.; Mora, C.A.; Soriano, E.M.P.; Neubauer, E.; Kitzmantel, M.;

Galván, E.A.; Meléndez, I.M.; Mora, C.A.; Soriano, E.M.P.; et al. Plasma Metal Deposition for Metallic Materials. In Advanced Additive Manufacturing; IntechOpen, 2021 ISBN 978-1-83962-821-4.

[2] Jayawardane, H.; Davies, I.J.; Gamage, J.R.; John, M.; Biswas, W.K. Sustainability Perspectives – a Review of Additive and Subtractive Manufacturing. *Sustain. Manuf. Serv. Econ.* 2023, 2, 100015, doi:10.1016/j.smse.2023.100015.

[3] Lalegani Dezaki, M.; Serjouei, A.; Zolfagharian, A.; Fotouhi, M.; Moradi, M.; Ariffin, M.K.A.; Bodaghi, M. A Review on Additive/Subtractive Hybrid Manufacturing of Directed Energy Deposition (DED) Process. *Adv. Powder Mater.* 2022, 1, 100054, doi:10.1016/j.apmate.2022.100054.

[4] Bourcey, N.; Campos, P.; Chiggiato, P.; Limon, P.; Mongelluzzo, A.; Musso, G.; Poncet, A.; Parma, V. Leak-Tight Welding Experience from the Industrial Assembly of the LHC Cryostats at CERN. *AIP Conf. Proc.* 2008, 985, doi:10.1063/1.2908564.

[5] Sharma, S.; Gupta, H.; Jain, V.; Ganesh, P.; Gupta, R.; Yadav, D.; Kaul, R. Investigation of Ultra-High Vacuum Compatible Weld Joints of AA5083 and AA6061 Materials for Synchrotron Radiation Source. *J. Mater. Eng. Perform.* 2022, 31, doi:10.1007/s11665-022-06589-8.

[6] Titanium; Engineering Materials, Processes; Springer: Berlin, Heidelberg, 2007; ISBN 978-3-540-71397-5.

[7] Spherical Squares | Kimball Physics | Find Top Spherical Squares at Kimball Physics ! Available online: <https://www.kimballphysics.com/product-category/multi-cf-hardware/vacuum-chambers/spherical-squares/> (accessed on 11 February 2025).

[8] Kurisu, H.; Ishizawa, K.; Yamamoto, S.; Hesaka, M.; Saito, Y. Application of Titanium Materials to Vacuum Chambers and Components. *J. Phys. Conf. Ser.* 2008, 100, 092002, doi:10.1088/1742-6596/100/9/092002.

[9] Kamiya, J.; Takano, K.; Yuza, H.; Wada, K. Evaluation of Titanium Vacuum Chamber as Getter Pump. *E-J. Surf. Sci. Nanotechnol.* 2022, 20, doi:10.1380/ejssnt.2022-017.

[10] RHP-Technology GmbH | Technology Transfer Track Posters. BSBF 2024 - Big Sci. Bus.

Forum 2024 Trieste Italy.

[11] Cooper, N.; Coles, L.A.; Everton, S.; Maskery, I.; Champion, R.P.; Madkhaly, S.; Morley, C.; O'Shea, J.; Evans, W.; Saint, R.; et al. Additively Manufactured Ultra-High Vacuum Chamber for Portable Quantum Technologies. *Addit. Manuf.* 2021, 40, 101898, doi:10.1016/j.addma.2021.101898.

[12] Vovrosh, J.; Voulazeris, G.; Petrov, P.G.; Zou, J.; Gaber, Y.; Benn, L.; Woolger, D.; Attallah, M.M.; Boyer, V.; Bongs, K.; et al. Additive Manufacturing of Magnetic Shielding and Ultra-High Vacuum Flange for Cold Atom Sensors. *Sci. Rep.* 2018, 8, 20352, doi:10.1038/s41598-018-20352-x.